Journal of Theoretical and Applied Information Technology

31st March 2024. Vol.102. No 6
© Little Lion Scientific

ISSN: 1992-8645 www.jatit.org E-ISSN: 1817-3195

ENERGY OPTIMIZATION APPROACH BASED MACHINE LEARNING ON LINEAR REFLECTOR SYSTEMS

MOHD ARIF[1], MALABIKA ADAK[2], ANJUM ARA AHMAD[3], CHHAYA NAYAK[4], IBRAHIM AQEEL[5], SHADAB ALAM[6*], DYUTI BANERJEE[7], AYASHA SIDDIQUA[8]

[1]Department of Educational Services and Equipment, Jazan University, Jazan, Saudi Arabia
[2]Department of Applied Mathematics and Humanities, Yeshwantrao Chavan College of Engineering, Nagpur, Maharashtra, India
[3]Department of Statistics, Rizvi College of Arts, Science & Commerce, Bandra West, Mumbai 400050, Maharashtra, India
[4]Pimpri Chinchwad College of Engineering, Pune, India
[5]College of Computer Science & IT, Jazan University, Jazan, Saudi Arabia
[6]College of Computer Science & IT, Jazan University, Jazan, Saudi Arabia
[7]Artificial intelligence & Data Science (AI&DS), Koneru Lakshmaiah Education
[8]Department of Information Technology and Security, Jazan University, Jazan, Saudi Arabia

makhtar@jazanu.edu.sa[1] malabikaadak@yahoo.co.in[2] anjumahmad2018@gmail.com [3] chhaya2007@gmail.com [4] iahmed@jazanu.edu.sa [5] s4shadab@gmail.com [6] dyuti738900@gmail.com [7] asiddiqua@jazanu.edu.sa[8]

ABSTRACT

Solar energy is a renewable and cost-effective energy source that holds great promise for meeting global energy demand. This capability is exemplified in solar-powered cooling systems, which have gained popularity in recent years. Addressing the environmental issues associated with fossil fuel consumption, this study investigates the application of linear Fresnel reflectors (LFRs) in solar-based refrigeration systems A novel approach uses equipment -Uses learning models to optimize LFR output, so that grid-based energy -Increased supply chain efficiency. The study uses Simulink simulations to evaluate the performance of the model, with a particular focus on its energy efficiency compared to other methods. This study addresses the complex challenges posed by sustainable energy and highlights the need for sustainable solutions. Studies focusing on LFRs contribute to the growing knowledge of solar energy efficiency. The inclusion of machine learning techniques demonstrates innovation in improving the performance of solar collectors and offers potential improvements in solving energy consumption problems Simulations in Simulink for testing robust areas, indicate that the proposed machine learning LFR outperforms other methods in terms of energy efficiency. The study highlights the importance of switching to renewable energy sources, especially in cooling systems. The use of linear Fresnel reflectors, together with advances in machine learning, represent a promising approach to energy efficiency. These issues contribute to the ongoing discourse on sustainable energy practices, offering compelling solutions for reducing environmental footprints.

Keywords: *Energy Consumption; Cooling Systems; Machine learning; Linear Fresnel reflectors; Energy Efficiency*

1. INTRODUCTION

Concentrating solar power is the method of transforming solar power, also known as CSP, into electricity through an intermediary process. The vast majority of CSP systems utilise large-area mirrors to concentrate the sun rays onto a relatively narrow receiver aperture. The following types of CSP technology are on the list: the Fresnel, parabolic trough, dish/engine and central receiver. This allows solar power plant dispatchability to be improved by using large-scale thermal storage in conjunction with the first three technologies [1][2][3]. There a maintenance problems, space, changes in water up and down, and connection problems, these will probably be fixed and used more in the future.

Line-focused Concentrated Solar Power (CSP) equipment may include parallel Fresnel collectors and parabolic troughs [4]. A linear Fresnel collector consists of primary reflectors and a receiver assembly have the potential to contain one or more linear receiver tubes as well as a secondary reflector. During the day, the primary reflectors move in a direction that is perpendicular to the path of the sun while the receiver assembly stays put. In contrast to parabolic troughs and large-sized heliostat mirrors for central-receiver systems, the low-profile reflector architecture enables an improvement in the concentration ratio without an increase in wind loads. This is possible because of the reflector's relatively low profile. Because wind torque loads are usually proportional to the square of the mirror height, this is the case here. The height of the mirror is why this is the case [5].

Because of the low-profile architecture, there is a great deal of leeway in determining the concentration ratios, which makes it possible to construct linear Fresnel collectors for a wide range of temperatures at which the light must be collected [6][7]. Since they are so effective at generating heat at low and medium temperatures, linear Fresnel collectors have been the most popular choice on the market for a significant amount of time. When operating at low or medium temperatures, the linear Fresnel is useful for a broad variety of purposes, including the heating and cooling of buildings, the supply of heat for industrial processes, and the treatment of water, among other things [8]. High-temperature heat is most typically produced by SOTA linear Fresnel collectors, which are more commonly constructed [9]. When generating electricity from large amounts of sunlight, it should be stored in batteries if there is no immediate demand for it. Otherwise, you will have to trip it. (Disconnect trip-function). Larger batteries have not been found to date. Buying a battery in the thousands would not be economically viable. To solve this problem, there is something called a pumped storage (hydroelectric power station) funnel power plant. When there is no electricity demand, the solar electricity generated can be pumped to the pump and the river water can be pumped from the bottom to the top of the dam. When the solar is not working when electricity is needed (at night or in the clouds the solar does not work), that electricity can be started by running the funnel power station, as the reservoir is full of water. The same pump can be driven as a turbine. Or you can use a turbine alone, with a normal pump.

One aspect of a solar-powered energy supply is demonstrated by several types of cooling systems. The need for cooling is estimated to account for 10% of all power produced globally [10]. The use of refrigeration cycles also has unfavourable effects on the surrounding ecosystem. When there is an abundance of solar energy, the demand for cooling increases. The fact that solar-powered cooling systems do not require the use of energy and do not contribute to environmental pollution makes them interesting. Recently, improvements have been made to the cooling systems utilised by solar collectors [11]. In particular, sorption refrigeration technologies are becoming increasingly prevalent. This is the case since collectors in cooling systems are able to deliver the required operating temperature [12]. Solar sorption systems, such as adsorption and absorption, have a massive amount of potential for cooling the environment [13]. The number of articles that have been published about utilising solar energy for cooling purposes is increasing. It is great to see that in the most recent year or two, there has been an increase in the number of publications that reference solar-powered air conditioners [14][15].

In this work, linear Fresnel reflectors are investigated in terms of the potential use they have in cooling systems. The study uses a machine learning model to process the generator to provide efficient output from the LFR to the grids. A motor that requires more power A.C. is available in sizes other than refrigerator and water heater. Even better is to set up LED lights in the house. Similarly, solar water heaters can be set up. This will reduce the monthly electricity bill.

2. RELATED WORKS

This section contains a retrospective look at linear Fresnel collectors and their applications throughout the years, as well as some forecasts regarding the foreseeable future of the technology.

Solar collectors, which can be of either a thermal or an electrical type, are what are used to harvest the sun's rays in order to extract usable energy (photovoltaic panels). Explaining the electrical performance of a PV panel can be done with the use of an equivalent circuit consisting of resistors and diodes [16][17][18]. Every solar power system must have at least one collector as one of its components. Using thermal collectors, it is feasible to harness the heat-producing potential of solar radiation and make it usable heat [19][20][21]. The two most common varieties of thermal collectors are known respectively as non-concentrating collectors and concentrating collectors. Non-concentrating types of collectors include flat-plate collectors, also known as FPCs, and evacuated tube collectors [22]. Solar energy gives off its thermal energy for free. We just have to electrify it. Similarly, waterfalls give their kinetic energy for free, and we just convert it into electricity. In the same way, the earth gives its petrol for free, we just have to turn it into electricity. The wind gives away its kinetic energy for free, and we just have to electrify it.

When the sun's rays strike the absorber of the collector, it converts the sun's energy into heat, which is then distributed throughout a system of fluid tubes. In the same way that absorber surfaces are handled in flat plate collectors, absorber tubes that are surrounded by an evacuated tube are used in the construction of evacuated tube collectors. Within a parabolic collector, a reflector surface acts as a conduit for the radiation to be reflected onto an absorber tube. Because of their ability to follow the sun along an axis, simple parabolic collectors are more effective than their complex counterparts [23]. The localized production is better in some sectors such as green electricity, agriculture, and construction respectively [24]. DC was electricity at the time electricity was invented. The AC power supply was invented because of the high power loss to transport it to a remote location [25]. The electricity available in the solar panel is low-volt DC electricity. Not suitable for carrying with the parcel.

These collectors suffer from a variety of structural and hydraulic problems, the most notable of which is the higher fabricating reflector cost along with the wind loads. Fresnel collectors do not contain difficulties that were previously noted as being connected with parabolic collectors. This is because Fresnel collectors do not have moving receivers and instead employ flat reflectors. Dish collectors are one method that can be utilised to produce heat. This collector can follow the sun in two dimensions thanks to the point reflector it possesses. Heliostat field collectors, which comprise a large number of reflective panels and direct the sun's rays toward a central receiver, are one method that can be used to gather solar radiation for energy collection [26]. Heat transfer can be improved in concentrating solar collectors by using fins that are hollow and cylindrical in shape [27][28].

There are many different fluids that can be used to transmit heat, such as water, air, nanofluids, thermal oils, and so on. Heat can be collected by collectors and then transferred to other systems. Working fluids are typically made using nanofluids because of the excellent heat transfer efficiency that these fluids possess [29][30]. If you use the direct technique, the fluid will be heated directly, and then it will be circulated via the collector. If you use the indirect method, the fluid will be heated directly, and then it will be circulated through the heat exchanger [31][32][33]. Ethylene glycol is a frequently selected option when it comes to the indirect water system. In addition to this, the utilisation of additional fluids, such as silicone oils and refrigerants, is essential. When it comes to absorption refrigeration systems, water-ammonia and water-lithium bromide are two of the fluids that are utilised for solar cooling more frequently than others. Ammonia is utilised as the coolant, and lithium is put to use in the absorption process [34].

Absorption chillers are a type of cooling system that was explored in [35] in their study of a cooling system for a house with one level. In the calculations, a transient model of a hybrid solar cooling system driven by PDC, and flat plate collector was utilised, but in the experiments, the PDC was the component that was utilised. The sun emits 62,900 kW of energy per square meter. This represents a capacity of approximately 1 million electric lights. Such an image is impressive - the sun is 8,000 billion KW every second on Earth, I.E., many times more than all the power stations in the world. Pre-mission of modern science - to learn solar energy more fully and efficiently as it is safer. Scientists believe reliable use of solar energy - this is the future of man. In order to determine the extent to which time and environmental factors, energy tariffs and flat collecting areas all had an impact on the functioning of the system, these factors were investigated. All of these figures were based on the reduction in energy consumption. Their findings suggest that the suggested system would not be very cost-effective due to the low gas and electricity rates that are prevalent in the research area. As a consequence, the payback period would be quite lengthy. It possible that a workable method would be to replace LFR collectors with more pricey alternatives in order to shorten the payback period [36]. An experiment is found in [37] to investigate absorption cooling cycles utilising PDC in conjunction with three fluids (ammonia, water, and hydrogen), respectively. During the course of the experiment, which lasted for a total of two days, temperature readings were taken from both the generator and the evaporator. When the evaporator was maintained at 23 degrees Celsius and the generator was maintained at 92 degrees Celsius, the coefficient of performance (COP) was measured at 1.6.

An absorption refrigeration cycle is found in [38]that is capable of supplying power in addition to desalinating water. A multi-effect technology that is based on the absorption of ammonia and water is utilised in the desalination portion of the refrigeration system. The amount of cooling power produced by the specified refrigeration cycle was 820.85 kW. We used Aspen Hysys to run simulations and then analysed the results to see how the second law of thermodynamics affected each individual component. Heat exchangers and distillation columns were found to be responsible for 86 percent of the total energy rate loss. The system overall energy efficiency and thermal efficiency were both 66 percent and 80 percent, respectively. They calculated that the aforementioned system would have a payback period of 5.783 years and would provide an annual net profit of 6.828 million US dollars.

Cascaded vapour compression-absorption system is developed in [39]. The organic Rankine cycle, also known as the ORC, is utilised in this system, which is driven by solar-biomass energy, in order to create low-temperature cooling. The study performed a thermo-economic analysis to calculate the solar fraction and the point at which PDC and LFR reach a position where they are no longer losing money. Because LFR has a lower yearly efficiency. and a higher cost, the solar fraction and the point at which it is profitable to switch to LFR are both lower. They also made adjustments to the ORC working fluid and determined break-even values as part of their investigation into the effects of the working fluid. When compared to a solar-biomass-powered system, the capital expenses and break-even point for the biomass system were 39 and 30 percent lower, respectively. Furthermore, the biomass system had a 30% lower break-even point.

3. PROPOSED METHOD

The LFR and PTC telescopes also use an approach that is quite similar to this one, in which the mirrors are steered in predetermined patterns in order to minimise the radiation angle of incidence and, as a result, maximise the amount of radiation that can be collected from incident rays. This is done in order to make the most efficient use of the irradiance that is received by the concentrator while it is arranged in an East-West tracking configuration and is being used to generate energy. In order for a Solar power plant to successfully generate electricity, the layout of its solar fields should be given the utmost importance. Because a poor design can result in low operating times, an increase in the thermal energy storage capacity, poor thermal performance, and even the operation of the power block because the concentrated solar energy density is insufficient. The reasons that are explained in this study led to the development of an opto-geometric optimization technique, and a schematic representation of this methodology. Figure 1 shows the Optimization of the LFR using ML. They use LFR rather than PDC to power their solar-powered system since LFR is more cost-effective. On the other hand, the use of PDC for a single cooling output does not have an economic justification.

A. Problem statement

Prior research examines various aspects of solar energy harvesting, including heat and electronics, with a particular focus on photovoltaic panels The discussion clarifies the energy performance of PV panels through a uniform circuit model so and emphasizes the important role of thermal collectors in harnessing solar radiation for usable heat. Various collectors such as parabolic, Fresnel, dish, and heliostat field collectors are examined for their specific capabilities in capturing solar radiation The research extends to heat transfer using various fluids and explores techniques direct and indirect. Experiments and analyzes of hybrid solar coolers, absorption chillers, and cascaded vapor compression-drying systems provide insights into payback time, energy efficiency, and economic consideration s for the scope of this research this It lies in addressing the identified gaps and provides valuable insight into the economic viability of using parabolic container collectors for cooling applications.

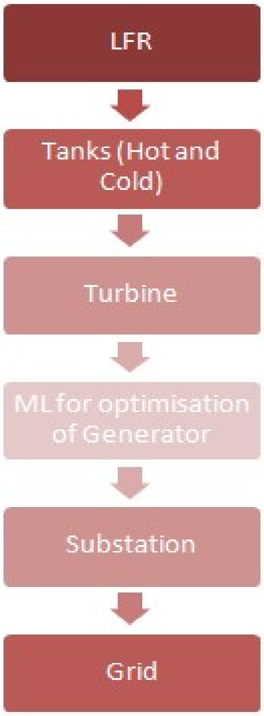

Figure 1: Optimization of the LFR using ML

The first thing that has to be done in order to begin the process of optimization is to determine the precise location of the power plant. Because of these data, a more accurate estimation of irradiation direction and incidence was possible by employing computations that took into account the angle of the sun. After determining the optimal receiver height and criterion, the intercept factor (IFC) and the incidence angle modifier (IAM) are computed once the criterion has been satisfied.

After that, the geometry of the CPC will be specified. A ray-tracing comparison of the flux distribution, and the optimised field is carried out, which is the fourth step. After that, a thermal technique is used to make a comparison between the enhanced field and the FRESDEMO field. The oldest method of passive use is solar power - it is painted on a dark-colored water tank. The darker the color, the more concentrated the sunny energy, the hotter it becomes - the warmer the water. However, there are progressive methods of passive use. The Solar power Construction Techniques When designing building designs, accounting for climatic conditions is used as much as possible in the selection of building materials. With this design, the construction of the building has accumulated a collector.

In order to configure the structure and construction of the LFR in such a way that the reflected solar radiation is directed to the receiver in the most efficient manner possible, the sun angles need to be determined first. In the case of a solar field that runs in a north-south orientation. LFR performance can also be affected by other factors like the positioning of the receiver height. In accordance with Fermat Principle, a target zone is the receiver, will be used to calculate the inclination of each mirror. However, as the distance between the mirrors increases, so does the amount of time it takes for light to travel; as a result, not all light tends to reach the receiver region. The intercept factor is a useful metric for quantifying this circumstance. Solar power solar collectors are used at the heart of active application systems. The collector heats the cooling by absorbing sunny energy cooling, heating the water, and converting the electrical energy. Solar collectors can be used in all activities for industrial, agricultural, and domestic needs.

There will be losses in this captured radiation that should be zero because the intercept factor (A)should have a unit value. This is because the LFR is not an ideal concentrator, where the losses are found in the captured radiation. Despite the vast number of methods that can be used, it is possible to determine the intercept factor by using more straightforward methods. These methods can be used in place of the numerous other methods that can be used. Among these are the direct application of the conservation and the utilisation of an improved ray-tracing technique as in equation (1).

$$FF=A'/A_{il}=a'L_m/(a'_l+a'+a_r)L_m \quad (1)$$

A_{il} - Total lighting area
A' - Receiver area
a_r - Right receiver spillage
a_l - Left receiver spillage
a' - Receiver width
where $0° \le \alpha_T \le 180°$, if $\alpha_T=90°$ when $\sin\gamma_s=0$.

Based on the immediate examination of the intercept factor, it is possible to draw the conclusion that incidence angles do have a role in determining the value of the intercept factor. Because the amount of irradiance that is received by the receiver will be at its highest point around solar noon, this is the best time of day to perform the intercept factor optimization so that it can be maximised. In the scenario in which the field is assumed to be situated at the equator, the location known as the reference position is the one in which the mirrors are arranged in such a way as to maximise the intercept factor. In order to construct the geometric description of the Fresnel reflector, it is necessary to have the inclination angleψ_i, which varies depending on where the sun is located and shown in equation (2).

$$\tan\alpha_T = \tan\alpha_s \sqrt{1+\frac{1}{\tan^2\gamma_a}} \quad (2)$$

ψ_i- inclination angle of mirror
β_i– inclination angle
α_T- transverse angle of solar altitude

The real focal distance with the primary mirrors h_{fr} is estimated as below as in equation (3):

$$\psi_i=\alpha_T - \beta_i^2$$

$$\beta_i=\arctan(h_{fr}d_i) \quad (3)$$

The inclination does not depend in any way on the position of the mirror; rather, it is entirely dependent on the temporal shift that occurs in the angle α_T. Each row of mirrors has a unique angle location, but they all rotate at the same pace. Despite this, the overall effect is seamless. In theory, a single motor might power all of the mirrors by means of a straightforward mechanical link composed of four bars (a rocker mechanism). On the other hand, contemporary LFRs have come to the conclusion that moving each mirror independently is the most effective technique to achieve precise tracking and gradual defocusing. The receiver in FRESDEMO Fresnel field arrangement is placed at a distance of 8 metres from the primary mirrors, with a spacing of 0.6 metres (a') between them (h_{fr}). The FRESDEMO field has a maximum intercept factor of 0.5753 for the point that serves as the reference. Therefore, it is possible to establish the position of the primary mirrors based on the position of the most recent mirror. The position and tilt of the mirrors are determined according to the equation for the reference point (which is solar noon). This is the simplest type of solar collector. Its design is very simple and reminiscent of the effect of a typical greenhouse, which is on any summer cottage. Spend a little experiment. On a winter sunny day, put any item in the sun and let the sun's rays fall on it and after a while put the palm on it. You feel like this item is hot. And can be outside the window.

B. Machine Learning

A Logistic Regression classifier is the most fundamental form of neural network, as there is only one neuron present at each node in this architecture. An output is produced by a computational neuron using a non-linear activation function that takes the sum of weighted inputs as its input and generates the output using that input. Logistic regression is a technique for supervised learning that can be used to tackle classification problems that involve outputs that are discrete (i.e., labels) [40]. Logistic regression and other types of regression modelling that use sigmoid activation functions are able to translate features from an input feature set to a continuous vector. This vector can then be used to indicate the likelihood that the input belongs to one or more of these classes. The following formula can be utilised when modelling data using logistic regression with two classes: There is a relationship between sigmoid function as in equation (4):

$$f(x) = sigmoid(W^T x + b) = \frac{1}{1+\exp(W^T x+b)} \quad (4)$$

Where
W- weight vector
x - feature vector and
b- bias.

The values of W and $b$are produced at random via gradient descent or stochastic gradient descent (SGD) methods, and they are then optimised by minimising a cost function in order to achieve the best possible solution (e.g., negative log-likelihood). Using a model with the optimal parameters, it is possible to make predictions about future inputs even when the labels are unknown. It is a linear classifier, which means that it makes predictions based on a linear combination of the input features. Figure 2 shows the advantages of machine learning.

This combination splits the spaces containing the input characteristics into halves. Because of their low computing complexity and excellent resistance to over-fitting, linear classifiers have the advantage of requiring features that are linearly separable in the feature space. This is typically extremely difficult to achieve in many applications, including medical imaging. Linear classifiers have the advantage of requiring features that are linearly separable in the feature space. Alternately, a Multiple Layer Perceptron (MLP) can be used to generate a non-linear classifier by combining a number of basic neurons.

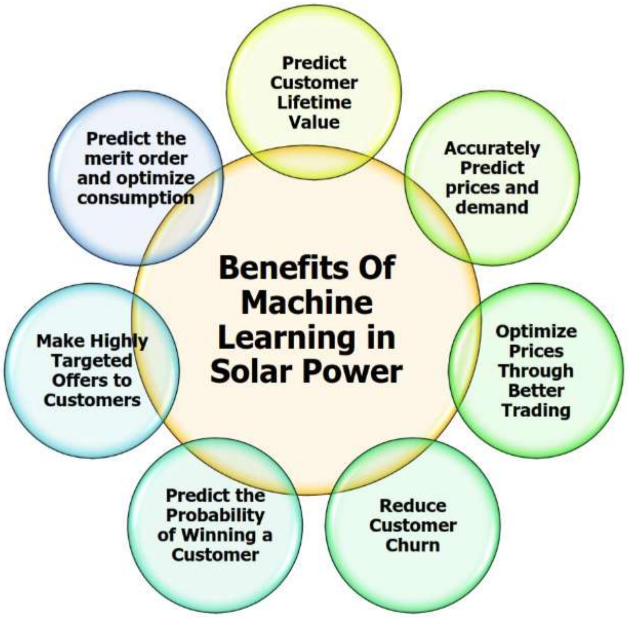

Figure 2: Benefits of machine learning.

The main feature of the collector is a thermocouple insulated plate. The plate is painted in a dark color. Sunlight passes through the exposed surface, heating the plate, and then heating the air flow into the atmosphere. Air passes through due to natural convection or by using a fan, which increases heat transfer. However, the absence of work on this system requires additional costs for fan work. These collectors work through light day, so they do not change the main source of heat. However, if you make a collector the main source of heating or ventilation, its efficiency will increase.

As a result of the limits imposed by hardware and computerised methods, MLPs consist of three layers. To get started, let look at the input layer, which is a representation of the feature vectors that are taken in by the network. The second layer is known as the hidden layer because its values are not visible in the training set. This is why the second layer is called the hidden layer. It is possible for the input and hidden layers to be fully coupled thanks to the presence of an output neuron that has a sigmoid activation function and is connected to neurons in both layers. This non-linear mapping is carried out in the expectation that optimised hidden features will be able to be linearly separated, which is the motivation behind the introduction of a hidden layer. The following is the formula for an MLP with two layers as in equation (5):

$$f(x) = G(b^{(2)} + W^{(2)T}(s(b^{(1)} + W^{(1)T}x))) \quad (5)$$

where

$b(1)$ - biasof layer 1,

$W(1)$ – weight matrix of layer 1,

$b(2)$ – bias of layer 2, and

$W(2)$ –weight matrix of layer 2.

G- Activation function used for the output layer that contains a sigmoid function and

s - Activation function used in the hidden layer.

The sigmoid kind of rectified linear unit is very popular and can be found rather frequently (ReLU). For instance, one way to reduce the size of a log-likelihood function is to use the back-propagation algorithm in conjunction with SGD, which is a type of chain-rule derivation. The collector consists of solar energy, coatings (glass with a reduced metal content), a tube and a heated insulation layer. The transparent coating protects the houses from adverse weather conditions. In this case, the solar power supply panel (absorber) is connected to the air conditioner, which circulates through the pipes. The pipe can be both in the form of a ladies and a barbeque. Cooling moves from the entrance to the entrance, gradually heating up. The suction board is made of metal well conductive heat (aluminium, copper).

4. RESULTS AND DISCUSSIONS

It is possible to calculate the intercept factor for systems that have a variable height. Altering the angle at which the mirrors are tilted is required in order to ensure that the absorber tube continues to receive light even after the intercept factor has been optimised for height. The variation in the intercept factor that occurs due to an increase in receiver height is depicted in Figure 3 - Figure 8. It is interesting to notice that the intercept factor does not much increase after 22m, but dealing with receivers at that height would make the installation more difficult.

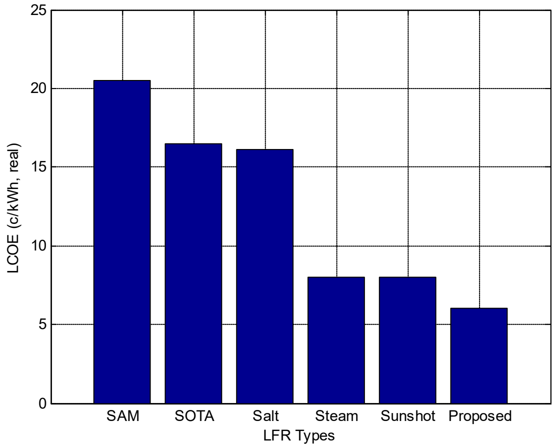

Figure 3: LCOE (c/kWh, real)

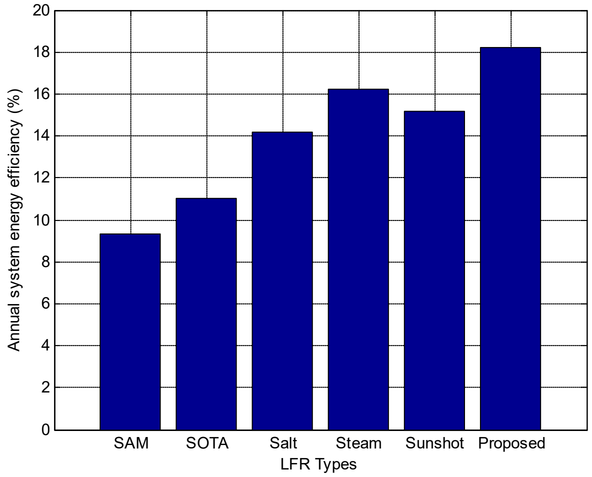

Figure 4: Annual Energy Efficiency (%)

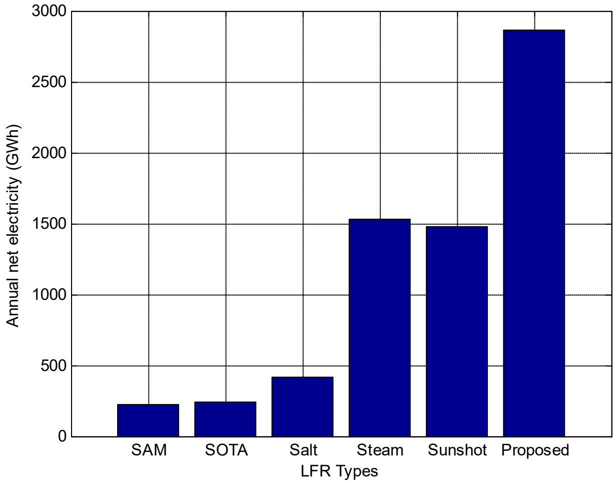

Figure 5: Annual net electricity (GWh)

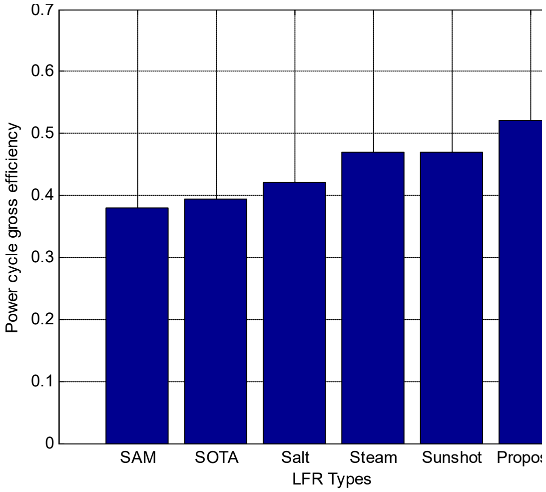

Figure 6: Power cycle gross efficiency

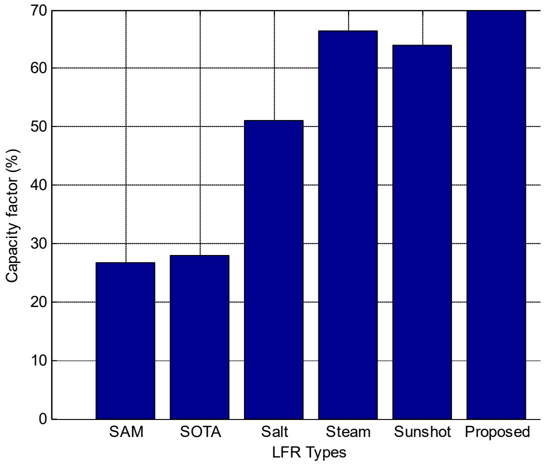

Figure 7: Capacity factor (%)

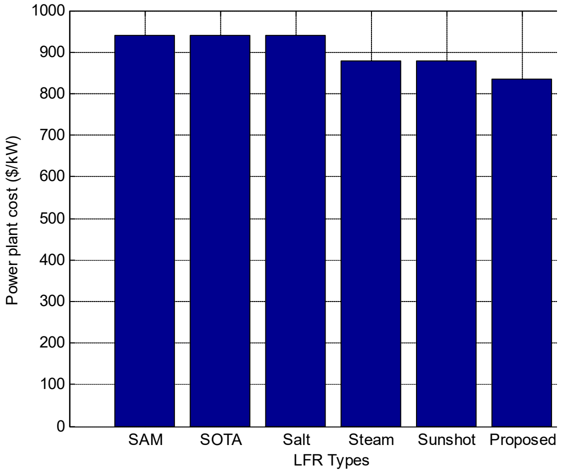

Figure 8: Power plant cost ($/kW)

A single criterion was all that was needed to establish the height. On the curve, an extreme point was found, which refers to the point at which the rate of change no longer increases considerably after reaching that point. The figure comes out to a little more than 15 metres when considering these circumstances. According to the above graph, the intercept factor equals 0.73 when the height of 16 metres is used as an optimization point. Because there is no change in the field width, there is no change in the placement of the mirrors. Following the completion of the calculation for the intercept factor, the next step involves locating an incident angle modifier (IAM). Calculating the IAM requires taking into consideration both the longitudinal and transverse angles, and the formula for this calculation is $IAM=IAM(\theta_l,\theta_t)$. Combining the longitudinal K_l and transverse modifiers K_t to generate the incidence angle multiplier is a standard definition. This multiplier can then be used to acquire both parameters individually.

As was previously mentioned, the architecture of the systems allows for the possibility of a different number of cavity systems and absorber tubes for the receiver. In the most basic configuration, just one tube is used. This tube will most likely be located inside a hollow that has a glass cover on the bottom if you are using a compound parabolic concentrator (CPC). A modified CPC in the receiver in order to increase the geometric concentration coefficient and deflect any radiation that does not contact the absorber directly. As a result, the receiver will only require a single tube to function properly. As a consequence of this, optimising the height of the CPC is not possible due to the fact that the geometric concentration is low. Visit to gain a better understanding of the meaning of the term truncation criterion and the implications it has. Only those photons that are not immediately collected by the absorber will be redirected by the CPC; this contributes to the conservation of energy and the reduction of optical losses. The restriction placed on the half acceptance angle θ_{max} by the principal mirror reflection is as follows: If the angles that enter CPC are going to be absorbed, the geometry of the field requires that they be exactly equal to or less than 33.45 rad. It is not recommended to cut the CPC because, as was explained earlier, θ_{max} = 66 degrees + 1.2 radians.

The provided bar graph illustrates a comparative analysis of power plant costs (in $/kW) for various Low Frequency Resonance (LFR) types, including SAM, SOTA, Salt, Steam, Sunshot, and Proposed. The costs across LFR types exhibit minimal variation, falling within the range of 800 to 900

$/kW. The research problem centers on identifying the most cost-effective LFR type for power generation, with the chosen evaluation criteria being the cost of power plants in $/kW. The significance of these choices lies in their direct impact on economic feasibility and scalability. In terms of analysis criteria, there is a similarity in the comparable costs among LFR types, yet differences may arise in other crucial factors such as efficiency and environmental impact. The outcome suggests no clear winner based solely on cost, emphasizing the importance of considering holistic factors including efficiency, reliability, and sustainability in LFR selection. It is crucial to acknowledge known facts about performance efficiency to inform decisions effectively. In conclusion, while cost is a vital consideration, a thorough evaluation encompassing multiple dimensions is necessary for optimal LFR selection.

5. CONCLUSIONS

In conclusion, the implementation of an energy efficiency method based on machine learning for linear reflector systems, especially focusing on the effect of increased receiver height, improved the overall system efficiency significantly improved The modification allowed for a larger window through which sunlight could penetrate and be transmitted to the CPC, thereby increasing the light-trapping capacity of the system A key finding of this study is the observed increase in blocking factor from 0.58 to 0.73 due to receiver height, resulting in shorter loops in the field This decrease in total loop length is significant, as it indicates solarization energy is used more efficiently, with less light absorption and heat gain per m2 as a result The total length of the Fresnel zone was effectively reduced from 990 meters to 795 meters, representing a significant reduction in loop length of 22%; This improvement in energy efficiency was achieved while keeping the primary crystal width, filler, and absorber tube diameter constant The results of this study confirm that a machine learning model be used to optimize linear imaging systems, improve solar energy harvesting and utilization These findings of increased potential underline the need for advanced solar a implementation, paving the way for more sustainable and efficient energy solutions.

REFERENCES:

[1] P. Esfanjani, S. Jahangiri, A. Heidarian, M. S. Valipour, and S. Rashidi, “A review on solar-powered cooling systems coupled with parabolic dish collector and linear Fresnel reflector,” *Environ. Sci. Pollut. Res.*, vol. 29, no. 28, pp. 42616–42646, 2022.

[2] Z. Said, M. Ghodbane, L. S. Sundar, A. K. Tiwari, M. Sheikholeslami, and B. Boumeddane, “Heat transfer, entropy generation, economic and environmental analyses of linear Fresnel reflector using novel rGO-Co3O4 hybrid nanofluids,” *Renew. Energy*, vol. 165, pp. 420–437, 2021.

[3] O. M. Ikumapayi *et al.*, “A Brief Study into Renewable Energy Technologies,” in *E3S Web of Conferences*, 2023, vol. 391, p. 1083.

[4] A. Barbón, J. A. Fernández-Rubiera, L. Martínez-Valledor, A. Pérez-Fernández, and L. Bayón, “Design and construction of a solar tracking system for small-scale linear Fresnel reflector with three movements,” *Appl. Energy*, vol. 285, p. 116477, 2021.

[5] X. Zhao, S. Yan, N. Zhang, N. Zhao, and H. Gao, “Solar flux measuring and optical efficiency forecasting of the linear Fresnel reflector concentrator after dust accumulation,” *J. Therm. Sci.*, vol. 31, no. 3, pp. 663–677, 2022.

[6] A. E. Rungasamy, K. J. Craig, and J. P. Meyer, “A review of linear Fresnel primary optical design methodologies,” *Sol. Energy*, vol. 224, pp. 833–854, 2021.

[7] H. Singh, A. Singh, R. S. Mishra, and A. Pal, “A current review on linear Fresnel reflector technology and its applications in power plants,” in *International Conference on Recent Advancements in Mechanical Engineering*, 2020, pp. 431–440.

[8] Q. Sun, D. Lin, M. Khayatnezhad, and M. Taghavi, “Investigation of phosphoric acid fuel cell, linear Fresnel solar reflector and Organic Rankine Cycle polygeneration energy system in different climatic conditions,” *Process Saf. Environ. Prot.*, vol. 147, pp. 993–1008, 2021.

[9] N. Yuvaraj, K. Praghash, R. A. Raja, and T. Karthikeyan, “An investigation of garbage disposal electric vehicles (GDEVs) integrated with deep neural networking (DNN) and intelligent transportation system (ITS) in smart city management system (SCMS),” *Wirel. Pers. Commun.*, vol. 123, no. 2, pp. 1733–1752, 2022.

[10] M. Sheikholeslami and Z. Ebrahimpour, “Thermal improvement of linear Fresnel solar system utilizing Al2O3-water nanofluid and multi-way twisted tape,” *Int. J. Therm. Sci.*, vol. 176, p. 107505, 2022.

[11] M. Ghodbane *et al.*, “Energy, financial, and environmental investigation of a direct steam production power plant driven by linear fresnel solar reflectors,” *J. Sol. Energy Eng.*, vol. 143, no. 2, p. 21008, 2021.

[12] J. Surendiran *et al.*, “Segmentation of optic disc and cup using modified recurrent neural network,” *Biomed Res. Int.*, vol. 2022, 2022.

[13] S. Kamel, E. B. Agyekum, T. S. Adebayo, I. B. M. Taha, B. A. Gyamfi, and S. J. Yaqoob, “Comparative analysis of Rankine cycle linear Fresnel reflector and solar tower plant technologies: techno-economic analysis for Ethiopia,” *Sustainability*, vol. 14, no. 3, p. 1677, 2022.

[14] Z. Ebrahimpour, M. Sheikholeslami, and S. A. Farshad, “Radiation and convection treatment of nanomaterial within a Linear Fresnel Reflector unit,” *Eur. Phys. J. Plus*, vol. 136, no. 2, p. 201, 2021.

[15] P. Boito and R. Grena, “Application of a fixed-receiver Linear Fresnel Reflector in concentrating photovoltaics,” *Sol. Energy*, vol. 215, pp. 198–205, 2021.

[16] M. Ghodbane, E. Bellos, Z. Said, B. Boumeddane, A. K. Hussein, and L. Kolsi, “Evaluating energy efficiency and economic effect of heat transfer in copper tube for small solar linear Fresnel reflector,” *J. Therm. Anal. Calorim.*, vol. 143, pp. 4197–4215, 2021.

[17] J. Ma, C.-L. Wang, Y. Zhou, and R.-D. Wang, “Optimized design of a linear Fresnel collector with a compound parabolic secondary reflector,” *Renew. Energy*, vol. 171, pp. 141–148, 2021.

[18] X. Zhao, Z. Chen, S. Yan, T. Ming, Z. Wu, and R. Ma, “Influence of dust accumulation on the solar reflectivity of a linear Fresnel reflector,” *J. Therm. Sci.*, vol. 30, pp. 1526–1540, 2021.

[19] N. Khandelwal, M. Sharma, O. Singh, and A. K. Shukla, “Comparative analysis of the linear Fresnel reflector assisted solar cycle on the basis of heat transfer fluids,” *Mater. Today Proc.*, vol. 38, pp. 74–79, 2021.

[20] A. Barbón, P. F. Ayuso, L. Bayón, and J. A. Fernández-Rubiera, “Non-uniform illumination in low concentration photovoltaic systems based on small-scale linear Fresnel reflectors,” *Energy*, vol. 239, p. 122217, 2022.

[21] J.-J. Men, X.-R. Zhao, Z.-D. Cheng, Y.-K. Leng, and Y.-L. He, “Study on the annual optical comprehensive performance of linear Fresnel reflector concentrators with an effective multi-objective optimization model,” *Sol. Energy*, vol. 225, pp. 591–607, 2021.

[22] A. V. Santos, D. Canavarro, P. Horta, and M. Collares-Pereira, “An analytical method for the optical analysis of Linear Fresnel Reflectors with a flat receiver,” *Sol. Energy*, vol. 227, pp. 203–216, 2021.

[23] H. Beltagy, “The effect of glass on the receiver and the use of two absorber tubes on optical performance of linear fresnel solar concentrators,” *Energy*, vol. 224, p. 120111, 2021.

[24] S. Alam, “Security Concerns in Smart Agriculture and Blockchain-based Solution,” in *2022 OPJU International Technology Conference on Emerging Technologies for Sustainable Development (OTCON)*, 2023, pp. 1–6.

[25] M. M. Khubrani and S. Alam, “Blockchain-Based Microgrid for Safe and Reliable Power Generation and Distribution: A Case Study of Saudi Arabia,” *Energies*, vol. 16, no. 16, p. 5963, 2023.

[26] Z. Ebrahimpour, S. A. Farshad, and M. Sheikholeslami, “Heat transfer within linear Fresnel unit using parabolic reflector,” *Int. J. Numer. Methods Heat Fluid Flow*, vol. 32, no. 8, pp. 2841–2863, 2022.

[27] A. V Santos, D. Canavarro, and M. Collares-Pereira, “The gap angle as a design criterion to determine the position of linear Fresnel primary mirrors,” *Renew. Energy*, vol. 163, pp. 1397–1407, 2021.

[28] G. Wang, Z. Ge, and J. Lin, “Design and performance analysis of a novel solar photovoltaic/thermal system using compact linear Fresnel reflector and nanofluids beam splitting device,” *Case Stud. Therm. Eng.*, vol. 35, p. 102167, 2022.

[29] H. Mahmood and K. Hossin, “Daily, monthly and annual thermal performance of a linear Fresnel reflector to drive an organic Rankine-cycle system,” *Clean Energy*, vol. 5, no. 4, pp. 673–689, 2021.

[30] M. Ghodbane, M. Majdak, and B. Boumeddane, “The efficiency of linear Fresnel reflectors in producing superheated steam for power plant drive,” in *E3S Web of Conferences*, 2021, vol. 323, p. 11.

[31] A. C. Montenon, A. V. Santos, M. Collares-Pereira, F. M. Montagnino, R. Garofalo, and C. Papanicolas, “Optical performance comparison of two receiver configurations for medium temperature Linear Fresnel Collectors,” *Sol. Energy*, vol. 240, pp. 225–236, 2022.

[32] A. Häberle, “Linear fresnel collectors,” in *Solar Thermal Energy*, Springer, 2022, pp. 55–62.

[33] A. Famiglietti, A. Lecuona, M. Ibarra, and J. Roa, “Turbo-assisted direct solar air heater for medium temperature industrial processes using Linear Fresnel Collectors. Assessment on daily and yearly basis,” *Energy*, vol. 223, p. 120011, 2021.

[34] B. Raillani, H. A. L. Ouali, S. Amraqui, M. A. Moussaoui, and A. Mezrhab, “Techno-economic impact of optical soiling losses on solar tower and linear Fresnel reflector power plants: Experimental and numerical investigation,” *Int. J. Green Energy*, vol. 19, no. 15, pp. 1665–1674, 2022.

[35] S. Kiyaee, Y. Saboohi, and A. Z. Moshfegh, “A new designed linear Fresnel lens solar concentrator based on spectral splitting for passive cooling of solar cells,” *Energy Convers. Manag.*, vol. 230, p. 113782, 2021.

[36] S. N. Danish, Z. Almutairi, A. El-Leathy, H. Al-Ansary, Y. Jardan, and S. Alaqel, “Modeling and performance simulation of an innovative concept of linear Fresnel reflector based CSP system,” *J. Therm. Sci.*, vol. 30, no. 5, pp. 1614–1624, 2021.

[37] M. Babu, N. Bhuvanesh, S. S. Raj, and E. Elavarasan, “Design and optimization of linear Fresnel reflector concentrating solar system using particle swarm optimization algorithms,” *Mater. Today Proc.*, vol. 66, pp. 1038–1043, 2022.

[38] M. Sofiane, “Effect of Design Parameters on The Performance of DSG Linear Fresnel Solar Power Plant,” *Int. J. Energy a Clean Environ.*, vol. 22, no. 2, 2021.

[39] Y. Wu *et al.*, “Comparative Study on Heat Flux and Temperature Distribution Performance of Linear Fresnel Collector Based on Uniformity Index,” *J. Therm. Sci.*, vol. 31, no. 3, pp. 678–688, 2022.

[40] M. Kirola, M. Memoria, M. Shuaib, K. Joshi, S. Alam, and F. Alshanketi, “A Referenced Framework on New Challenges and Cutting-Edge Research Trends for Big-Data Processing Using Machine Learning Approaches,” in *2023 International Conference on Smart Computing and Application (ICSCA)*, 2023, pp. 1–5.

ISSN: 2633-4828 Vol. 5 No.3, September, 2023

International Journal of Applied Engineering & Technology

A STUDY ON MEASURING DETERMINANTS OF USAGE OF ONLINE SHOPPING APPLICATIONS AMONG THE USERS OF SOUTH MUMBAI REGION

Dr. Masooma Zaheer Asad Sayed
Assistant Professor (Accountancy), Rizvi College of Arts Science and Commerce, Bandra West, Mumbai 400 050, Maharashtra, India
smasoomaza@gmail.com

ABSTRACT

Online shopping is a structure of e-commerce which empowers shopper to buy goods and services online using internet webpages and mobile applications. The goal of this study is to evaluate determinants of usage of online shopping applications among its users. SEM technique using SMART PLS have been used for the current study. It is seen that Effort expectancy, Hedonic motivation, Performance expectancy and social influence significantly influences shopping decisions. Further studies can be conducted by using moderator construct and building a higher order model.

Keywords: E-shopping, UTAUT, online shopping

INTRODUCTION

The Indian consumer market industry has come a long way from ancient times and has seen several developments in the sector for years. Online shopping is one such part of the retail industry which has gained momentum since its inception in the last decade. Online shopping is beneficial for retailers as well as buyers as for the retails there are no real estate costs and the need to have many premises to sell their goods. It also provides mass customization, enhanced customer services, global reach, and specialized stores. There are various platforms available in India for electronic commerce, such as Flipkart, Amazon, Snapdeal, eBay, Myntra, Meesho, etc., which provide several goods and services. Most of these applications offer electronics, books, groceries, greeting cards, cell phones and accessories, apparel, furniture, various electronic gadgets, and home appliances with a wide variety to select from and purchase.

Online shopping came to India in the early 1990s after the internet was introduced. It gained momentum within a few years of its introduction, and by the year 2000, it was a popular form of shopping that people preferred who had access to the internet. Various websites were established in the initial years; some famous first few are Amazon and Flipkart, Snapdeal, etc. People found this form of shopping to be more convenient and faster than traditional methods of buying goods and services. Online shopping has not just stopped at goods but has ventured into hotel bookings, flight, train, taxi, and bus booking, along with holiday bookings. Although the online shopping method is not free of cost and comes with charges, people are still drawn towards it because it is faster and can be done at the leisure of their homes.

However, there are various pros and cons attached to online shopping. The pros can be listed as it is time and money saving, can be done any time of the day and is available 24x7, provides several reviews which help make decisions for purchase, had a wide variety and that too at the distance of a click, no salesperson is trying to convince you to buy, and the decision can be made without being forced into it; also it gives a lot of privacy, and to the shopper, there are no long waiting hours for bill payments, also provides with a lot of discounts and cashback options, shopping becomes easier when intending to send it to far away friends and relatives as they provide the delivery option. A person does not have to look for courier companies to send their gifts; there are various payment options available, and they can be selected as per the shopper's convenience, such as cash of delivery, mobile wallets, debit or credit cards, etc. There are many cons to online shopping, such as fake advertisements, the quality of the product not being the same as described, delays in delivery, wrong product delivery, payment fraud, return policies not being followed by the companies, etc.

The purpose of conducting this research is to examine the Determinants of usage of online shopping applications among the users of the Mumbai region and to give proper and appropriate suggestive measures to improve the shopping experience of the users.

REVIEW OF LITERATURE

1. **Gehrt, K. C. et al. (2012).** The authors examined the emergence of online shopping in India and the shopping arrangement segments. The study conducted surveys from 536 consumers of online shopping adopting the two-step process. The findings of the results showed that three elements perform an essential role in the emergence of online shopping in India: calibre at any price, influence or amusement, and value distinctiveness. Quality and reputation were the primary online shoppers. The shopping orientations differ through various aspects such as demographics, behavior, and website attribute ratings are very alike; the only difference was seen towards the occupation. The authors believe that future research needs to be concluded to include a comparative study to understand online shopping in India better.
2. **Kim, C. et al. (2012).** The paper examined the factors influencing internet shopping value and customer repurchase determination. The study was conducted on 293 respondents who were classified into two groups: working class and students. The study results showed that the application features and the service quality of the shopping platforms are key factors that affect the indulgent shopping value. The research findings are that service quality plays a vital role in increasing pragmatic and hedonistic shopping values. Also, the results showed that the influence of quality factors on internet shopping values and future repurchase determination varies among the two predefined groups, i.e., the working class and the students.
3. **Natarajan, T. et al. (2018)** The authors examined the arbitrate role of device type and age of users on the intention to use mobile shopping applications. The factors such as perceived usefulness, perceived enjoyment, perceived risk, and perceived ease-to-use were considered. Personal innovativeness and customer satisfaction were also considered; 67 respondents were shortlisted for this study, and the findings of this study showed a significant difference in the responses for the variables; perceived usefulness and enjoyment, intention to use, and satisfaction among the respondents. The authors further concluded that the satisfaction factor plays a vital role in mobile applications depending on the user's age and is different with all age groups.
4. **Natarajan, T. et al. (2017).** The authors researched to understand the purpose to use mobile shopping applications and their influence on price sensitivity. The study was analyzed using the Technology acceptance model (TAM). Three additional variables were added for better analysis of the results: perceived risk, personal innovativeness, and perceived enjoyment. A questionnaire was circulated online to 675 respondents gender, frequency, and experience were used as moderators for all associations. The results of this study indicated that perceived risk and personal innovativeness play an essential role in determining the purchase intention of mobile shopping application users.
5. **Singh, D. P. (2014).** This study aimed to examine the Indian consumers' perception of online shopping, motivation, intention, and information search towards it. The paper also seeks to determine the relationship between the abovementioned three factors. Indian e-commerce market offers a wide variety of opportunities to businesses that are conducted online due to the increase in the buying of products and services. This study showed that utilitarian and hedonic motivation significantly affects online research and shopping intentions. The information search was seen to be the most crucial motivator towards intention for online purchases.
6. **SivaKumar, A., & Gunasekaran, A. (2017).** The paper conducted an pragmatic study on the components that affect the online shopping etiquette of millennial users in India. E-commerce in the country has been growing rapidly and extensively. The main intent of this research is to determine the factors that affect shopping behavior; the respondents of this survey are from the Chennai, Tamil Nadu region. The findings of this research suggested that the benefit of purchasing 24x7, website layout, design, user interface, search engines,

sorting and filter options, safety, and security are some of the determinants that push users toward online shopping.

7. **Thakur, R. (2016).** The author conducted the research focusing on understanding the customers' engagement and loyalty toward using mobile devices for shopping online. The study conducted interviews, surveys, and previous research for the current paper. The findings of this study included growth and recognition of customer engagement as a second-order build-up emerging out of 6 distinct customer experiences: self-connect, time-filler, intrinsic enjoyment, practical, social facilitation, and monetary evaluation. Also, customer engagement is notable in forecasting customer loyalty incorporation with an existing build-up of convenience and satisfaction.
8. **Thamizhvanan, A., & Xavier, M. J. (2013).** The paper examined the determinants of customers' online purchase intention in India to understand the customers' perceptions and motivations toward online purchases. The author points out that the online retail market has been growing since its inception in India at a steady 35 percent and has emerged as a critical sector in the economy. The results of this research are based on 95 complete and valid responses received via an online survey. The findings of this research were that there is a noteworthy relationship between purchase orientation, prior purchases, and online trust in the customer's purchase intention. Moreover, it was also observed that males have higher purchase intentions than females.

OBJECTIVE OF THE STUDY

To evaluate the determinants of usage of online shopping applications among the users of South Mumbai Region

Hypotheses

1. Effort expectancy has positive impact on online shopping among users.
2. Hedonic motivation has effect on online shopping among users.
3. Performance expectancy influences online shopping decisions among users.
4. Social influence affects online shopping decisions among users

RESEARCH METHODOLOGY

Data has been collected from 210 online shopping users using non probability purposive sampling method. As per **Soper, D.S. (2023)** the minimum required sample size at effect size 0.3, desired statistical power level 0.9, latent variable 5, observed variables 20 and probability level 0.05 = 188. The technique applied for the current structural equation model and the tool used for the current study is smart PLS.

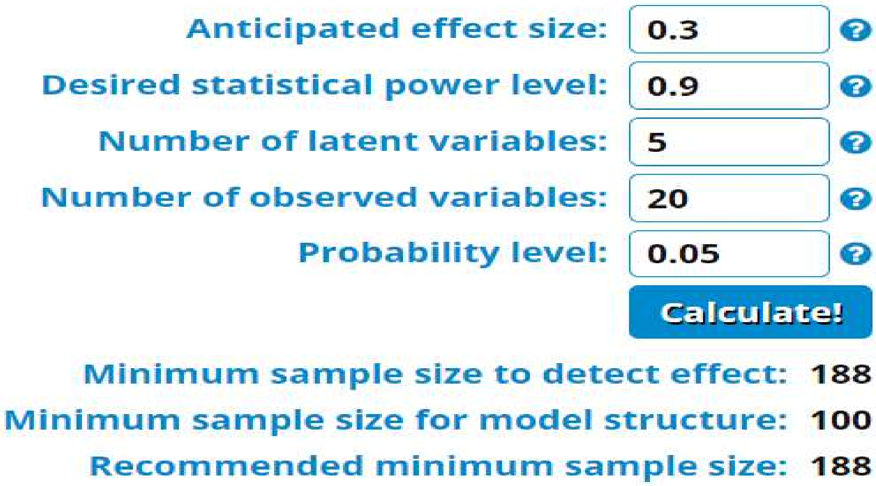

Anticipated effect size: 0.3

Desired statistical power level: 0.9

Number of latent variables: 5

Number of observed variables: 20

Probability level: 0.05

Minimum sample size to detect effect: 188

Minimum sample size for model structure: 100

Recommended minimum sample size: 188

Data Analysis and Interpretation

Figure No: 1 Reliability analysis

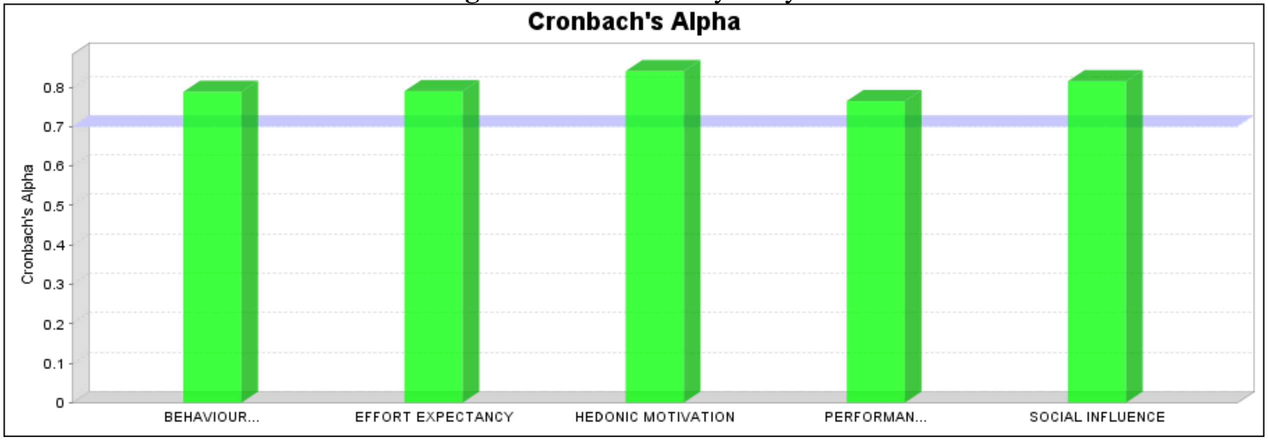

As all the values of cronbach alpha > .70 indicating sufficient corellation between the items.

Figure No: 2 SEM model

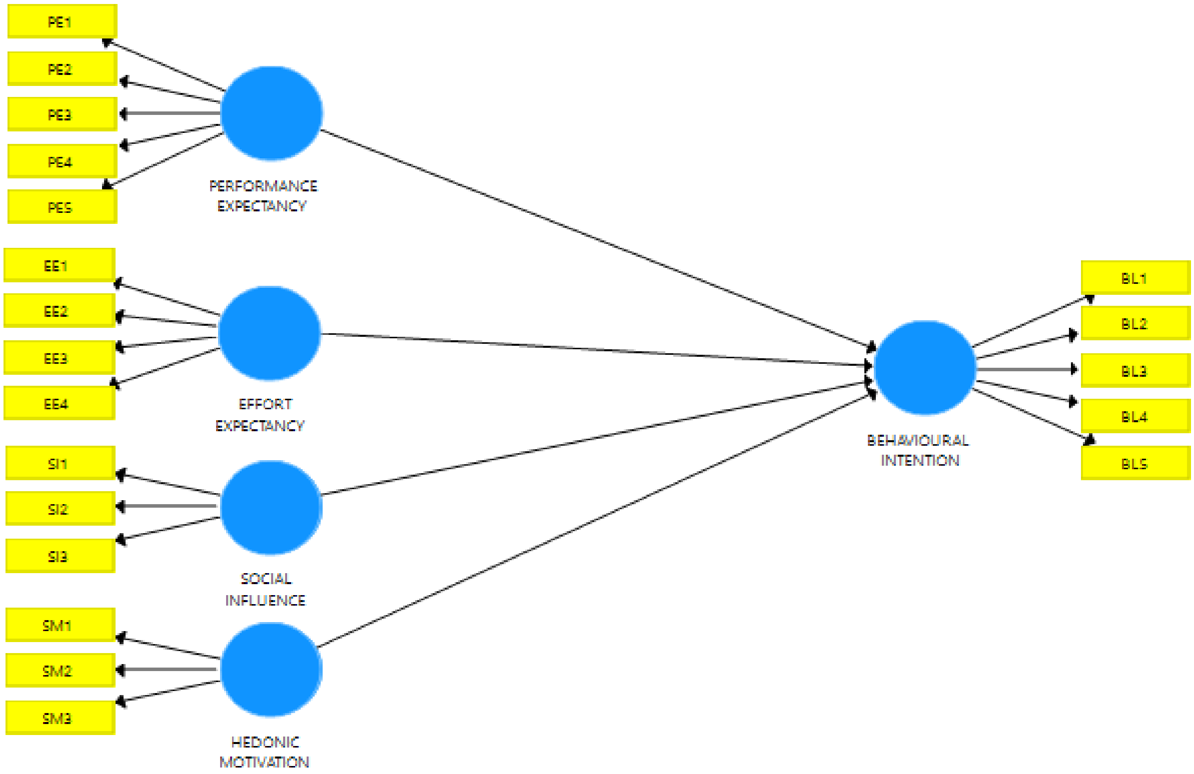

Table No: 1 Hypothesis testing

Path	Beta coefficient	T value	P value
Effort expectancy → Behavioural intention	0.219	5.239	0.000
Hedonic motivation → Behavioural intention	0.166	3.737	0.009
Performance expectancy → Behavioural intention	0.229	5.114	0.000
Social influence → Behavioural intention	0.429	9.148	0.000

P (value) < level of significance 5% thus H1 is accepted in all the cases indicating significance impact of Effort expectancy, Hedonic motivation, Performance expectancy and Social influence on behavioural intention of online shopping.

CONCLUSION

Online shopping is an endeavour or manoeuvre of buying products and services available over the internet. Online shopping has been in the modern world for two decades and has only gained popularity worldwide. There is various website as well as mobile application introduced for online shopping. More and more people have ditched the traditional form of shopping. They have gone towards this modern advanced form of shopping where several stuff is available such as electronics, gadgets, furniture, books, mobile, groceries, apparel, clothing, etc. The focus of this study was to measure determinants of usage of online shopping applications among the users of the Mumbai region, and it was observed that there is a remarkable correlation among behaviour intention, effort expectancy, hedonic motivation, performance expectancy and social influence. People are drawn towards shopping as it gives a larger shelf of goods to select from without having to visit a marketplace, is available 24x7 and shopping can be done at the convenience of a person at the leisure of their home.

REFERENCES

1. Chopdar, P. K., Korfiatis, N., Sivakumar, V. J., & Lytras, M. D. (2018). Mobile shopping apps adoption and perceived risks: A cross-country perspective utilizing the Unified Theory of Acceptance and Use of Technology. *Computers in Human Behavior*, *86*, 109-128.
2. Gehrt, K. C., Rajan, M. N., Shainesh, G., Czerwinski, D., & O'Brien, M. (2012). Emergence of online shopping in India: shopping orientation segments. *International Journal of Retail & Distribution Management*, *40*(10), 742-758.
3. Gong, W., Stump, R. L., & Maddox, L. M. (2013). Factors influencing consumers' online shopping in China. *Journal of Asia Business Studies*.
4. Kim, C., Galliers, R. D., Shin, N., Ryoo, J. H., & Kim, J. (2012). Factors influencing Internet shopping value and customer repurchase intention. *Electronic commerce research and applications*, *11*(4), 374-387.
5. Natarajan, T., Balasubramanian, S. A., & Kasilingam, D. L. (2017). Understanding the intention to use mobile shopping applications and its influence on price sensitivity. *Journal of Retailing and Consumer Services*, *37*, 8-22.
6. Natarajan, T., Balasubramanian, S. A., & Kasilingam, D. L. (2018). The moderating role of device type and age of users on the intention to use mobile shopping applications. *Technology in Society*, *53*, 79-90.
7. Singh, D. P. (2014). Online shopping motivations, information search, and shopping intentions in an emerging economy. *Asian Journal of Business Environment*, *4*(3), 5-12.

8. Sinha, P., & Singh, S. (2014). Determinants of consumers' perceived risk in online shopping: A study. *Indian Journal of Marketing*, *44*(1), 22-32.

9. SivaKumar, A., & Gunasekaran, A. (2017). An empirical study on the factors affecting online shopping behavior of millennial consumers. *Journal of Internet Commerce*, *16*(3), 219-230.

10. Thakur, R. (2016). Understanding customer engagement and loyalty: a case of mobile devices for shopping. *Journal of Retailing and consumer Services*, *32*, 151-163.

11. Thakur, R., & Srivastava, M. (2015). A study on the impact of consumer risk perception and innovativeness on online shopping in India. *International Journal of Retail & Distribution Management*.

12. Thamizhvanan, A., & Xavier, M. J. (2013). Determinants of customers' online purchase intention: an empirical study in India. *Journal of Indian Business Research*.

Journal of Advanced Zoology
ISSN: 0253-7214
*Volume **44** Issue **S8 Year 2023** Page421-**424***

Harvesting Prosperity: A Comparative Analysis Of Karnataka's Agricultural Development Landscape (2021-22)

Dr. Dattatraya Parhad[1]*

*[1]*Associate Professor, Department of Mathematics and Statistics Rizvi College of Arts, Science and Commerce Bandra West Mumbai 400050 University of Mumbai Email: parhadd@rizvicollege.edu.in*

****Corresponding author:** Dr. Dattatraya Parhad*
**Associate Professor, Department of Mathematics and Statistics Rizvi College of Arts, Science and Commerce Bandra West Mumbai 400050 University of Mumbai Email: parhadd@rizvicollege.edu.in*

***Abstract*:**

In India's southwest, Karnataka is the eighth-largest state. It is the industry leader in floriculture and horticulture. With 23.82 lakh hectares under cultivation, the State holds the top spot and accounts for 9.01 percent of the nation's total horticultural area. Its reputation as a producer of horticulture, cash crops, food crops, and plantations is widely acknowledged. Altitude and distance from the sea influence the interaction of topographic, climatic, and edaphic variables that result in a highly diversified and distinct ecosystem.

The current study aims to analyse the data that the Karnataka government has released regarding 27 indicators, using 31 districts as the study's units. The Composite Index Method is used to construct the agricultural development index, which is used to rank the districts.

The study revealed that whereas Tumakuru and Belgavi are poorly developed, the districts of Udupi, Bangalore (Rural), Kodagu, and Ramanagara are developed districts in terms of agriculture. Every other district is classified as a developing district.

Introduction:

In the fields of floriculture and horticulture, Karnataka leads the way. The entire area and production of horticultural crops in India are documented in the "Agriculture Cooperation & Farmers Welfare database - 2020" as being 264.57 lakh hectares and 3199.69 lakh M.T., respectively. With 23.82 lakh hectares under cultivation, or 9.01 percent of the nation's total horticultural area, Karnataka State has taken first place. The state exports more flowers and gherkins than any other state in the union. India's second-largest producer of maize, safflower, grapes, pomegranates, and onions, Karnataka is also the country's top producer of coffee, raw silk, sandalwood, ragi (finger millet), sunflower, and tomato. In India, the state is in fifth place for the total area dedicated to horticulture.

It ranks third in the production of fruit crops and fifth in the production of vegetable crops. In addition, it produces the most tropical fruits, fragrant and medicinal crops, and spices. After Gujarat, it is the second-largest milk-producing state.

The state mostly cultivates rice-based crops. Ragi, bajra, cotton, groundnut, jowar, and maize are important agricultural substitutes for rice. Wheat, minor millets, and pulses such as tur, Bengal gramme, horse gramme, black gramme, green gramme, and cowpea are additional significant crops. Groundnut, sesame, sunflower, soybean, and sunflower are examples of oilseeds. In the eastern region, tobacco is a commercial crop; in the northwest, cotton is a commercial crop. Other significant crops include cashew, coconut, areca nut (southern region), cardamom, and chilies.

Other major crops include cashew, coconut, areca nut (southern region), cardamom, and chilies. While maize is mainly farmed in the state's northern part, the Western Ghats are famous for its coffee and tea plantations. The coastal region is ideal for growing fruit orchards because of its climate.

Karnataka has a long history of sericulture, and the state places a high value on silk. The tale of Soil to Silk & Fabric is intriguing. In the field of sericulture, women perform 60% of the labor. The silk and sericulture industries provide significant employment opportunities for around 12 lakh households in Karnataka.

5.76 lakh hectares of inland water resources, 8000 hectares of brackish water, 2.38 lakh hectares of waterlogged and alkaline terrain, 313.02 kilometers of coastline, and 27,000 sq. km of continental shelf make up Karnataka's water resources.

Karnataka produced about 2.0 lakh tonnes of fish in the early 1980s, and by the mid-1990s, it was producing over 3.0 lakh tonnes. Over the past five years, the average annual fish production has been approximately 5.95 lakh tonnes, with the marine sector accounting for 66% of the total and the inland sector for 34%.

Karnataka's forest environment is distinct and exceptionally diverse. It is an essential component of the environment's natural resources. There are several types of vegetation such as semi-evergreen, dry deciduous, moist deciduous, sholas, prickly shrubs, and coastal mangroves. They are a storehouse of abundant biodiversity at the gene, species, and ecosystem levels. The interaction of topographic, climatic, and edaphic variations determined by height and distance from the sea results in distinct forest ecosystems.

Karnataka is home to 25% of the nation's elephant population and 10% of its tigers. About 4500 flowering plant species, 600 bird species, 160 animal species, 160 reptile species (including turtles, snakes, lizards, and crocodiles), 70 frog species, and 800 fish species are found in the state. These numbers provide a decent picture of the state's richness of flora and animals.

Karnataka state is divided into four revenue divisions and 31 districts as follows: -

Table 1: Districts and Revenue Divisions of Karnataka

Belagavi Division	Bengaluru Division	Kalaburagi Division	Mysuru Division
Bagalkote	Bengaluru Rural	Ballari	Chamarajanagara
Belagavi (Headquarters)	Bengaluru Urban (Headquarters)	Bidar	Chikkamagaluru
Dharwada	Chikkaballapura	Kalaburagi (Headquarters)	Dakshina Kannada
Gadaga	Chitradurga	Koppala	Hassan
Haveri	Davanagere	Raichuru	Kodagu
Uttara Kannada	Kolar	Vijayanagara	Mandya
Vijayapura	Ramanagara	Yadagiri	Mysuru (Headquarters)
	Shivamogga Tumakuru		Udupi

List of districts of Karnataka - Wikipedia

Research Methodology: -

Composite Index Method

Consider the set of n units for the group of k indicators. This can be represented by a matrix
$[X_{ij}]$,
$i=1,2,3,$ -------, n and $j= 1,2,3,$ -------, k.

To overcome the difficulty in dimensions and unit of dimensions, the data is standardized as follows.

$$Z_{ij} = \frac{X_{ij} - \bar{X}_j}{6j}$$

Where σ_j = S.D of X_j, $j = 1, 2, 3,$ --------- , k
X_j = Mean of X_{ij} .

$[z_{ij}]$ denotes the matrix of standardized indicators. The best value of each indicator (with max / min standardized value depending upon the direction of indicator) is identified and from this, the deviations of the value for each unit are taken for all indicators in the following manner:

$$C_j = \left\{ \Sigma \left(z_{ij} - z_{oj} \right)^2 \right\}^{1/2}$$

Where z_{oj} is the standardized value of the j^{th} indicator of the best unit and Ci denotes the pattern of development of ith unit. The composite index of development is obtained through the following formula:

$$\bar{C} = \frac{\Sigma C_i}{n}$$

The value of the composite index is non-negative and lies between 0 and 1. The value closer to 0 indicates higher level of development while the value closer to 1 indicates the lower level of development.

The units are ranked by the composite indices scored by the units. The composite indices are arranged in descending order and the units are ranked by the position obtained from their composite index.

The units are further classified into three categories namely developed, developing and low developed. The units scoring the composite indices more than Mean + SD of the indices are treated as low developed, the units scoring the indices ranging between Mean + SD and Mean - SD are treated as developing and the units scoring less than Mean - SD are considered as the developed units.

The correlations are calculated between the composite indices scored by all the units in a particular time stage for all the sectors and the composite indices scored by all the units for a particular sector in all time stages.

Analysis:

-The Directorate of Economics and Statistics, Government of Karnataka published the handbook "Karnataka At A Glance" for the Year 2021-22. The data related to agricultural development for the following 27 indicators and 31 districts as the units, is considered for this study. The data and analysis can be verified at the links provided in the citation 12 to 13 in the references below.

1. Percentage of Forest Area to Geographical Area
2. Percentage of Land not available for Cultivation to Geographical area
3. Percentage of Permanent Pasture to Geographical Area
4. Percentage of Net area Sown to Total Geographical Area
5. Percentage of Net area Irrigated to Net area sown
6. Percentage of area under food grains to Total area sown
7. Percentage of area under oil seeds to Total Area sown
8. Total Area under Fruits (In Hectares)
9. Total Area under Vegetables (In Hectares)
10. Total Area under Cotton (In Hectares)
11. Total area under Sugarcane (In Hectares)
12. Total Area under Condiments and Spices (In Hectares)
13. Total area under Coconuts (In Hectares)
14. Total area under Areca Nuts (In Hectares)
15. Percentage of food grain production to the state total
16. Cold storage Capacity for Horticulture in Tonnes
17. Percentage of Chemical fertilizers distributed to the State Total
18. Kisan Credit Card Distributed
19. Number of Soil Health card Distributed
20. Percentage of seeds distributed to the State total
21. No. of Regulated Markets
22. No. of Regulated submarkets
23. No. of Mandis linked to electronic markets
24. Percentage of Marginal land holders to total land holders (<1 Hectares)
25. Percentage of small landholders to total land holders (1-2 hectares)
26. Percentage of Livestock to state Total
27. Total No. of veterinary Hospitals/Dispensaries

The data is analyzed using the Composite Index method as explained in the Research Methodology and further the units are ranked on the basis of development. The units are further classified as Developed, developing and Low developed.

Table 2: District-wise Composite Indices of Agricultural Development

District	Ci	District	Ci
Udupi	0.3242	Mandya	0.5504
Bengaluru (Rural)	0.3509	Bidar	0.56
Kodagu	0.3972	Davanagere	0.5693
Ramanagara	0.4073	Kalburgi	0.5728
Chamarajanagara	0.4167	Uttar Kannada	0.5764
Chikkaballapura	0.4301	Chitradurga	0.5841
Dharwada	0.4498	Haveri	0.588
Vijayanagara	0.4575	Shivamogga	0.5932
Bengaluru(Urban)	0.4616	Haasan	0.5949
Kolara	0.4733	Bagalkote	0.5975
Chikkamangaluru	0.49	Raichuru	0.624
Gadag	0.4942	Vijayapura	0.6375
Dakshina Kannada	0.5084	Tumakuru	0.7269
Koppal	0.5115	Belgavi	0.9462
Yadgiri	0.5133	Mean	0.5312
Ballari	0.5185	**SD**	**0.1172**
Mysuru	0.543	**Mean - SD**	**0.4141**
		Mean + SD	**0.6484**

Conclusions:

This research offers a comprehensive examination of Karnataka's agricultural development, elucidating disparities among districts. The findings provide valuable insights for policymakers and stakeholders to tailor interventions for the overall advancement of the state's agriculture.

The study found that, the districts of Udupi, Bangalore (Rural), Kodagu and Ramanagara are developed districts in agriculture while Tumakuru, Belgavi these districts are low developed. Remaining all the districts fall under the developing districts category.

References: -

1. Shivakumar, B. G., & Anantha, K. H. (2021). "Agricultural Development and Cropping Pattern in Karnataka: An Empirical Analysis." International Journal of Agricultural and Biological Sciences, 7(2), 21-29.
2. Government of Karnataka. (2021). Karnataka State Agriculture Policy 2020-25. [Official Policy Document]
3. Ministry of Agriculture & Farmers Welfare, Government of India. (2022). Horticultural Statistics at a Glance 2021. [Government Publication]
4. Department of Agriculture, Government of Karnataka. (2022). Karnataka Agriculture: Vision 2025. [Official Report]
5. Kulkarni, S. A., & Doddabasavraj, K. (2021). "Economic Analysis of Agricultural Development in Karnataka." International Journal of Agriculture, Environment, and Biotechnology, 14(2), 611-618. [Academic Paper]
6. Karnataka State Natural Disaster Monitoring Centre (KSNDMC). (2022). Agro-Meteorological Advisory Bulletin for Karnataka State. [Official Bulletin]
7. Institute for Social and Economic Change (ISEC). (2022). Karnataka Agriculture and Allied Sector: An Economic Overview. [Research Report]
8. University of Agricultural Sciences, Bengaluru. (2022). Annual Report 2021-22. [University Report]
9. Kumar, S. B., & Hegde, R. (2021). "A Study on Horticulture Development in Karnataka." Journal of Horticulture, 8(1), 35-42. [Academic Paper]
10. Karnataka State Department of Horticulture. (2022). Annual Report 2021-22. [Government Report]
11. Raju, R. V., & Raghavan, K. (2021). "Challenges and Opportunities in Karnataka Agriculture: A Review." Indian Journal of Agricultural Research, 55(4), 345-356. [Academic Paper]
12. des.karnataka.gov.in/storage/pdf-files/PTC/KAG 2021_22.pdf
13. https://drive.google.com/drive/folders/1IHAz6BcSgTcf1X1_PuiyDxyG9xckDEqe?usp=drive_link

Educational Administration: Theory and Practice
2023, 29(4), 1996-2000
ISSN: 2148-2403
https://kuey.net/

Research Paper

A Comprehensive Methodology For Measuring Course, Program, And Program-Specific Outcomes In Higher Education

Dr. Dattatraya Parhad[1*]

[1*]Department of Mathematics and Statistics, Rizvi College of Arts, Science and Commerce Bandra West Mumbai 400050, Affiliated to University of Mumbai. Tel: +91 9657725810 E-mail: parhadd@rizvicollege.edu.in

Citation: Dr. Dattatraya Parhad, (2023), A Comprehensive Methodology For Measuring Course, Program, And Program-Specific Outcomes In Higher Education, *Educational Administration: Theory and Practice, 29(4), 1996-2000*
Doi: 10.53555/kuey.v29i4.6806

ARTICLE INFO

ABSTRACT

The accurate measurement of Course Outcomes (CO), Program Outcomes (PO), and Program Specific Outcomes (PSO) is crucial for continuous improvement in educational programs. Traditional methods often lack the precision and comprehensive analysis required to fully assess these outcomes. This paper proposes a novel methodology that integrates advanced statistical techniques with qualitative assessment tools to provide a more robust framework for measuring CO, PO, and PSO attainment. The proposed methodology aims to enhance the accuracy, reliability, and validity of the assessment processes in higher education institutions.

Keywords: Course Outcomes (CO), Program Outcomes (PO), Program Specific Outcomes (PSO), Educational Assessment, Quantitative Metrics, Qualitative Assessment, Mixed-Methods Approach, Higher Education, Learning Outcomes, Curriculum Design, Statistical Techniques, Continuous Improvement, Holistic Evaluation, Accreditation

1. Introduction

Ensuring that learners achieve desired learning outcomes is paramount in higher education. Course Outcomes (CO), Program Outcomes (PO), and Program-Specific Outcomes (PSO) are key indicators of educational effectiveness. However, current measurement practices often face challenges related to standardization, accuracy, and comprehensive assessment. This paper introduces a new methodology designed to address these challenges, offering a more holistic and precise approach to outcome measurement.

1.1 Problem Statement

Existing methods for measuring CO, PO, and PSO attainment often fall short in providing detailed and accurate analysis. Issues such as lack of standardization, insufficient data integration, and inadequate consideration of qualitative factors lead to incomplete assessments. A methodology that incorporates quantitative metrics and integrates qualitative evaluations is needed to better capture the multifaceted nature of educational outcomes.

1.2Importance of the Problem

Accurate assessment of CO, PO, and PSO is fundamental to maintaining and enhancing the quality of education. These measurements are essential for accrediting bodies, curriculum developers, and educators to ensure that educational programs meet their objectives and effectively prepare learners for their future careers. Inaccurateor incomplete assessments can lead to a misalignment between educational goals and actual student performance, ultimately affecting the institution's reputation and learners' professional readiness. By developing a more reliable and comprehensive methodology, we can significantly improve quality assurance processes in higher education.

1.3Objectives

1. To develop a comprehensive framework for measuring CO, PO, and PSO attainment.
2. To enhance the accuracy, reliability, and validity of outcome measurement processes.
3. To provide actionable insights for continuous improvement in educational programs.

2. Review of Literature

2.1Literature review

The literature on educational assessment highlights various methodologies for measuring learning outcomes. Traditional approaches often rely heavily on quantitative metrics such as exam scores and survey results. However, recent studies suggest that combining quantitative data with qualitative evaluations, such as student feedback and peer reviews, can provide a more nuanced understanding of outcome attainment. This paper builds on these insights, proposing a methodology that leverages both types of data to offer a more comprehensive assessment framework.

2.2 Relation to Previous Work

Previous research has predominantly focused on quantitative measures, with studies by Biggs and Tang (2011) and Black and Wiliam (1998) emphasizing metrics such as test scores and course completion rates. However, these approaches often overlook the rich, contextual information that qualitative data can provide. Creswell and Creswell (2017) highlighted the potential of mixed-methods approaches, combining qualitative and quantitative data to enhance assessment depth and breadth. This paper extends these insights by integrating advanced statistical techniques with qualitative assessments to create a more robust and holistic methodology for measuring CO, PO, and PSO attainment.

3. Research Methodology

3.1The Methodology in Practice

In the recent years, the institutions are measuring the CO/PO/PSO attainment in which the attainment level is calculated in three parts

(i) CO attainment at Semester End Examination (SEE)
(ii) CO attainment at Continuous Internal Assessment (CIA)
(iii) CO attainment level in Course exit survey The steps involed in the process are as follows: -

a) Design of CO and PO/PSO with the help of Bloom's Taxonomy

The CO's are designed based on the expectations from the learner after completing the course. It explains what knowledge gained by the student, what is the understanding level achieved by the learner, what skills are developed by the learner, how the learner can apply the knowledge for a creation purpose

b) Mapping of CO and PO/PSO using the known correlations between them

The facilitator decides the correlation between the CO and PO/PSO on the three-level scale, based on the understanding and experience of the facilitator.
Level 1: if there is slight correlation Level2: if there is moderate correlationLevel 3: if there is strong correlation Level '-': if there is no correlation

c) Course attainment level calculations

The facilitator then analyse the question paper and Marksheet of Semester end exam for the mapping of questions with Cos and the number of learners who score the marks in that question more or equal to the desire (p%). The CO is supposed to be attained if the student scores more or equal to p%. The attainment level is calculated by the formula:

$$\text{Percentage of leaners who attained the CO}(a) = \frac{\text{Number of learners who score more or equal to p\%}}{\text{Total number of learners who atempted the question}} \times 100$$

The facilitator then decides the CO attainment level with following criteria:Level 1: $0 \leq a < q$

Level 2: $q \leq a < r$
Level 3: $r \leq a \leq 100$
The percentages p, q and r are to be decided by the facilitator according the difficulty level of the course and question paper as well as the academic, social and financial background of the learners.

d) PO/PSO attaimnet level calculations

PO/PSO attainment can be computed for a batch using following formula:

$$\text{PO / PSO ATTAINMENT} = \frac{(\text{ CO attainment } * \text{ Co} - \text{PO/PSO mapping })}{\text{maximum correlation strength}}$$

3.2 Proposed Methodology and Theoretical Implications

The proposed methodology involves a multi-step process:

a) Design of CO and PO/PSO with the help of Bloom's Taxonomy

The facilitator will decide the Course outcomes depending upon the level achieved by the learner on the scale of Bloom's taxonomy from L1 to L6 as follows:

L1: Remember
L2: UnderstandingL3: Apply
L4: Analyse L5: EvaluateL6: Create

Maximum six Course outcomes will be designed on the basis of expected level of achievement on the completion of the course.

b) Mapping of CO and PO/PSO using the known correlations between them

The facilitator will rate the CO with PO/PSO on the scale of 0 to 1, both inclusive, say l1 to l6 depending upon the strength of relationship between each CO with each PO/PSO. The table will have all the column sums equal to 1.

c) Course attainment level calculations

The facilitator then analyse the question paper and Marksheet of Semester end exam for the mapping of questions with COs and the number of learners who score the marks in that question more or equal to the average marks. The level of attainment of CO will be categorized as follows:

Level 1: α% of the learners scored marks more or equal to the average marks obtained by the learners Level 2: β% of the learners scored marks more or equal to the average marks obtained by the learners Level 3: γ% of the learners scored marks more or equal to the average marks obtained by the learners

d) PO/PSO attaimnet level with each Course

Calculate the data for the calculation of PO/PSO attainment as follows:

S1: If p% of learners scored the marks more or equal to the average marks in Question related to CO1 S2: If p% of learners scored the marks more or equal to the average marks in Question related to CO2S3: If p% of learners scored the marks more or equal to the average marks in Question related to CO3S4: If p% of learners scored the marks more or equal to the average marks in Question related to CO4S5: If p% of learners scored the marks more or equal to the average marks in Question related to CO5S6: If p% of learners scored the marks more or equal to the average marks in Question related to CO6 PO/PSO attainment can be computed for a batch using following formula:

$$\text{PO/PSO } ATTAINMENT = \frac{\sum l.s}{\sum l}, \sum l = 1$$

Here are a few specific recommendations while applying this method:

1. Consistency in scales: Ensure that the scales used for correlation and attainment levels are consistent throughout the methodology.

2. Clear definitions: Clearly define and justify the scales and criteria (e.g., values of p, q, r, α, β, γ and the maximum correlation strength).

3. Sum of the correlations: The column sum represents the total contribution of each course outcome amongst the PO/PSO of the program. So, the Sum of all these correlation coefficients needs to be 1 forthe uniformity and it is also requirement of the statistical tool. The facilitator needs to make sure that the column sum must be equal to 1.

e) Over-all PO/PSO attainment Level

The facilitator can frame a table showing the correlation strength of each course with each of the PO/PSO. Let the correlation strengths of the PO/PSO are denoted by C1, C2 etc. where the column sum must be equal to 1 and the corresponding PO/PSO attainment levels are denoted by L1, L2, etc.

The over-all PO/PSO attainment level can be calculated as follows:

$$\text{Over-all PO/PSO } attainment = \frac{\sum C.L}{\sum C}, \sum C = 1$$

The same methodology can be adopted for the Internal as well as the Semester end examination and Final PO/PSO attainment level can be calculated by the formula

$$\text{Final PO/PSO } attainment = x \times a + y \times b$$

where x, y denotes weightages for the Internal and Semester examinations and a, b denotes the over-all attainment in internal and Semester examination respectively.

4. Conclusions:

4.1 Summary of Conclusions

In this research, I have examined the current practices for measuring the attainment of Course Outcomes (CO), Program Outcomes (PO), and Program Specific Outcomes (PSO) within educational institutions. The existing methodology, which involves the calculation of attainment levels based on Semester End Examinations (SEE), Continuous Internal Assessment (CIA), and Course Exit Surveys, has provided a structured approach to evaluating student performance. However, it has revealed areas for potential enhancement.

The proposed methodology builds upon the foundation of Bloom's Taxonomy, utilizing a systematic approach to design COs and PO/PSOs, map them accurately, and calculate attainment levels with greater precision. By introducing a refined correlation scale and employing a comprehensive method for evaluating student performance through various assessment metrics, this methodology aims to provide a more detailed and nuanced understanding of learner achievements.

Key improvements in the proposed methodology include:

1. **Enhanced CO and PO/PSO Design:** By leveraging Bloom's Taxonomy, the COs are crafted to reflect a comprehensive range of cognitive skills, from basic knowledge recall to complex creation andevaluation tasks. This ensures that the learning outcomes are aligned with the expected educational objectives and skillsets required in real-world applications.
2. **Accurate Correlation Mapping**: The introduction of a more granular scale for mapping COs to POs/PSOs allows for a more precise assessment of the relationships between course outcomes and program objectives. This helps in identifying specific areas where the curriculum can be improved to better align with program goals.
3. **Refined Attainment Level Calculations**: The new criteria for determining attainment levels basedon average marks provide a clearer and more standardized measure of student performance. This adjustment addresses the variability in difficulty levels across different courses and assessments, leading to more reliable attainment data.
4. **Comprehensive PO/PSO Attainment Calculation**: The revised formula for calculating PO/PSO attainment incorporates multiple data points, ensuring that the overall program outcomes are reflective of a diverse range of student achievements across various COs. This holistic approach offersa more accurate depiction of program effectiveness.

In conclusion, the proposed methodology offers a robust framework for assessing educational outcomes with improved accuracy and detail. By adopting this approach, institutions can gain deeper insights into student performance, enabling targeted interventions and curriculum enhancements to foster better educational outcomes. This refined methodology not only supports continuous improvement in teaching and learning processes but also ensures that educational programs remain aligned with the evolving needs of learners and the demands of the professional landscape.

4.2 Practical Implications

Implementing the proposed methodology has several practical implications for higher education institutions. Firstly, it can enhance the accuracy and reliability of outcome assessments, providing a clearer picture of student learning and program effectiveness. This, in turn, can help institutions make more informed decisions about curriculum design and teaching strategies. Secondly, the methodology's integration of qualitative data ensures that the assessments are more holistic, capturing the full spectrum of student experiences and learning outcomes. Lastly, the actionable insights derived from this comprehensive assessment can guide targeted interventions, ultimately leading to improved educational quality and student performance. Institutions can also use the findings to meet accreditation requirements more effectively and demonstrate their commitment to continuous improvement.

Acknowledgements:

I would like to express my gratitude to my colleagues at the Department of Mathematics and Statistics, Rizvi College of Arts, Science and Commerce, for their support and contributions to this research. Special thanks to the learners who participated in the pilot study, providing invaluable feedback and data.

References

1. Biggs, J., & Tang, C. (2011). Teaching for Quality Learning at University. McGraw-Hill Education.
2. Black, P., & Wiliam, D. (1998). Assessment and Classroom Learning. Assessment in Education: Principles, Policy & Practice, 5(1), 7-74.
3. Creswell, J. W., & Creswell, J. D. (2017). Research Design: Qualitative, Quantitative, and Mixed Methods Approaches. Sage publications.
4. Anderson, L. W., & Krathwohl, D. R. (2001). A Taxonomy for Learning, Teaching, and Assessing:A Revision of Bloom's Taxonomy of Educational Objectives. Longman.

Chemistry Africa
https://doi.org/10.1007/s42250-023-00587-6

ORIGINAL ARTICLE

A Novel Ultrasound-Assisted Approach for the Synthesis of Biscoumarin and Bislawsone Derivatives Using rGO/TiO_2 Nanocomposite as a Heterogeneous Catalyst

Sarfaraz Shaikh[1,2] · **Ishita Yellapurkar**[1] · **Sonal Bhabal**[1] · **M. M. V. Ramana**[1] · **Julekha A. Shaikh**[3]

Received: 7 November 2022 / Accepted: 3 January 2023

Abstract

In the present study, an efficient and eco-friendly protocol for the syntheses of biscoumarin and bislawsone derivatives is reported. The reactions are carried out in the presence of the rGO/TiO_2 nanocomposite in an ethanol/water solvent system under the influence of ultrasonication. The structural features of the synthesized reduced graphene oxide (rGO) powder and the catalyst were investigated using FTIR, XRD and Raman characterization techniques, and the morphological analysis is achieved by SEM, TEM imaging and EDX spectroscopy. A detailed examination of the effects of various reaction parameters on the product yield was conducted to develop an optimized procedure for synthesizing several biscoumarin and bislawsone derivatives. The products were characterized by FTIR, ^{1}H NMR, Mass spectrometry, and elemental analysis. The significance of this novel protocol is augmented by its notable attributes, namely, shorter reaction times, exceptional product yields, ambient reaction conditions, use of ultrasonication to expedite the reaction, and reusability of the catalyst for up to five cycles. Thus, the environment-friendly nature of the current method abides by the postulates of Green Chemistry.

Graphical Abstract

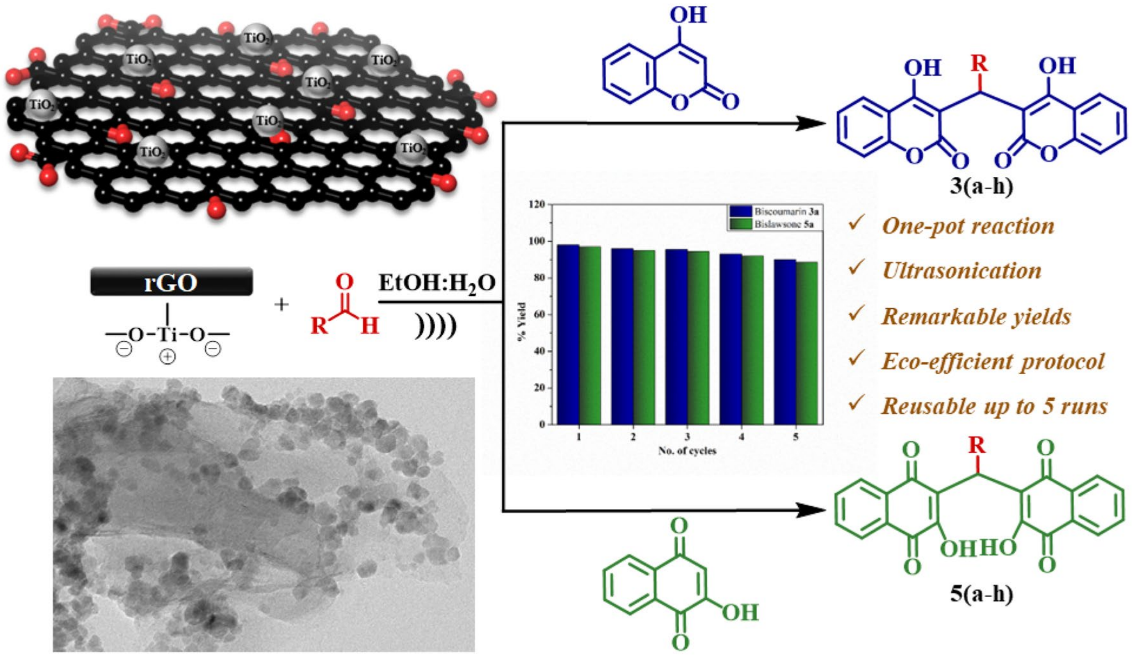

Keywords Catalysis · rGO/TiO_2 · Biscoumarin · Bislawsone · Ultrasonication

---

Extended author information available on the last page of the article

1 Introduction

Multicomponent reactions (MCRs) are essentially one-pot processes involving three or more components undergoing sequential reactions to yield a single product [1]. Operational simplicity, molecular diversity, atom economy, and convergence of simple starting materials into complex structures grant MCRs a significant status in the world of synthetic organic chemistry [2]. In adherence to the principles of Green Chemistry, numerous catalytic methodologies have been developed for carrying out organic transformations via the MCR route [3]. A plethora of novel methods have been developed for most MCRs that employ heterogeneous catalysts, considering their inherent advantages over homogeneous systems [4, 5]. The use of nanoparticles as catalyst has recently received notable recognition owing to their unique attributes, such as their ability to withstand high temperatures, high recyclability, fine-tuning of the nanomaterial, and the environmentally friendly nature of the catalytic protocol. Thus, nanocatalysis is considered an alternative approach to conventional organic synthesis. The amalgamation of nanocatalysts and MCRs is an advanced strategy for obtaining targeted products with high selectivity within a short period of time [6].

The efficient use of metal oxide nanoparticles as heterogeneous catalysts in MCR has been extensively reported in the literature [7]. To further enhance the sustainability of the experimental protocol, immobilization of the nanocatalyst on a solid support, such as reduced graphene oxide (rGO), has proven to be beneficial [8, 9]. In particular, the rGO/TiO_2 nanocomposite has drawn increasing attention due to its promising features, such as chemical inertness in both acidic and basic media, structural flexibility, and large surface area [10–12]. Comprehensive research has been carried out evaluating the photocatalytic characteristic of rGO/TiO_2 nanocomposite, including dye degradation [13] [14], degradation of VOCs [15] and organic pollutants [16], bisphenol A removal [17], pesticide degradation [18], light-induced selective oxidation [19], etc. However, the use of the nanocomposite to catalyze an MCR has not yet been reported.

Biscoumarins constitute an important class of oxygen-containing heterocycles and are well known for their versatile biological applications, including antibacterial [20], antiviral [21], antimicrobial [22], antioxidant [23], anticancer [24], anticoagulant [25] and enzyme inhibition [23]. Lawsone, 2-hydroxy-1,4-naphthoquinone or hennotannic acid, is the principal dye found in henna leaves (*Lawsonia inermis*) [26]. Traditionally, it has been used in cosmetics as hair dye, tattoo dye, and body paint. Bislawsone derivatives are bridge-substituted dimers (usually with a phenyl moiety) of lawsone and have significant pharmacological applications. They are known to exhibit a wide variety of biological activities, including antifungal, antioxidant [27], antileishmanial [28], antibacterial [29], and inhibitory effects on H5N1 neuraminidase [30] and HIV-1 integrase [31]. There are a number of synthetic protocols reported for biscoumarin derivatives using TBAB [32], sodium dodecyl sulfate [33], $RuCl_3$ [34], heteropolyacids [35], ionic liquid [36] and bislawsone derivatives using DMAP [37], camphor sulfonic acid [38], humic acid [39], lipase [40], LiCl [41], LiCl coupled with ultrasound or microwave irradiation [42], amino acids [29], sulfamic acid [43] and chitosan [44]. However, these methods suffer from several disadvantages, such as long reaction times, difficult product isolation, no reusability, and inadequate product yields. This necessitates the development of a high-yielding, environmentally benign protocol for the synthesis of biscoumarin and bislawsone.

A practical alternative to conventional synthetic methods is using high-energy sources, such as ultrasonication, to accelerate chemical reactions [45]. This high energy causes instantaneous generation and collapse of cavitation bubbles, thereby increasing the temperature and pressure of the reaction medium [46]. Thus, coupling ultrasonication with a nanocatalyst provides an eco-friendly pathway for organic synthesis. Herein, we report the ultrasound-assisted one-pot synthesis of biscoumarin and bislawsone derivatives catalyzed by rGO/TiO_2 nanocomposite. The catalyst was successfully characterized by FTIR, XRD, Raman, SEM, TEM and EDX techniques. Further, the biscoumarin and bislawsone derivatives were synthesized and characterized by FTIR, ^{1}H-NMR, Mass spectrometry and elemental analysis.

2 Experimental

2.1 Materials and methods

Graphite powder, TiO_2 nanopowder and all other chemicals were procured from Sigma Aldrich (India) and used directly without purification. FTIR spectroscopy was performed on Perkin Elmer, Frontier equipment with ATR. X-ray Diffraction studies were carried out on a Shimadzu Maxima 7000 S diffractometer (USA), using Cu K_α radiation in the 2θ range of 10^o to 80^o at a scanning speed of 5^o min^{-1}. The Cu K_α X-ray tube of $\lambda = 1.5418$ $\mathring{A}$ and 1.6 kW power was subjected to 40 kV voltage and 40 mA current. Raman spectra were recorded using Kaiser Optical Systems Inc. (KOSI) laser Raman Spectrometer. SEM analysis and EDX spectroscopy were conducted on JEOL-JSM 7600 field emission gun-scanning electron microscopes operated in the voltage range of 0.1–30 kV. TEM images were recorded on PHILIPS-CM200 electron microscope with an operating voltage of 20–200 kV and a resolution of 2.4 $\mathring{A}$. ICP-AES studies were

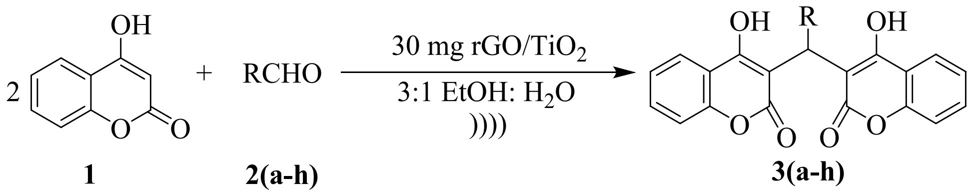

R=
a: phenyl
b: 4-methylphenyl
c: 2-methoxyphenyl
d: 3-methoxyphenyl
e: 4-methoxyphenyl
f: 4-chlorophenyl
g: 3-fluorophenyl
h: 4-fluorophenyl

Scheme 1 Synthesis of biscoumarin derivatives **3(a-h)** using rGO/TiO_2 catalyst (30 mg) in 3:1 EtOH: H_2O (4 mL) under ultrasonication

performed on a HJY Ultima-2 spectrometer (1000 W, 1.29 nebulizer flow, 2.96 nebulizer pressure, 242.795 nm wavelength). The probe sonicator used for ultrasonication was a multi-wave ultrasonic cell crusher (SJIA-250 W), equipped with a converter/transducer and a titanium oscillator of 6 mm diameter, and operated at 220 V voltage with a power of 250 W. Melting points were estimated using open capillary tubes and they are uncorrected. For recording of ^1H NMR spectra, Bruker Avance II spectrometer was used. AB SCIEX 3200 QTRAP spectrometer was used for recording of mass spectra in ESI mode. Elemental Analysis (CHN) was accomplished using EA 300 elemental analyser (Euro Vector, Italy).

2.2 Preparation of rGO

Synthesis of rGO was carried out by oxidation of graphite powder according to the modified Hummer's method [47], followed by its reduction to yield reduced graphene oxide (rGO) [48]. About 75 mL of conc. H_2SO_4 was gradually added to a mixture of the commercially acquired graphite powder (1.5 g) and $NaNO_3$ (1.5 g). After 30 min of stirring, the reaction mixture was cooled by placing it in an ice bath, followed by slow addition of $KMnO_4$ (9 g) for an hour. This caused a progressive change in the colour of the reaction mixture from black to greenish-black. The ice bath was then removed, and the mixture was stirred for two days to yield brown slurry. To this, warm distilled water (500 mL) was added, followed by slow addition of H_2O_2 (30 mL) to obtain a yellow-coloured suspension. After washing this suspension three times with 6% H_2SO_4 and 1% H_2O_2, several distilled water washings were performed until the pH was neutral. The dark-brown suspension of graphene oxide was exfoliated by mild sonication and centrifugation. During the reduction, the typical weight ratio of hydrazine to graphene oxide was approximately 7:10. The graphene oxide suspension (5 mL) was then stirred in a water bath at 95 °C for an hour with hydrazine (5 µL, 35 wt% in water) and ammonia solution (35 µL, 28 wt% in water) to obtain black-coloured rGO powder.

2.3 Preparation of rGO/TiO_2 Nanocomposite

A modified version of Men's method [49], as reported by Li et al. [50], was followed without any modifications to prepare the rGO/TiO_2 nanocomposite. The synthesized rGO powder (20 mg) and commercially obtained TiO_2 nanopowder (120 mg) were dispersed in 50 mL of a 4:1 water-ethanol solvent system, sonicated for half an hour and then subjected to hydrothermal treatment at 120 °C for 24 h. The obtained powder was dried under vacuum at 60 °C for 24 h to obtain the rGO/TiO_2 nanocomposite.

2.4 General Procedure for the Synthesis of Biscoumarin Derivatives 3(a-h)

4-hydroxycoumarin **1** (2 mmol) and aromatic aldehyde **2(a-h)** (1 mmol) were added to 3:1 ethanol:water (4 mL) in a round-bottom flask. To this, the rGO/TiO_2 nanocomposite was added (30 mg) and then subjected to ultrasonication (100 W power, 10s/5s on/off time) until completion of the reaction (monitored by TLC). The obtained precipitate was filtered and added to hot ethanol (3 mL) to dissolve the product. The catalyst was then recovered by filtration and the solvent was evaporated off under vacuum to furnish the crude product, which was purified by recrystallization from ethanol (Scheme 1).

3,3'-(phenylmethylene)bis(4-hydroxy-2 H-chromen-2-one) (3a).

Yield 98% (white solid); ***MP*** = 230–232 °C, **IR (υ_{max}/ cm^{-1})**: 2980 (OH), 1668, 1652 (C=O). **^1H NMR (300 MHz, DMSO) δ** = 7.90 (s, 1 H, Ar-**H**), 7.59 (d, *J* = 5.3 Hz, 2 H, Ar-**H**), 7.39–7.26 (m, 5 H, Ar-**H**), 7.20 (d, *J* = 5.6 Hz, 3 H, Ar-**H**), 7.15 (s, 2 H, Ar-**H**), 6.35 (s, 1 H, **CH**). **MS (ESI-ve) m/z**: 412 $(M-H)^-$. **Elemental analysis for $C_{25}H_{16}O_6$**: C, 72.81; H, 3.91; found: C, 72.76; H, 3.84.

3,3'-(p-tolylmethylene)bis(4-hydroxy-2 H-chromen-2-one) (3b).

Yield 96% (white solid); ***MP*** = 266–268 °C, **IR (υ_{max}/cm^{-1})**: 2913 (OH), 1660, 1652 (C=O). **^{1}H NMR (300 MHz, DMSO) δ** = 7.89 (d, *J* = 6.5 Hz, 2 H, Ar-**H**), 7.58 (s, 2 H, Ar-**H**), 7.35 (d, *J* = 8.4 Hz, 4 H, Ar-**H**), 7.02 (s, 4 H, Ar-**H**), 6.30 (s, 1 H, C**H**), 2.24 (s, 3 H, C**H**$_3$). **MS (ESI-ve) m/z**: 426 (M-H)$^-$. **Elemental analysis for $C_{26}H_{18}O_6$**: C, 73.23; H, 4.25; found: C, 73.14; H, 4.17.

3,3'-((2-methoxyphenyl)methylene)bis(4-hydroxy-2 H-chromen-2-one) (3c).

Yield 94% (white solid); ***MP*** = 236 °C, **IR (υ_{max}/cm^{-1})**: 2964 (OH), 1644, 1602 (C=O). **^{1}H NMR (300 MHz, DMSO) δ** = 7.91 (d, *J* = 6.3 Hz, 2 H, Ar-**H**), 7.58 (s, 2 H, Ar-**H**), 7.38–7.30 (m, 4 H, Ar-**H**), 7.16 (s, 2 H, Ar-**H**), 6.87 (dd, *J* = 12.0, 8.0 Hz, 2 H, Ar-**H**), 6.25 (s, 1 H, C**H**), 3.57 (s, 3 H, OC**H**$_3$). **MS (ESI-ve) m/z**: 442 (M-H)$^-$. **Elemental analysis for $C_{26}H_{18}O_7$**: C, 70.59; H, 4.10; found: C, 70.41; H, 4.02.

3,3'-((3-methoxyphenyl)methylene)bis(4-hydroxy-2 H-chromen-2-one) (3d).

Yield 93% (white solid); ***MP*** = 238 °C, **IR (υ_{max}/cm^{-1})**: 2980 (OH), 1659, 1651 (C=O). **^{1}H NMR (300 MHz, DMSO) δ** = 7.86 (d, *J* = 6.1 Hz, 2 H, Ar-**H**), 7.60–7.49 (m, 2 H, Ar-**H**), 7.37–7.22 (m, 4 H, Ar-**H**), 7.13 (d, *J* = 9.3 Hz, 1 H, Ar-**H**), 6.70 (d, *J* = 5.3 Hz, 2 H, Ar-**H**), 6.63 (s, 1 H, Ar-**H**), 6.28 (s, 1 H, C**H**), 3.62 (s, 3 H, OC**H**$_3$). **MS (ESI-ve) m/z**: 442 (M-H)$^-$. **Elemental analysis for $C_{26}H_{18}O_7$**: C, 70.59; H, 4.10; found: C, 70.56; H, 3.95.

3,3'-((4-methoxyphenyl)methylene)bis(4-hydroxy-2 H-chromen-2-one) (3e).

Yield 96% (white solid); ***MP*** = 242 °C, **IR (υ_{max}/cm^{-1})**: 2981 (OH), 1666, 1660 (C=O). **^{1}H NMR (300 MHz, DMSO) δ** = 7.88 (s, 2 H, Ar-**H**), 7.58 (s, 2 H, Ar-**H**), 7.33 (d, *J* = 5.7 Hz, 4 H, Ar-**H**), 7.03 (s, 2 H, Ar-**H**), 6.78 (d, *J* = 4.3 Hz, 2 H, Ar-**H**), 6.27 (s, 1 H, C**H**), 3.69 (s, 3 H, OC**H**$_3$). **MS (ESI-ve) m/z**: 442 (M-H). **Elemental analysis for $C_{26}H_{18}O_7$**: C, 70.59; H, 4.10; found: C, 70.54; H, 3.98.

3,3'-((4-chlorophenyl)methylene)bis(4-hydroxy-2 H-chromen-2-one) (3f).

Yield 97% (white solid); ***MP*** = 256–258 °C, **IR (υ_{max}/cm^{-1})**: 2980 (OH), 1661, 1603 (C=O). **^{1}H NMR (300 MHz, DMSO) δ** = 7.89 (s, 2 H, Ar-**H**), 7.58 (s, 2 H, Ar-**H**), 7.33 (s, 3 H, Ar-**H**), 7.26 (d, *J* = 6.9 Hz, 3 H, Ar-**H**), 7.17 (s, 2 H, Ar-**H**), 6.31 (s, 1 H, C**H**). **MS (ESI-ve) m/z**: 446 (M)$^+$. **Elemental analysis for $C_{25}H_{15}ClO_6$**: C, 67.20; H, 3.38; found: C, 67.08; H, 3.25.

3,3'-((3-fluorophenyl)methylene)bis(4-hydroxy-2 H-chromen-2-one) (3 g).

Yield 97% (white solid); ***MP*** = 283 °C, **IR (υ_{max}/cm^{-1})**: 3065 (OH), 1667, 1606 (C=O). **^{1}H NMR (300 MHz, DMSO) δ** = 7.88 (d, *J* = 6.8 Hz, 2 H, Ar-**H**), 7.57 (s, 2 H, Ar-**H**), 7.34 (d, *J* = 8.0 Hz, 5 H, Ar-**H**), 6.93 (d, *J* = 20.0 Hz, 3 H, Ar-**H**), 6.33 (s, 1 H, C**H**). **MS (ESI-ve) m/z**: 430 (M-H)$^-$. **Elemental analysis for $C_{25}H_{15}FO_6$**: C, 69.77; H, 3.51; found: C, 69.67; H, 3.42.

3,3'-((4-fluorophenyl)methylene)bis(4-hydroxy-2 H-chromen-2-one) (3 h).

Yield 95% (white solid); ***MP*** = 213–215 °C, **IR (υ_{max}/cm^{-1})**: 2980 (OH), 1667, 1604 (C=O). **^{1}H NMR (300 MHz, DMSO) δ** = 7.89 (d, *J* = 6.2 Hz, 2 H, Ar-**H**), 7.58 (s, 2 H, Ar-**H**), 7.35 (d, *J* = 6.0 Hz, 4 H, Ar-**H**), 7.16 (s, 2 H, Ar-**H**), 7.03 (s, 2 H, Ar-**H**), 6.31 (s, 1 H, C**H**). **MS (ESI-ve) m/z**: 430 (M-H)$^-$. **Elemental analysis for $C_{25}H_{15}FO_6$**: C, 69.77; H, 3.51; found: C, 69.62; H, 3.40.

2.5 General Procedure for the Synthesis of Bislawsone Derivatives 5(a-h)

2-hydroxy-4-naphthoquinone **4** (2 mmol) and aromatic aldehyde **2(a-h)** (1 mmol) were placed in a round-bottom flask containing 3:1 ethanol:water (4 mL). The rGO/TiO$_2$ catalyst (30 mg) was then added, and the reaction mixture was subjected to ultrasonication (100 W power, 10s/5s on/off time). Upon completion of the reaction, as indicated by TLC, the reaction mixture was filtered, and the product obtained from the solid residue was dissolved in hot ethanol (3 mL). The catalyst was then filtered, and the crude mass obtained by vacuum evaporation of the solvent was recrystallized with ethanol to yield the purified product (Scheme 2).

3,3'-(phenylmethylene)bis(2-hydroxynaphthalene-1,4-dione) (5a).

Yield 97% (Yellow solid); ***MP*** = 202–204 °C, **IR (υ_{max}/cm^{-1})**: 3327 (OH), 1658, 1643 (C=O). **^{1}H NMR (300 MHz, CDCl$_3$) δ** = 8.11 (d, *J* = 4.7 Hz, 7 H, Ar-**H**), 7.74 (dd, *J* = 11.5, 3.9 Hz, 6 H, Ar-**H**), 6.27 (s, 1 H, C**H**). **MS (ESI-ve) m/z**: 436 (M-H)$^-$. **Elemental analysis for $C_{27}H_{16}O_6$**: C, 74.31; H, 3.70; found: C, 74.25; H, 3.62.

3,3'-(p-tolylmethylene)bis(2-hydroxynaphthalene-1,4-dione) (5b).

Yield 94% (Yellow solid); ***MP*** = 174–176 °C, **IR (υ_{max}/cm^{-1})**: 3355 (OH), 1620, 1608 (C=O). **^{1}H NMR (300 MHz, DMSO) δ** = 7.99–7.90 (m, 4 H, Ar-**H**), 7.78 (s, 4 H, Ar-**H**), 7.03 (d, *J* = 27.6 Hz, 4 H, Ar-**H**), 5.97 (s, 1 H, C**H**), 2.23 (s, 3 H, C**H**$_3$). **MS (ESI + ve) m/z**: 450 (M + H)$^+$. **Elemental analysis for $C_{28}H_{18}O_6$**: C, 74.66; H, 4.03; found: C, 74.51; H, 3.94.

3,3'-((2-methoxyphenyl)methylene)bis(2-hydroxynaphthalene-1,4-dione) (5c).

Yield 95% (Yellow solid); ***MP*** = 212–214 °C, **IR (υ_{max}/cm^{-1})**: 3293 (OH), 1659, 1634 (C=O). **^{1}H NMR (300 MHz, DMSO) δ** = 7.93 (d, *J* = 19.2 Hz, 4 H, Ar-**H**), 7.79 (s, 4 H, Ar-**H**), 7.09 (d, *J* = 20.9 Hz, 2 H, Ar-**H**), 6.82 (d, *J* = 31.1 Hz, 2 H, Ar-**H**), 6.04 (s, 1 H, C**H**), 3.65 (s, 3 H, OC**H**$_3$). **MS (ESI) m/z**: 466 (M)$^+$. **Elemental analysis for $C_{28}H_{18}O_7$**: C, 72.10; H, 3.89; found: C, 72.03; H, 3.72.

Scheme 2 Synthesis of bislawsone derivatives **5(a-h)** using rGO/TiO_2 catalyst (30 mg) in 3:1 EtOH: H_2O (4 mL) under ultrasonication

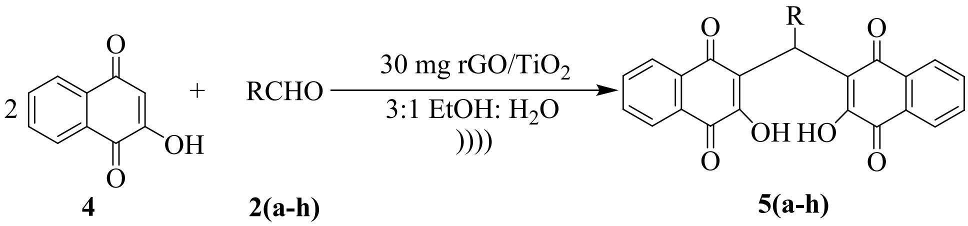

R=

a: phenyl	e: 4-methoxyphenyl
b: 4-methylphenyl	f: 4-chlorophenyl
c: 2-methoxyphenyl	g: 3-fluorophenyl
d: 3-methoxyphenyl	h: 4-fluorophenyl

3,3'-((3-methoxyphenyl)methylene)bis(2-hydroxynaphthalene-1,4-dione) (5d).

Yield 94% (Yellow solid); ***MP*** = 190–192 °C, **IR (υ_{max}/cm^{-1})**: 3061 (OH), 1613, 1593 (C=O). **^{1}H NMR (300 MHz, $CDCl_3$) δ** = 8.10 (s, 4 H, Ar-**H**), 7.79–7.66 (m, 4 H, Ar-**H**), 7.23 (s, 1 H, Ar-**H**), 6.82 (dd, *J* = 18.3, 10.6 Hz, 3 H, Ar-**H**), 6.24 (s, 1 H, **CH**), 3.76 (s, 3 H, OCH_3). **MS (ESI-ve) m/z**: 466 (M-H)$^-$. **Elemental analysis for $C_{28}H_{18}O_7$**: C, 72.10; H, 3.89; found: C, 72.01; H, 3.69.

3,3'-((4-methoxyphenyl)methylene)bis(2-hydroxynaphthalene-1,4-dione) (5e).

Yield 93% (Yellow solid); ***MP*** = 220–222 °C, **IR (υ_{max}/cm^{-1})**: 3394 (OH), 1665, 1634 (C=O). **^{1}H NMR (300 MHz, $CDCl_3$) δ** = 8.11 (d, *J* = 6.6 Hz, 4 H, Ar-**H**), 7.72 (dd, *J* = 15.3, 7.7 Hz, 4 H, Ar-**H**), 7.22 (d, *J* = 8.1 Hz, 2 H, Ar-**H**), 6.84 (d, *J* = 6.4 Hz, 2 H, Ar-**H**), 6.18 (s, 1 H, **CH**), 3.79 (s, 3 H, **OCH_3**). **MS (ESI-ve) m/z**: 466 (M-H)$^-$. **Elemental analysis for $C_{28}H_{18}O_7$**: C, 72.10; H, 3.89; found: C, 72.04; H, 3.74.

3,3'-((4-chlorophenyl)methylene)bis(2-hydroxynaphthalene-1,4-dione) (5f).

Yield 96% (Yellow solid); ***MP*** = 188–190 °C, **IR (υ_{max}/cm^{-1})**: 3155 (OH), 1639, 1631 (C=O). **^{1}H NMR (300 MHz, $CDCl_3$) δ** = 8.09 (s, 5 H, Ar-**H**), 7.75 (s, 2 H, Ar-**H**), 7.24 (s, 5 H, Ar-**H**), 6.17 (s, 1 H, **CH**). **MS (ESI + ve) m/z**: 470 (M + H)$^+$. **Elemental analysis for $C_{27}H_{15}ClO_6$**: C, 68.87; H, 3.21; O, 20.39; found: C, 68.75; H, 3.14; O, 20.24.

3,3'-((3-fluorophenyl)methylene)bis(2-hydroxynaphthalene-1,4-dione) (5 g).

Yield 97% (Yellow solid); ***MP*** = 213–215 °C, **IR (υ_{max}/cm^{-1})**: 3422 (OH), 1654, 1640 ((C=O). **^{1}H NMR (300 MHz, $CDCl_3$) δ** = 8.11 (s, 4 H, Ar-**H**), 7.79–7.68 (m, 4 H, Ar-**H**), 7.25 (s, 1 H, Ar-**H**), 7.08 (d, *J* = 4.9 Hz, 1 H, Ar-**H**), 7.02–6.90 (m, 2 H, Ar-**H**), 6.23 (s, 1 H, **CH**). **MS (ESI + ve) m/z**: 454 (M + H)$^+$. **Elemental analysis for $C_{27}H_{15}FO_6$**: C, 68.82; H, 3.19; found: C, 68.75; H, 3.11.

3,3'-((4-fluorophenyl)methylene)bis(2-hydroxynaphthalene-1,4-dione) (5 h).

Yield 96% (Yellow solid); ***MP*** = 193–195 °C, **IR (υ_{max}/cm^{-1})**: 3333 (OH), 1669, 1640 (C=O). **^{1}H NMR (300 MHz, $CDCl_3$) δ** = 8.10 (s, 5 H, Ar-**H**), 7.81–7.62 (m, 5 H, Ar-**H**), 6.98 (s, 2 H, Ar-**H**), 6.18 (s, 1 H, **CH**). **MS (ESI + ve) m/z**: 454 (M + H)$^+$. **Elemental analysis for $C_{27}H_{15}FO_6$**: C, 71.37; H, 3.33; found: C, 71.21; H, 3.28.

3 Results and Discussion

3.1 Characterization of rGO and rGO/TiO_2 Nanocomposite

3.1.1 Fourier Transform Infrared Spectroscopy (FTIR)

FTIR spectroscopic analysis of rGO (Fig. 1a) and the rGO/TiO_2 nanocomposite (Fig. 1b) was performed for the detection of functional groups and characterization of the

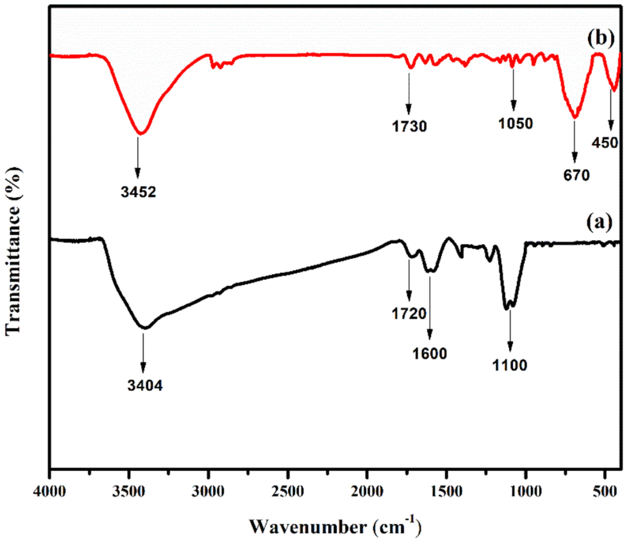

Fig. 1 FTIR spectra of **a** rGO and **b** rGO/TiO_2 nanocomposite using a powder sample

covalent bonding information [51]. The broad peaks at around 3400 cm^{-1} are attributed to the stretching vibrations of the surface hydroxyl groups. The peaks at around 1700 cm^{-1} correspond to the carbonyl functional group, whereas the peaks at 1100 cm^{-1} in Fig. 1a and 1050 cm^{-1} in Fig. 1b are accredited to C–O stretching vibrations. In Fig. 1a, the peak observed at around 1600 cm^{-1} corresponds to the skeletal vibrations of the rGO sheet [52]. The presence of oxygen-containing functional groups in Fig. 1b suggests partial reduction of graphene, thereby facilitating the interaction of TiO_2 with these groups [53]. The characteristic peaks of Ti–O–Ti vibrations are observed at 670 cm^{-1} and 450 cm^{-1} in the spectrum of the nanocomposite (Fig. 1b).

3.1.2 X-Ray Diffraction (XRD)

X-Ray Diffraction Studies of rGO (Fig. 2a) and rGO/TiO_2 nanocomposite (Fig. 2b) were carried out to determine the crystallographic structure. The peaks at $2\theta = 24.4^\circ$ and 44° corresponding to the (002) and (100) planes, respectively, observed in Fig. 2a, are characteristic of a typical graphitic structure [54]. The diffraction pattern of the nanocomposite (Fig. 2b) suggests the formation of anatase TiO_2 nanoparticles (JCPDS 21-1272). The peaks at $2\theta = 25.3^\circ$, 37.9°, 48°, 54.3°, and 62.9° can be indexed to the (101), (004), (200), (105), and (204) reflection planes, respectively. The low intensity of these peaks is accredited to the use of ultrasonication during the synthesis of the nanocomposite [55]. Moreover, shielding of the (002) peak of rGO at 24.4° by the (101) peak of TiO_2 at 25.3° in the nanocomposite is a commonly observed phenomenon [56].

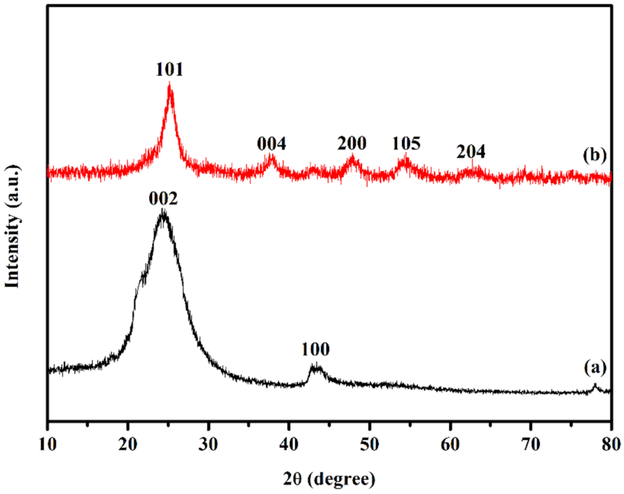

Fig. 2 X-ray diffraction pattern of **a** rGO and **b** rGO/TiO_2 nanocomposite using a powder sample from 10° to 80° 2θ range at scanning speed of 5 min^{-1}

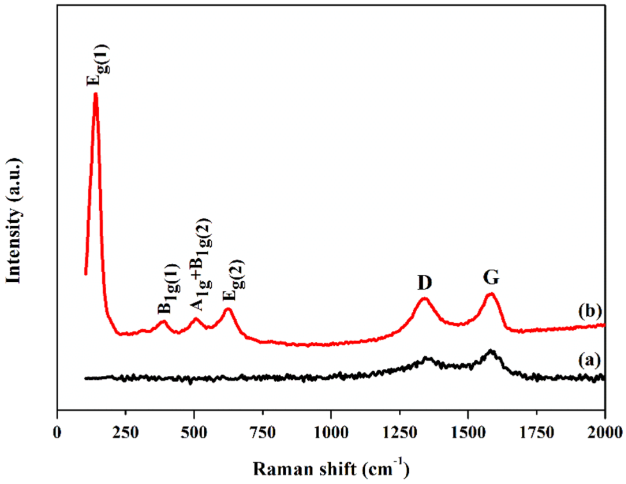

Fig. 3 Raman spectra of **a** rGO and **b** rGO/TiO_2 nanocomposite using a powder sample

3.1.3 Raman Spectroscopy

Raman Spectroscopy is one of the most powerful non-destructive tools used to characterize graphitic materials. Figure 3b shows the phonon bands of anatase TiO_2 at 144 cm^{-1}, 396 cm^{-1}, 512 cm^{-1} and 631 cm^{-1}, corresponding to the $E_{g(1)}$, B_{1g}, $A_{1g} + B_{1g}$, and $E_{g(2)}$ transitions, respectively [57]. Furthermore, the spectra exhibit two characteristic bands: the D-band (sp^3 defects) and the G-band (in-plane vibrations of sp^2 atoms) [58]. In rGO (Fig. 3a), these bands were obtained at 1341 cm^{-1} and 1580 cm^{-1}, while in the nanocomposite (Fig. 3b), they were at 1353 cm^{-1} and 1589 cm^{-1}, respectively. The red shift observed in these bands can be attributed to the presence of hydroxyl groups on the surface of the nanocomposite. Correspondingly, the I_D/I_G ratio increased from 0.77 in rGO to 0.94 in rGO/TiO_2 as structural defects in two-dimensional graphitic sheets increased with the incorporation of TiO_2 [59, 60].

3.1.4 Morphology

The morphological features of rGO and rGO/TiO_2 nanocomposite were investigated using SEM, TEM and EDX characterization techniques. The SEM image of rGO (Fig. 4a) shows a two-dimensional layered structure of graphene sheets with curved edges, while that of the nanocomposite (Fig. 4b) depicts the rGO sheets as well-decorated and embedded with TiO_2 nanoparticles. Further, TEM analysis was carried out for detailed structural examination. Figure 5a portrays the smooth and somewhat wrinkled graphene layers of rGO, and Fig. 5b illustrates the TiO_2 nanoparticles anchored and aggregated over the rGO sheets. EDX spectroscopy (Fig. 6) revealed

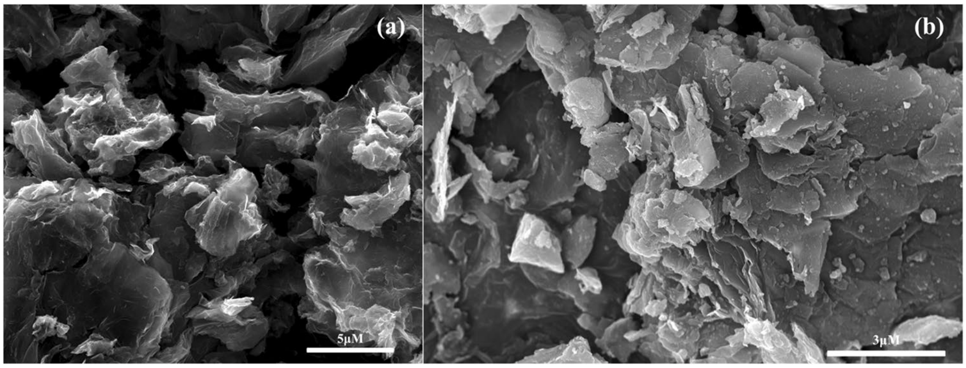

Fig. 4 SEM images of **a** rGO and **b** rGO/TiO_2 nanocomposite using a small portion of the powder dispersed in ethanol, transferred to the adhesive carbon tape, and air-drying

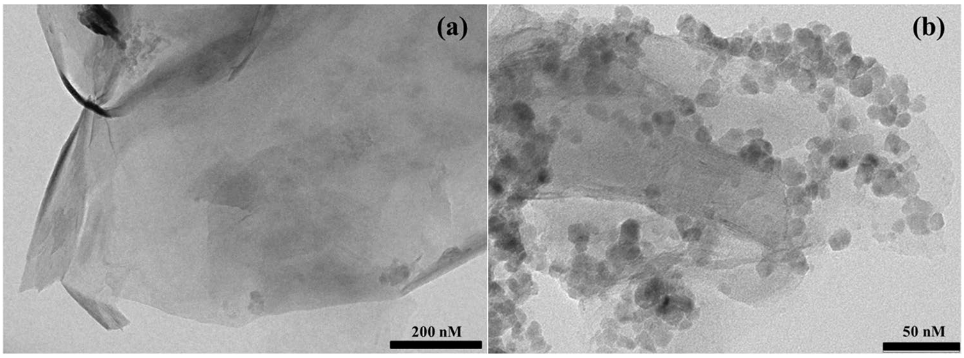

Fig. 5 TEM images of **a** rGO and **b** rGO/TiO_2 nanocomposite by dispersing a small portion in ethanol and transferring it to the copper grid and air-drying

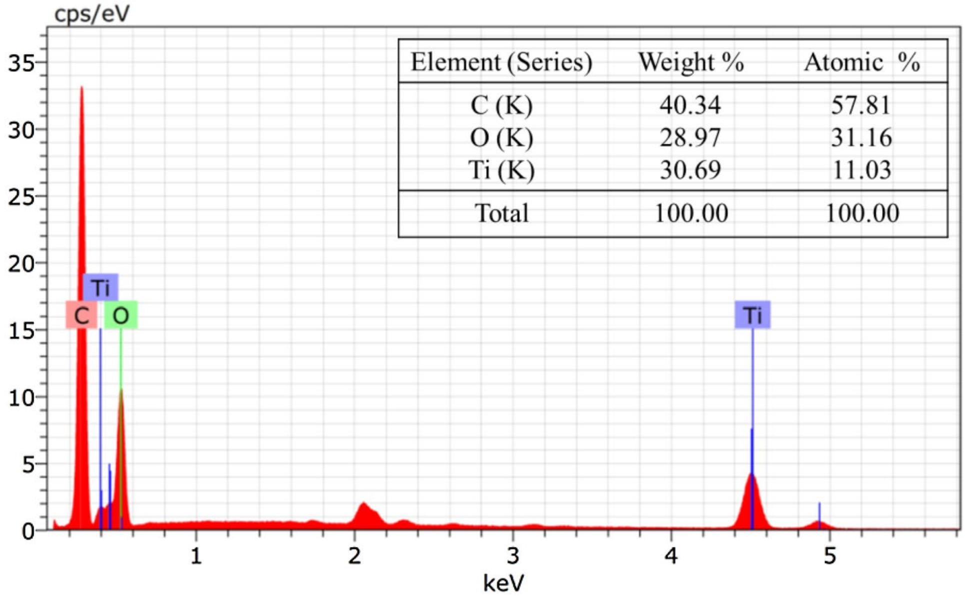

Element (Series)	Weight %	Atomic %
C (K)	40.34	57.81
O (K)	28.97	31.16
Ti (K)	30.69	11.03
Total	100.00	100.00

Fig. 6 EDX spectrum of rGO/TiO_2 nanocomposite using a small portion of the powder dispersed in ethanol and transferring to the adhesive carbon tape and air-drying

the elemental composition of the nanocomposite, with 57.81% of C, 31.16% of O and 11.03% of Ti. Other than the detected elements, no other impurities were detected inferring that the synthesized nanocomposite is in high purity.

3.2 Catalytic Performance of rGO/TiO_2 Nanocomposite

To develop an efficient synthetic protocol, various reaction parameters, such as the amount of catalyst, solvent and solvent systems, and temperature were optimized by

Table 1 Optimization of reaction parameters for the synthesis of **3a**

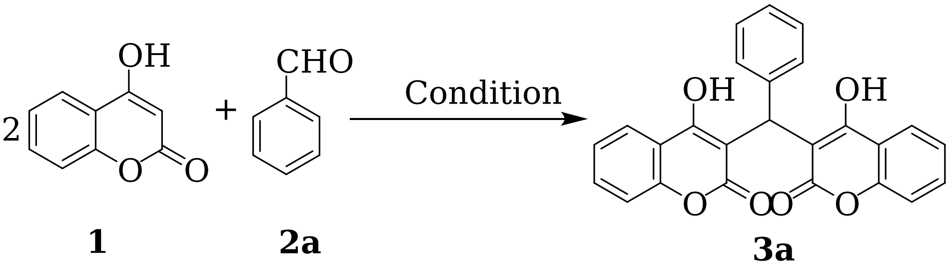

Entry	Catalyst	Solvent	Condition[a]	% yield[c]
1	No catalyst	Ethanol	US probe	20
2	rGO (30 mg)	Ethanol	US probe	26
3	Bulk TiO_2 (30 mg)	Ethanol	US probe	25
4	Commercial TiO_2 NPs (30 mg)	Ethanol	US probe	48
5	rGO/TiO_2 (30 mg)	Ethanol	US probe	77
6	rGO/TiO_2 (20 mg)	Ethanol	US probe	62
7	rGO/TiO_2 (40 mg)	Ethanol	US probe	77
8	rGO/TiO_2 (30 mg)	Methanol	US probe	72
9	rGO/TiO_2 (30 mg)	Water	US probe	47
10	rGO/TiO_2 (30 mg)	Acetonitrile	US probe	45
11	rGO/TiO_2 (30 mg)	Dichloromethane	US probe	40
12	rGO/TiO_2 (30 mg)	Toluene	US probe	38
13	**rGO/TiO_2 (30 mg)**	**Ethanol:Water (3:1)**	**US probe**	**98**
14	rGO/TiO_2 (30 mg)	Ethanol:Water (2:1)	US probe	76
15	rGO/TiO_2 (30 mg)	Ethanol:Water (1:1)	US probe	70
16	rGO/TiO_2 (30 mg)	Ethanol:Water (1:2)	US probe	58
17	rGO/TiO_2 (30 mg)	Ethanol:Water (1:3)	US probe	50
18	rGO/TiO_2 (30 mg)	Ethanol:Water (3:1)	25 °C[b]	35
19	rGO/TiO_2 (30 mg)	Ethanol:Water (3:1)	50 °C	55
20	rGO/TiO_2 (30 mg)	Ethanol:Water (3:1)	75 °C	64
21	rGO/TiO_2 (30 mg)	Ethanol:Water (3:1)	US bath	56

Bold indicates best optimum condition for the present synthetic strategy

[a] All reactions were carried out for 5 min except for

[b] Entry 18 which was carried out for 30 min

[c] Isolated yield

considering the reaction between 4-hydroxycoumarin and benzaldehyde as a module (Table 1). Foremost, the use of the catalyst was substantiated by carrying out the reaction in its absence. The reaction did not proceed well, and about 20% of the product was obtained (Table 1, entry 1). Moreover, using the synthesized rGO powder as a catalyst resulted in a low yield (Table 1, entry 2). The use of commercially procured bulk and nano TiO_2 also resulted in poor yields (Table 1, entries 3 and 4). The rGO/TiO_2 nanocomposite was then utilized as a heterogeneous catalyst, resulting in a somewhat acceptable product yield of 77% (Table 1, entry 5). The effect of catalyst loading was then investigated by varying the amount of nanocomposite added from 20 mg to 40 mg (Table 1, entries 6 and 7). It was observed that 30 mg of the catalyst was optimal, and increasing or decreasing the amount of catalyst yielded substandard results. Thus, 30 mg of rGO/TiO_2 was used for further investigation. To study the effect of solvents, protic solvents such as ethanol, methanol, and water and aprotic solvents such as acetonitrile, dichloromethane, and toluene were used. The highest yield was observed for ethanol (Table 1, entry 5), followed by methanol and water (Table 1, entries 8 and 9, respectively); aprotic solvents resulted in lower yields (Table 1, entries 10–12). Interestingly, the water-ethanol solvent system granted excellent results (Table 1, entries 13–17). Upon careful examination, it was found that 3:1 ethanol:water afforded

Table 2 Synthesis of biscoumarin derivatives **3(a-h)** using rGO/TiO$_2$ nanocomposite under optimized reaction conditions

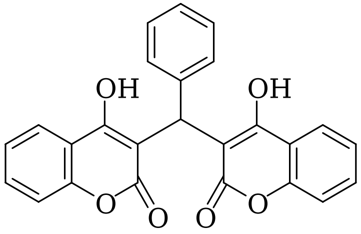

3a (5 min, 98%^{a})

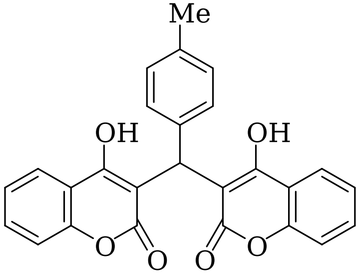

3b (5 min, 96%^{a})

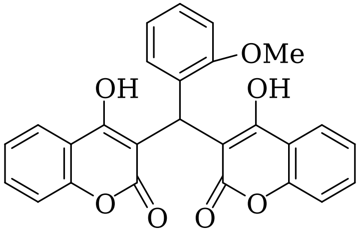

3c (6 min, 94%^{a})

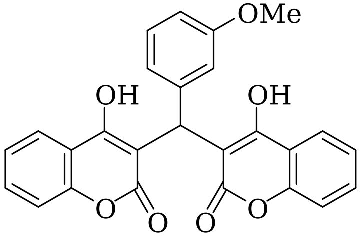

3d (6 min, 93%^{a})

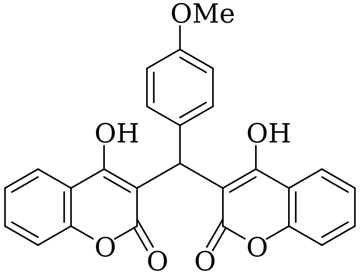

3e (5.5 min, 96%^{a})

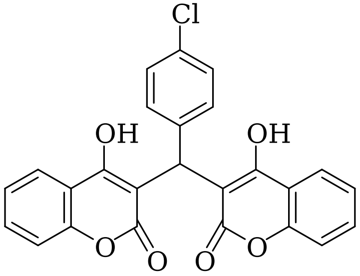

3f (5 min, 97%^{a})

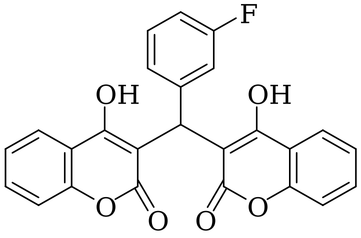

3 g (7.5 min, 97%^{a})

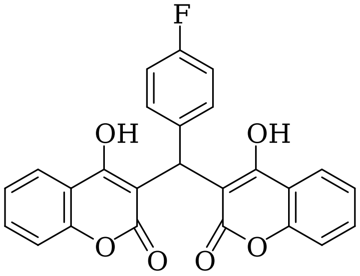

3 h (7 min, 95%^{a})

Reaction conditions: 4-hydroxycoumarin (2 mmol), aldehyde (1 mmol) and catalyst (30 mg) under ultrasonication at room temperature

[a] Isolated yield

Table 3 Synthesis of bislawsone derivatives **5(a-h)** using rGO/TiO_2 nanocomposite under optimized reaction conditions

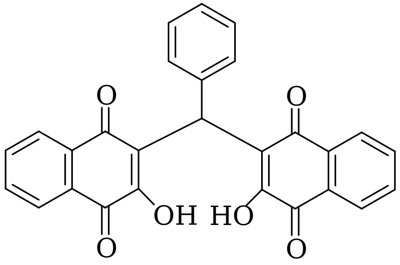

5a (5 min, 97%[a])

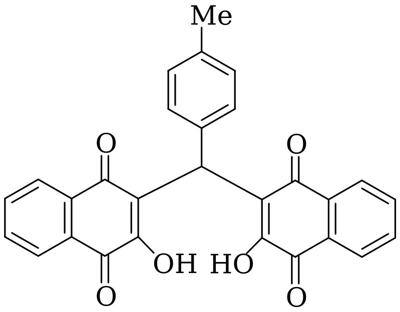

5b (5.5 min, 94%[a])

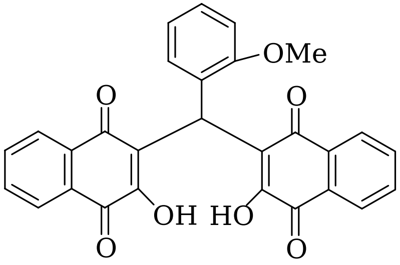

5c (6 min, 95%[a])

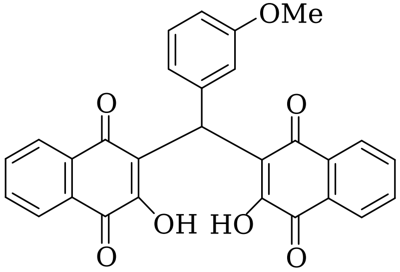

5d (5 min, 94%[a])

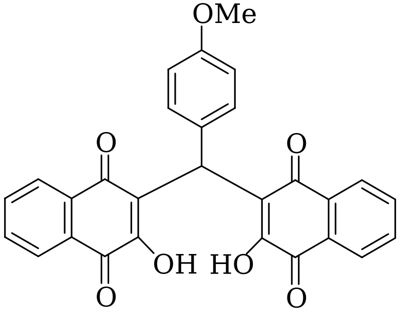

5e (6.5 min, 93%[a])

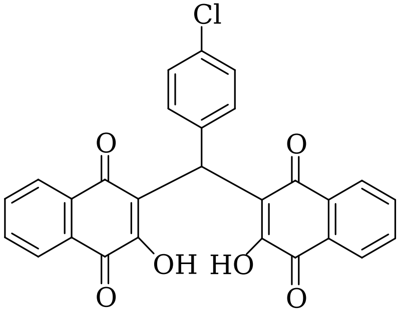

5f (6 min, 96%[a])

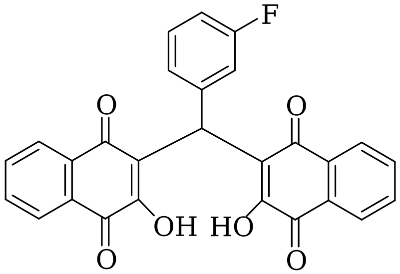

5 g (8 min, 97%[a])

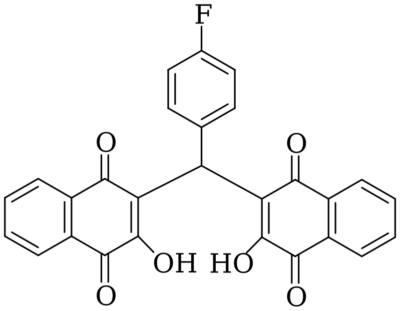

5 h (8 min, 96%[a])

Reaction conditions: 2-hydroxy-4-naphthoquinone (2 mmol), aldehyde (1 mmol) and catalyst (30 mg) under ultrasonication at room temperature

[a] Isolated yield

Table 4 Comparative study of rGO/TiO_2 nanocomposite for the synthesis of biscoumarin and bislawsone derivatives

Entry	Product	Catalyst	Condition	Yield (%)	Refs.
1	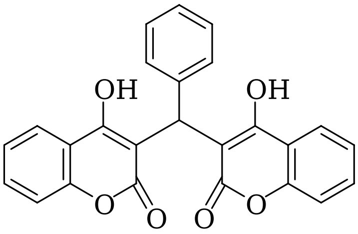	TiO_2/KSF (20 mg)	Neat, 100 °C, 10 min	98	[61]
2		$RuCl_3$ (5 mol%)	Water, 80 °C, 25 min	84	[34]
3		DBSA (25 mol%)	1:1 EtOH:H_2O, MW, 12 min	95	[62]
4		[bmim]BF_4 (4 eq.)	Neat, 60–70 °C, 2 h	84	[36]
5		$BiVO_4$ (30 mg)	Water, 80 °C, 25 min	98	[63]
6		TBAB (10 mol%)	Water, reflux, 25 min	92	[32]
7		Nano TiO_2 (5 mol%)	Water, reflux, 8 min	90	[64]
8		Graphene oxide (5 mg)	Water, reflux, 25 min	90	[65]
9		**rGO/TiO_2 (30 mg)**	**3:1 EtOH:H_2O, US, 5 min**	**98**	**This work**
10	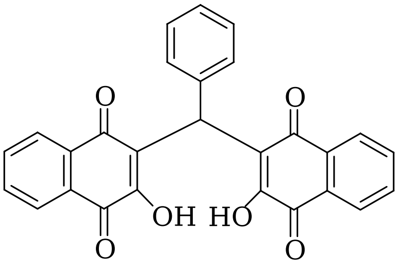	Lipase (30 mg)	Ethanol, 60 °C, 2 h	88	[40]
11		Et_3N (1 eq.)	Ethanol, 25 °C, 5 min	75	[66]
12		Humic acid (10 mg)	Neat, 100 °C, 15 min	96	[39]
13		CSA (20 mol%)	1:1 EtOH:H_2O, 27 °C, 2 h	94	[38]
14		LiCl (1 eq.)	Water, 25 °C, 12 h	83	[41]
15		β-alanine (15 mg)	AcOH, Ar atm, reflux, 5 h	83	[28]
16		Sulfamic acid (20 mol%)	1:1 EtOH:H_2O, 25 °C, 16 h	92	[43]
17		DMAP (20 mol%)	EtOH, MW, reflux, 15 min	96	[37]
18		**rGO/TiO_2 (30 mg)**	**3:1 EtOH:H_2O, US, 5 min**	**97**	**This work**

Bold indicates best optimum condition for the present synthetic strategy

an exceptional product yield of 98% (Table 1, entry 13). Furthermore, the reaction was performed under reflux conditions as well as in an ultrasonic bath to authenticate the use of probe ultrasonication. Insufficient yields were observed under thermal conditions (Table 1, entries 18–20), and the ultrasonic bath resulted in a slightly better but inadequate yield (Table 1, entry 21). Thus, to demonstrate its generality, the optimized protocol was employed to synthesize eight biscoumarin derivatives **3(a-h)** by varying the aromatic aldehyde. Table 2 lists the reaction times and the isolated yields of the derivatives. It was observed that the nature of the aldehyde (electron-rich or electron-poor) did not affect the general outcome of the reaction, and all products were obtained in high yields in a short amount of time.

Encouraged by these phenomenal observations, the scope of this novel methodology was assessed by replacing 4-hydroxycoumarin with 2-hydroxy-1,4-naphthoquinone and synthesizing bislawsone derivatives. A total of eight products **5(a-h)** were obtained with exceptional yields using a diverse array of aldehydes, as delineated in Table 3.

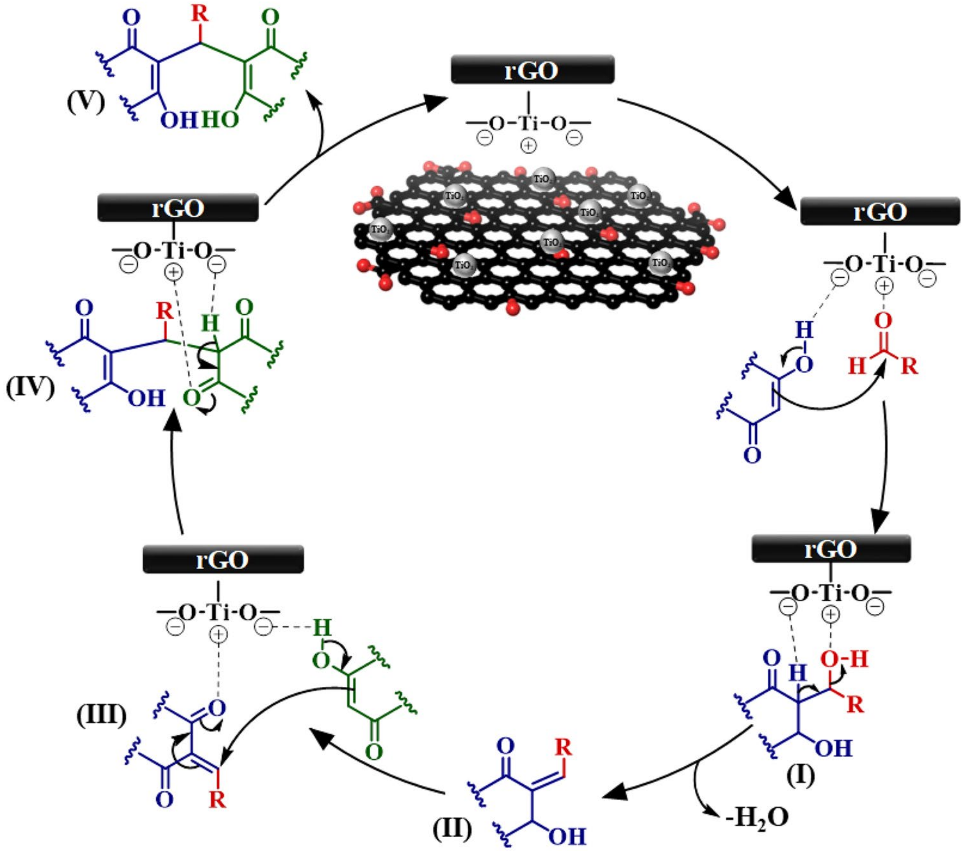

Fig. 7 Plausible mechanism for biscoumarin and bislawsone synthesis in the presence of rGO/TiO_2 nanocomposite

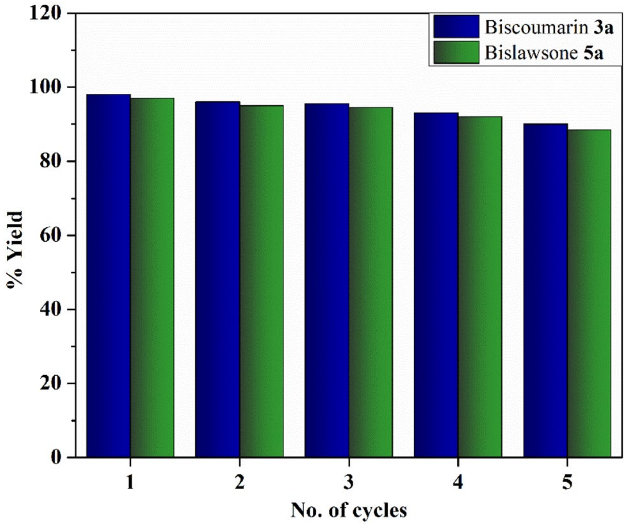

Fig. 8 Recyclability of the rGO/TiO_2 catalyst. Reaction conditions: 4-hydroxycoumarin/2-hydroxy-4-naphthoquinone (2 mmol), benzaldehyde (1 mmol) and catalyst (30 mg) under ultrasonication at room temperature

3.3 Comparative Study

To establish the merits of the rGO/TiO_2 nanocomposite as a heterogeneous catalyst, a study was conducted to compare the efficiency of the current protocol with those previously reported in the literature, as depicted in Table 4. The reaction parameters considered for comparison were the nature and amount of catalyst used, nature of the solvent used, reaction temperature and time, product yields, and utilization of non-conventional alternatives such as ionic liquids, microwave irradiation, or ultrasonication to spike the reaction rate. It is evident that despite the observed versatility, the reported protocols suffer from numerous drawbacks, such as high reaction temperature and time, inadequate product yield, harsh reaction conditions, and the requirement of an inert atmosphere. The present work supersedes all these difficulties and thus validates the efficacy of this novel methodology.

3.4 Plausible Mechanism

Figure 7 outlines a plausible mechanism for rGO/TiO_2 catalyzed biscoumarin and bislawsone synthesis. Initially, the carbonyl group of the aldehyde is activated by Ti^{4+}, facilitating nucleophilic attack of the carbon atom of 4-hydroxycoumarin/2-hydroxy-4-naphthoquinone on the aldehyde to form intermediate **I**. Subsequently, a water molecule is lost to yield enol **II**, which tautomerizes to its keto form **III**. Ti^{4+} then activates intermediate **III**, followed by a nucleophilic attack from another 4-hydroxycoumarin/2-hydroxy-4-naphthoquinone molecule, forming intermediate **IV**. Finally, another keto-enol tautomerization leads to the formation of the desired product **V**, regenerating the catalyst.

3.5 Recyclability Study

The ability to catalyze multiple reaction cycles without significantly affecting the reaction outcome is one of the fundamentals of catalysis. Model reactions of 4-hydroxycoumarin and benzaldehyde for the synthesis of biscoumarin **3a** and 2-hydroxy-4-naphthoquinone and benzaldehyde for the synthesis of bislawsone **5a** were employed to ascertain the reusability of the catalyst. On completing the reaction, as mentioned in Schemes 1 and 2, the catalyst was isolated via filtration, washed several times with hot ethanol, dried in an oven, and then reused. As illustrated in Fig. 8, the efficiency of the rGO/TiO_2 nanocomposite remained unaltered for up to five catalytic runs for both biscoumarin **3a** and bislawsone **5a**. Leaching of TiO_2 nanoparticles into the reaction mixture was also analyzed with ICP-AES analysis. For this purpose, blank rGO/TiO_2 nanocomposite in 3:1 EtOH:H_2O was taken and the sample was ultrasonicated for 5 min. The solvent was analysed using ICP-AES and it was found that Ti concentration in the solution was less than the detection limit. Similar results were obtained when the completed reaction mixture was filtered and the solvent was analysed. Both findings indicate that the TiO_2 nanoparticles did not leach into the solution during the catalytic cycles and thus, remained intact on the rGO support. The eventual decline observed in the efficacy of the catalyst may be accredited to agglomeration of the nanomaterial or minor inadequacies in the recovery process.

4 Conclusion

In conclusion, a novel ultrasound-assisted procedure was developed for the efficient synthesis of biscoumarin and bislawsone derivatives catalyzed by rGO/TiO_2 nanocomposite. The catalyst was characterized by FTIR, XRD, Raman, SEM, TEM and EDX techniques. FTIR, XRD, and Raman analyses were used to verify the structural features. SEM and TEM imaging were used to determine the morphological attributes, and EDX spectroscopy was used to examine the elemental composition. The reaction parameters were optimized, and several biscoumarin and bislawsone derivatives were synthesized. The sustainable nature of the current synthetic protocol pays heed to the postulates of Green Chemistry i.e. ambient reaction temperature, short reaction time, use of green solvents, extraordinary product yield, and reusability of the catalyst for five cycles and hence, offers an environmentally attractive approach to conventional synthesis.

Supplementary Information The online version contains supplementary material available at https://doi.org/10.1007/s42250-023-00587-6.

Acknowledgements We are thankful to Microanalytical Laboratory, University of Mumbai for providing characterization facilities. Authors also acknowledge SAIF (IITB), Mumbai.

Author Contributions SS and YY contributed to the design and implementation of the research, to the analysis of the results and writing of the manuscript. SB and JS contributed to the interpretation of the results to the writing and review of the manuscript.

Funding Not applicable.

Declarations

Conflict of Interest The authors declare that there are no financial or commercial conflicts of interest that could have appeared to influence the work stated in this paper.

Ethical Approval Not applicable.

References

1. Dömling A (2005) The discovery of new isocyanide-based multicomponent reactions. In: Zhu J, Bienaymé H (eds) Multicomponent reactions. Wiley, New York, pp 76–94. https://doi.org/10.1002/3527605118.ch3
2. Abranches PA, da Paiva S, de Fátima WF et al (2018) Calix[*n*] arene-Catalyzed three-component Povarov reaction: microwave-assisted synthesis of Julolidines and mechanistic insights. J Org Chem 83(4):1761–1771. https://doi.org/10.1021/acs.joc.7b02532
3. Neto BAD, Rocha RO, Rodrigues MO (2021) Catalytic approaches to multicomponent reactions: a critical review and perspectives on the roles of catalysis. Molecules 27(1):132–159. https://doi.org/10.3390/molecules27010132
4. Kerru N, Bhaskaruni SVHS, Gummidi L et al (2019) Recent advances in heterogeneous catalysts for the synthesis of imidazole derivatives. Synth Commun 49(19):2437–2459. https://doi.org/10.1080/00397911.2019.1639755
5. Climent MJ, Corma A, Iborra S (2012) Homogeneous and heterogeneous catalysts for multicomponent reactions. RSC Adv 2(1):16–58. https://doi.org/10.1039/C1RA00807B
6. Behravesh S, Fareghi-Alamdari R, Badri R (2018) Sulfonated reduced graphene oxide (rGO-SO_3H): as an efficient nanocatalyst for one-pot synthesis of 2-amino-3-cyano-7-hydroxy-4H-chromenes derivatives in water. Polycycl Aromat Compd 38(1):51–65. https://doi.org/10.1080/10406638.2016.1149080

7. Wang S, Wang Z, Zha Z (2009) Metal nanoparticles or metal oxide nanoparticles, an efficient and promising family of novel heterogeneous catalysts in organic synthesis. Dalton Trans 43:9363–9373. https://doi.org/10.1039/B913539A
8. Sankar M, He Q, Engel R et al (2020) Role of the support in gold-containing nanoparticles as heterogeneous catalysts. Chem Rev 120(8):3890–3938. https://doi.org/10.1021/acs.chemrev.9b00662
9. Demirkan B, Bozkurt S, Şavk A et al (2019) Composites of bimetallic platinum-cobalt alloy nanoparticles and reduced graphene oxide for electrochemical determination of ascorbic acid, dopamine, and uric acid. Sci Rep 9:12258–12264. https://doi.org/10.1038/s41598-019-48802-0
10. Leary R, Westwood A (2011) Carbonaceous nanomaterials for the enhancement of TiO_2 photocatalysis. Carbon 49(3):741–772. https://doi.org/10.1016/j.carbon.2010.10.010
11. Morales-Torres S, Pastrana-Martínez LM, Figueiredo JL, Faria JL et al (2012) Design of graphene-based TiO2 photocatalysts—a review. Environ Sci Pollut Res 19(9):3676–3687. https://doi.org/10.1007/s11356-012-0939-4
12. Balsamo S, Fiorenza R, Condorelli M et al (2021) One-pot synthesis of TiO2-rGO photocatalysts for the degradation of groundwater pollutants. Materials 14(20):5938–5956. https://doi.org/10.3390/ma14205938
13. Ali MHH, Al-Afify AD, Goher ME (2018) Preparation and characterization of graphene – TiO_2 nanocomposite for enhanced photodegradation of Rhodamine-B dye. Egypt J Aquat Res 44(4):263–270. https://doi.org/10.1016/j.ejar.2018.11.009
14. Kocijan M, Ćurković L, Bdikin I et al (2022) Immobilised rGO/TiO2 nanocomposite for multi-cycle removal of methylene blue dye from an aqueous medium. Appl Sci 12(1):385–398. https://doi.org/10.3390/app12010385
15. Lin W, Xie X, Wang X et al (2018) Efficient adsorption and sustainable degradation of gaseous acetaldehyde and o-xylene using rGO-TiO_2 photocatalyst. Chem Eng J 349:708–718. https://doi.org/10.1016/j.cej.2018.05.107
16. Kocijan M, Ćurković L, Gonçalves G et al (2022) The potential of rGO@TiO2 photocatalyst for the degradation of organic pollutants in water. Sustainability 14(19):12703–12721. https://doi.org/10.3390/su141912703
17. Xu L, Yang L, Johansson EMJ et al (2018) Photocatalytic activity and mechanism of bisphenol a removal over TiO_{2-x}/rGO nanocomposite driven by visible light. Chem Eng J 350:1043–1055. https://doi.org/10.1016/j.cej.2018.06.046
18. Luna-Sanguino G, RuÃz-Delgado A, Tolosana-Moranchel A et al (2020) Solar photocatalytic degradation of pesticides over TiO_2-rGO nanocomposites at pilot plant scale. Sci Total Environ 737:140286–140390. https://doi.org/10.1016/j.scitotenv.2020.140286
19. Yuan L, Yu Q, Zhang Y et al (2014) Graphene–TiO_2 nanocomposite photocatalysts for selective organic synthesis in water under simulated solar light irradiation. RSC Adv 4(29):15264–15270. https://doi.org/10.1039/C4RA01190B
20. Li J, Xue X, Li X et al (2016) Synthesis of biscoumarin and dihydropyran derivatives as two novel classes of potential anti-bacterial derivatives. Arch Pharm Res 39(10):1349–1355. https://doi.org/10.1007/s12272-015-0614-7
21. Jung J, Park O (2009) Synthetic approaches and biological activities of 4-hydroxycoumarin derivatives. Molecules 14(11):4790–4803. https://doi.org/10.3390/molecules14114790
22. Hamdi N, Puerta MC, Valerga P (2008) Synthesis, structure, antimicrobial and antioxidant investigations of dicoumarol and related compounds. Eur J Med Chem 43(11):2541–2548. https://doi.org/10.1016/j.ejmech.2008.03.038
23. Choudhary MI, Fatima N, Khan KM et al (2006) New biscoumarin derivatives-cytotoxicity and enzyme inhibitory activities. Med Chem 14(23):8066–8072. https://doi.org/10.1016/j.bmc.2006.07.037
24. Reddy DS, Kongot M, Singh V et al (2021) Biscoumarin–pyrimidine conjugates as potent anticancer agents and binding mechanism of hit candidate with human serum albumin. Arch Pharm (Weinheim) 354(1):2000181–2000195. https://doi.org/10.1002/ardp.202000181
25. Manolov I, Maichle-Moessmer C, Nicolova I et al (2006) Synthesis and anticoagulant activities of substituted 2,4-diketochromans, biscoumarins, and chromanocoumarins. Arch Pharm (Weinheim) 339(6):319–326. https://doi.org/10.1002/ardp.200500149
26. Chaudhary G, Goyal S, Poonia P (2010) *Lawsonia inermis* linnaeus: a phytopharmacological review. Int J Pharm Sci Drug Res 2(2):91–98
27. De Oliveira AS, Brighente I, Lund R et al (2017) Antioxidant and antifungal activity of naphthoquinones dimeric derived from lawsone. J Biosci Med 5(2):39–48. https://doi.org/10.4236/jbm.2017.52004
28. De Araújo M, De Souza P, De Queiroz A et al (2014) Synthesis, leishmanicidal activity and theoretical evaluations of a series of substituted bis-2-hydroxy-1,4-naphthoquinones. Molecules 19(9):15180–15195. https://doi.org/10.3390/molecules190915180
29. Novais J, Rosandiski A, De Carvalho C et al (2020) Efficient synthesis and antibacterial profile of bis(2-hydroxynaphthalene-1,4-dione). Curr Top Med Chem 20(2):121–131. https://doi.org/10.2174/1568026619666191210160342
30. Sharma G, Kumar SV, Wahab HA (2018) Molecular docking, synthesis, and biological evaluation of naphthoquinone as potential novel scaffold for H5N1 neuraminidase inhibition. J Biomol Struct Dyn 36(1):233–242. https://doi.org/10.1080/07391102.2016.1274271
31. Mazumder A, Wang S, Neamati N et al (1996) Antiretroviral agents as inhibitors of both human immunodeficiency virus type 1 integrase and protease. J Med Chem 39(13):2472–2481. https://doi.org/10.1021/jm960074e
32. Khurana JM, Kumar S (2009) Tetrabutylammonium bromide (TBAB): a neutral and efficient catalyst for the synthesis of biscoumarin and 3,4-dihydropyrano[c]chromene derivatives in water and solvent-free conditions. Tetrahedron Lett 50(28):4125–4127. https://doi.org/10.1016/j.tetlet.2009.04.125
33. Mehrabi H, Abusaidi H (2010) Synthesis of biscoumarin and 3,4-dihydropyrano[c]chromene derivatives catalysed by sodium dodecyl sulfate (SDS) in neat water. J Iran Chem Soc 7(4):890–894. https://doi.org/10.1007/BF03246084
34. Tabatabaeian K, Heidari H, Khorshidi A et al (2012) Synthesis of biscoumarin derivatives by the reaction of aldehydes and 4-hydroxycoumarin using ruthenium (III) chloride hydrate as a versatile homogeneous catalyst. J Serbian Chem Soc 77(4):407–413. https://doi.org/10.2298/JSC110427189T
35. Heravi MM, Sadjadi S, Haj NM et al (2009) Role of various heteropolyacids in the reaction of 4-hydroxycoumarin, aldehydes and ethylcyanoacetate. Catal Commun 10(13):1643–1646. https://doi.org/10.1016/j.catcom.2009.04.031
36. Khurana JM, Kumar S (2010) Ionic liquid: an efficient and recyclable medium for the synthesis of octahydroquinazolinone and biscoumarin derivatives. Monatsh Chem Chem Mon 141(5):561–564. https://doi.org/10.1007/s00706-010-0306-4
37. Thuy Giang LN, Tuyet Anh DT, Thi Phuong H et al (2021) DMAP-catalyzed efficient and convenient approach for the synthesis of 3,3′-(arylmethylene)bis(2-hydroxynaphthalene-1,4-dione)

derivatives. Nat Prod Commun 16(9):1934578X2110458. https://doi.org/10.1177/1934578X211045808

38. Kaur G, Singh D, Singh A et al (2021) Camphor sulfonic acid catalyzed facile and general method for the synthesis of 3,3'-(arylmethylene)bis(4-hydroxy-2H-chromen-2-ones), 3,3'-(arylmethylene)bis(2-hydroxynaphthalene-1,4-diones) and 3,3'-(2-oxoindoline-3,3-diyl)bis(2-hydroxynaphthalene-1,4-dione) derivatives at room temperature. Synth Commun 51(7):1045–1057. https://doi.org/10.1080/00397911.2020.1856877
39. Mitra B, Ghosh P (2021) Humic acid: a biodegradable organocatalyst for solvent-free synthesis of bis(indolyl)methanes, bis(pyrazolyl)methanes, bis-coumarins and bis-lawsones. ChemistrySelect 6(1):68–81. https://doi.org/10.1002/slct.202004245
40. Wang H, Wang Z, Wang C et al (2014) Lipase catalyzed synthesis of 3,3′-(arylmethylene)bis(2-hydroxynaphthalene-1,4-dione). RSC Adv 4(67):35686–35689. https://doi.org/10.1039/C4RA06516F
41. Tisseh ZN, Bazgir A (2009) An efficient, clean synthesis of 3,3′-(arylmethylene)bis(2-hydroxynaphthalene-1,4-dione) derivatives. Dyes Pigm 83(2):258–261. https://doi.org/10.1016/j.dyepig.2008.09.003
42. De Oliveira AS, Llanes LC, Nunes RJ et al (2014) Use of ultrasound and microwave irradiation for clean and efficient synthesis of 3,3'-(arylmethylene)bis(2-hydroxynaphthalene-1,4-dione) derivatives. Green Sustain Chem 4(4):177–184. https://doi.org/10.4236/gsc.2014.44023
43. Brahmachari G (2015) Sulfamic acid-catalyzed one-pot room temperature synthesis of biologically relevant bis-lawsone derivatives. ACS Sustain Chem Eng 3(9):2058–2066. https://doi.org/10.1021/acssuschemeng.5b00325
44. Asghari-Haji F, Rad-Moghadam K, Mahmoodi NO (2016) An efficient approach to bis-benzoquinonylmethanes on water under catalysis of the bio-derived O-carboxymethyl chitosan. RSC Adv 6(33):27388–27394. https://doi.org/10.1039/C5RA26580K
45. Shaikh S, Rasal S, Ramana MMV (2021) Ultrasound assisted synthesis of pyrano[3,2-b]pyran and 7-tosyl-4,7-dihydropyrano[2,3-e]indole scaffolds using barium titanate nanoparticles. React Kinet Mech Catal 133(1):405–424. https://doi.org/10.1007/s11144-021-01972-3
46. Shaikh S, Yellapurkar I, Ramana MMV (2021) Ultrasound assisted one-pot synthesis of novel antipyrine based α-aminophosphonates using TiO_2/carbon nanotubes nanocomposite as a heterogeneous catalyst. React Kinet Mech Catal 134(2):917–936. https://doi.org/10.1007/s11144-021-02110-9
47. Hummers WS, Offeman RE (1958) Preparation of graphitic oxide. J Am Chem Soc 80(6):1339–1339. https://doi.org/10.1021/ja01539a017
48. Li D, Müller MB, Gilje S et al (2008) Processable aqueous dispersions of graphene nanosheets. Nat Nanotechnol 3(2):101–105. https://doi.org/10.1038/nnano.2007.451
49. Men X, Wu Y, Chen H et al (2017) Facile fabrication of TiO_2/Graphene composite foams with enhanced photocatalytic properties. J Alloys Compd 703:251–257. https://doi.org/10.1016/j.jallcom.2017.01.353
50. Li Y, Zhang S, Li N et al (2020) A highly sensitive and selective molecularly imprinted electrochemical sensor modified with TiO_2-reduced graphene oxide nanocomposite for determination of podophyllotoxin in real samples. J Electroanal Chem 873:114439–114437. https://doi.org/10.1016/j.jelechem.2020.114439
51. Nipane SV, Lee S, Gokavi GS et al (2018) In situ one pot synthesis of nanoscale TiO_2-anchored reduced graphene oxide (RGO) for improved photodegradation of 5-fluorouracil drug. J Mater Sci Mater Electron 29(19):16553–16564. https://doi.org/10.1007/s10854-018-9749-x
52. John D, Rajalakshmi AS, Lopez RM et al (2020) TiO_2-reduced graphene oxide nanocomposites for the trace removal of diclofenac. SN Appl Sci 2(5):840–855. https://doi.org/10.1007/s42452-020-2662-y
53. Sher Shah MSA, Park AR, Zhang K et al (2012) Green synthesis of biphasic TiO_2–reduced graphene oxide nanocomposites with highly enhanced photocatalytic activity. ACS Appl Mater Interfaces 4(8):3893–3901. https://doi.org/10.1021/am301287m
54. Adamu H, Dubey P, Anderson JA (2016) Probing the role of thermally reduced graphene oxide in enhancing performance of TiO_2 in photocatalytic phenol removal from aqueous environments. Chem Eng J 284:380–388. https://doi.org/10.1016/j.cej.2015.08.147
55. Deshmukh SP, Kale DP, Kar S et al (2020) Ultrasound assisted preparation of rGO/TiO_2 nanocomposite for effective photocatalytic degradation of methylene blue under sunlight. Nano-Struct Nano-Objects 21:100407–100411. https://doi.org/10.1016/j.nanoso.2019.100407
56. Tan L, Ong W, Chai S et al (2013) Reduced graphene oxide-TiO_2 nanocomposite as a promising visible-light-active photocatalyst for the conversion of carbon dioxide. Nanoscale Res Lett 8(1):465–473. https://doi.org/10.1186/1556-276X-8-465
57. Benjwal P, Kumar M, Chamoli P et al (2015) Enhanced photocatalytic degradation of methylene blue and adsorption of arsenic (III) by reduced graphene oxide (rGO)–metal oxide (TiO_2/Fe_3O_4) based nanocomposites. RSC Adv 5(89):73249–73260. https://doi.org/10.1039/C5RA13689J
58. Kocijan M, Ćurković L, Radošević T et al (2020) Photocatalytic degradation of organic pollutant using TiO2/rGO nanocomposites under simulated sunlight. Nanomater Sci Eng 2(4):162–169. https://doi.org/10.34624/nmse.v2i4.21063
59. Yu L, Wang L, Sun X et al (2018) Enhanced photocatalytic activity of rGO/TiO_2 for the decomposition of formaldehyde under visible light irradiation. J Environ Sci 73:138–146. https://doi.org/10.1016/j.jes.2018.01.022
60. Kocijan M, Ćurković L, Radošević T (2021) Enhanced photocatalytic activity of hybrid rGO@TiO2/CN Nanocomposite for organic pollutant degradation under solar light irradiation. Catalysts 11(9):1023–1038. https://doi.org/10.3390/catal11091023
61. Zeydi MM, Mahmoodi N (2016) Nano TiO_2@KSF as a high-efficient catalyst for solvent-free synthesis of biscoumarin derivatives. Int J Nano Dimens 7(2):174–180
62. Shamsaddini A, Sheikhhosseini E (2014) Synthesis of 3,3-Arylidene Bis(4-Hydroxycoumarin) catalyzed by p-Dodecylbenzenesulfonic acid (DBSA) in aqueous media and microwave irradiation. Int J Org Chem 4(2):135–141. https://doi.org/10.4236/ijoc.2014.42015
63. Shirini F, Lati MP (2017) $BiVO_4$-NPs: an efficient nanocatalyst for the synthesis of biscoumarins, bis(indolyl)methanes and 3,4-dihydropyrimidin-2(1H)-ones (thiones) derivatives. J Iran Chem Soc 14(1):75–87. https://doi.org/10.1007/s13738-016-0959-y
64. Babaei H, Montazeri N (2014) Nano TiO_2: an efficient catalyst for the synthesis of biscoumarins in aqueous medium. Orient J Chem 30(2):577–280. https://doi.org/10.13005/ojc/300223
65. Khodabakhshi S, Marahel F, Rashidi A et al (2015) A green synthesis of substituted coumarins using nano graphene oxide as recyclable catalyst. J Chin Chem Soc 62(5):389–392. https://doi.org/10.1002/jccs.201400349
66. Riaz MT, Yaqub M, Shafiq Z et al (2021) Synthesis, biological activity and docking calculations of bis-naphthoquinone

derivatives from lawsone. Bioorg Chem 114:105069–105071. https://doi.org/10.1016/j.bioorg.2021.105069

Authors and Affiliations

Sarfaraz Shaikh[1,2] · **Ishita Yellapurkar**[1] · **Sonal Bhabal**[1] · **M. M. V. Ramana**[1] · **Julekha A. Shaikh**[3]

✉ Sarfaraz Shaikh
sarfarazshaikh@rizvicollege.edu.in

[1] Department of Chemistry, University of Mumbai, Santacruz (E), 400 098 Mumbai, India

[2] Department of Chemistry, Rizvi College of Arts, Science and Commerce, Bandra (West), Mumbai 400 050, India

[3] Department of Chemistry, Maharashtra College of Arts, Science and Commerce, 246-A, J.B.B. Marg, 400 008 Mumbai, India

Journal for Re Attach Therapy and Developmental Diversities
eISSN: 2589-7799
2023 June; 6(6s): 1023-1026

Data Analytics: A Game Changer For Better Business Decisions And Results

Dr. Mohammed Abdul Raffey[1*] Dr. Sandeep B. Gaikwad[2,] Dr Siddiqui Lubna Javed Hasan[3,] Farhat Hasan[4]

[1*]Assistant Professor UGC-Malaviya Mission Teachers Training Center, Dr. Babasaheb Ambedkar Marathwada University, Chhatrapati Sambhajinagar
[2]Associate Professor and Head Shri Muktanand College Gangapur Dist. Chhatrapati Sambhajinagar
[3]Sr.Data Analyst IT Support Stop, Hyderabad
[4]Assistant professor Rizvi college of Arts science and commerce

[*]**Corresponding Author:** Dr. Mohammed Abdul Raffey,
*****Assistant Professor UGC-Malaviya Mission Teachers Training Center

Abstract

Data analytics has emerged as a transformative tool in the modern business landscape, driving more informed decision-making and delivering substantial results. This paper explores the evolution, methodologies, applications, and impact of data analytics on business decisions. By examining case studies and industry trends, we illustrate how data-driven strategies can enhance efficiency, customer satisfaction, and competitive advantage. The paper also discusses challenges and future directions in the field of data analytics.

Introduction

Background

In the era of digital transformation, businesses are inundated with vast amounts of data. This data, if harnessed effectively, can provide deep insights into various aspects of business operations. Data analytics, the process of examining raw data to draw conclusions and make informed decisions, has become a pivotal component in the business decision-making process.

Importance of Data Analytics

Data analytics enables businesses to identify trends, uncover patterns, and gain insights that were previously unattainable. This analytical capability allows for better forecasting, improved operational efficiency, and enhanced customer experiences. As a result, data analytics is not just a tool but a game changer for businesses aiming to stay competitive in a rapidly evolving market.

Evolution of Data Analytics

Early Beginnings

The roots of data analytics can be traced back to the early days of computing, where simple statistical methods were applied to business data. The advent of computers in the mid-20th century provided the computational power needed to process larger datasets, laying the foundation for modern data analytics.

The Rise of Big Data

The 21st century saw an explosion of data generation, often referred to as "big data." This era was marked by the proliferation of the internet, social media, and the Internet of Things (IoT), which contributed to the massive increase in data volume, variety, and velocity. This shift necessitated the development of more sophisticated data analytics tools and techniques.

Modern Data Analytics

Today, data analytics encompasses a wide range of methodologies, including descriptive, diagnostic, predictive, and prescriptive analytics. Advanced technologies such as machine learning, artificial intelligence (AI), and deep learning have further augmented the capabilities of data analytics, allowing for real-time analysis and more accurate predictions.

Methodologies in Data Analytics

Descriptive Analytics

Descriptive analytics involves the analysis of historical data to understand what has happened in the past. It uses data aggregation and data mining techniques to provide insights into past performance. Common tools for descriptive analytics include dashboards and reporting systems.

Diagnostic Analytics

Diagnostic analytics goes a step further by examining the reasons behind past performance. It uses techniques such as drill-down, data discovery, and correlations to identify the underlying causes of trends and patterns.

Predictive Analytics

Predictive analytics uses historical data and statistical algorithms to forecast future outcomes. Techniques such as regression analysis, time series analysis, and machine learning models are commonly employed in predictive analytics. This methodology helps businesses anticipate future trends and make proactive decisions.

Prescriptive Analytics

Prescriptive analytics recommends actions based on predictive insights. It uses optimization and simulation algorithms to suggest the best course of action for achieving desired outcomes. This methodology is particularly useful in resource allocation, scheduling, and supply chain management.

Applications of Data Analytics in Business

Marketing

Data analytics has revolutionized marketing by enabling personalized campaigns and targeted advertising. By analyzing customer data, businesses can segment their audience, predict customer behavior, and tailor their marketing strategies to maximize ROI.

Finance

In the finance sector, data analytics is used for risk management, fraud detection, and investment decision-making. Predictive models help financial institutions identify potential risks and opportunities, improving their overall financial performance.

Operations

Operational efficiency can be significantly enhanced through data analytics. Businesses use analytics to optimize supply chain management, reduce operational costs, and improve productivity. Real-time analytics allows for quick decision-making and agile responses to market changes.

Customer Service

Data analytics plays a crucial role in enhancing customer service. By analyzing customer feedback, interaction history, and behavior patterns, businesses can improve their service quality, address customer issues proactively, and enhance overall customer satisfaction.

Impact of Data Analytics on Business Decisions

Improved Decision-Making

Data-driven decision-making leads to more accurate and informed decisions. By relying on data analytics, businesses can reduce uncertainty, minimize risks, and make strategic choices that align with their objectives.

Enhanced Competitive Advantage

Businesses that leverage data analytics gain a competitive edge by staying ahead of market trends, understanding customer needs better, and optimizing their operations. This advantage is crucial in maintaining market leadership and driving growth.

Increased Efficiency and Productivity

Data analytics streamlines business processes, identifies bottlenecks, and suggests improvements. This leads to increased operational efficiency, reduced costs, and higher productivity, contributing to better overall business performance.

Case Studies

Amazon

Amazon's success is largely attributed to its data-driven approach. The company uses data analytics for inventory management, personalized recommendations, and dynamic pricing. These strategies have enabled Amazon to enhance customer satisfaction, optimize operations, and maintain a competitive edge.

Netflix

Netflix leverages data analytics to understand viewer preferences and predict content success. By analyzing viewing patterns, Netflix creates personalized recommendations and invests in original content that resonates with its audience, leading to increased subscriber retention and growth.

Walmart

Walmart uses data analytics to optimize its supply chain, manage inventory, and enhance customer experiences. Real-time analytics allows Walmart to respond quickly to market demands, reduce stockouts, and improve overall operational efficiency.

Challenges in Data Analytics

Data Quality

The accuracy and reliability of data are critical for effective analytics. Poor data quality can lead to incorrect insights and flawed decision-making. Ensuring data integrity and consistency is a significant challenge for businesses.

Data Privacy and Security

With the increasing volume of data comes the responsibility to protect it. Data privacy and security concerns are paramount, especially with stringent regulations such as GDPR. Businesses must implement robust security measures to safeguard sensitive information.

Skill Gap

The demand for skilled data analysts and data scientists often exceeds supply. Bridging the skill gap is essential for businesses to fully leverage the potential of data analytics. Continuous training and development programs are necessary to build a competent workforce.

Future Directions

Integration of AI and Machine Learning

The integration of AI and machine learning with data analytics will continue to advance, providing more sophisticated and autonomous analytical capabilities. This integration will enable businesses to uncover deeper insights and make more accurate predictions.

Real-Time Analytics

Real-time analytics will become increasingly prevalent, allowing businesses to make immediate decisions based on current data. This capability is particularly valuable in dynamic industries where rapid response is crucial.

Enhanced Data Visualization

Improved data visualization tools will make it easier for businesses to interpret complex data. Interactive dashboards and advanced visualization techniques will enhance the accessibility and usability of data analytics.

Conclusion

Data analytics has undeniably transformed the business landscape, enabling more informed decision-making and delivering significant results. As businesses continue to navigate the complexities of the modern market, the role of data analytics will only grow in importance. By embracing data-driven strategies and overcoming the associated challenges, businesses can unlock new opportunities, drive growth, and achieve long-term success.

References

1. Davenport, T. H., & Harris, J. G. (2007). Competing on Analytics: The New Science of Winning. Harvard Business Review Press.
2. Provost, F., & Fawcett, T. (2013). Data Science for Business: What You Need to Know About Data Mining and Data-Analytic Thinking. O'Reilly Media.

3. Waller, M. A., & Fawcett, S. E. (2013). Data Science, Predictive Analytics, and Big Data: A Revolution That Will Transform Supply Chain Design and Management. Journal of Business Logistics, 34(2), 77-84.
4. McAfee, A., & Brynjolfsson, E. (2012). Big Data: The Management Revolution. Harvard Business Review, 90(10), 60-68.
5. Chen, H., Chiang, R. H., & Storey, V. C. (2012). Business Intelligence and Analytics: From Big Data to Big Impact. MIS Quarterly, 36(4), 1165-1188.

Photosensitivity and structural properties of vanadium-doped ZnO and ZnO nanoparticle at various calcined temperature

Article *in* Materials Today Proceedings · September 2023

DOI: 10.1016/j.matpr.2023.08.362

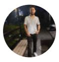

Ghulam Mustafa
University of Allahabad

Shekhar Srivastava
University of Allahabad

Kashif Aziz
University of Allahabad

Rahul Kanaoujiya
Central University of Allahabad

ARTICLE IN PRESS

Materials Today: Proceedings xxx (xxxx) xxx

Contents lists available at ScienceDirect

Materials Today: Proceedings

journal homepage: www.elsevier.com/locate/matpr

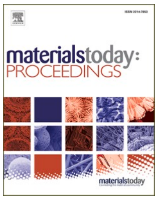

Photosensitivity and structural properties of vanadium-doped ZnO and ZnO nanoparticle at various calcined temperature

Ghulam Mustafa [a], Shekhar Srivastava [a], Mohd Kashif Aziz [a], Rahul Kanaoujiya [b],*, C. Rajkumar [c]

[a] Nanotechnology Laboratory, Department of Chemistry, University of Allahabad, Prayagraj, Uttar Pradesh, India
[b] Synthetic Inorganic and Metallo-Organic Research Laboratory, Department of Chemistry, University of Allahabad, Uttar Pradesh, India
[c] Department of Electronics & Communication, University of Allahabad, Uttar Pradesh, India

ARTICLE INFO

Keywords:
Vanadium-doped ZnO NPs
Zinc oxide
XRD
SEM
Photoluminescence
Nanoparticle and FTIR

ABSTRACT

The aim of the research to elucidate the photosensitivity of a synthesized nanomaterial, i.e. ZnO NPs and 10% vanadium-doped ZnO NPs with their characterization. The material were characterized by X-Ray diffractometer (XRD), Fourier Transform Infrared spectroscopy (FTIR), Scanning Electron Microscopy (SEM) and Photoluminescence (PL). XRD confirms the formation of ZnO and V-ZnO NPs from its peaks and confirmed the doping of a vanadium element with ZnO NPs by JCPDS with different calcination temperature (450 °C, 550 °C and 660 °C). By increasing a temperature its peak or crystallinity is also increases and confined its atom in a peak. FTIR confirms the formation of ZnO and V-doped ZnO NPs by their specific spectral peaks. SEM images shows that the ZnO NPs is spherical in shape with an average particle size of 50 nm and V-ZnO NPs is polyhedral or hexagonal with an average particle size of 74 nm confirms its morphology. The property of photoconductivity has been measured by photoluminescence via UV–vis illumination. Sample with high calcination show good result due to increase in Zn_idefect but with vanadium-doped ZnO NPs shows the higher and more interesting result than the ZnO NPs.

1. Introduction

Nanotechnology is the controlled creation, manipulation, and study of nanoscale materials with diameters smaller than 100 nm [1]. This interdisciplinary field makes it possible new developments are exciting, and materials with valued features [2]. The properties of nanoparticles are unique and can be altered by chemical, biological, or physical processes [3]. Metal oxide nanoparticles shows the biological, magnetic, electrical, antimicrobial, catalytic and optical capabilities are dependent on their size, shape, and chemical nature [4–6]. Zinc oxide (ZnO) is a semiconducting compound that belongs to the II-VI group and has a wide direct bandgap of ~ 3.35 eV at room temperature, exceptional chemical stability, and a high exciton binding energy (60 meV) [7–9]. ZnO nanoparticles are one of the most interesting materials used in many different types of devices, including electronics [10,11], photonics [12], spintronics [13], biosensors [7], drug delivery systems [14,15], photocatalysis [16,17] andbio imaging [18,19]. However, there are still some significant barriers to the creation of devices using both pure ZnO and transition metals doped ZnO [18].

Extensive studies on transition metal (TM)-doped ZnO oxide-based semiconductors have been researches in recent years to investigate that the changes in dopant ions cause in the physical properties of a parent material [20,21]. Particularly luminescent inorganic nanoparticles have aroused interest because of their large potential applications and for fundamental scientific research in a range of fields in doped semiconductors [7,22]. Additionally, the research on the magneto-optical properties of the TM-doped ZnO system is also greatly encouraged by the exceptional optical transparency of ZnO and the potential for band gap engineering by TM doping, which could result in the development of innovative magneto-optoelectronic devices [21,23].In the literatures, it has been discovered that vanadium doping can cause the generation of defects and fill in its voids of ZnO NPs. Because of the presence of the multivalent vanadium ion, versatile magnetic ordering has been obtained by substituting vanadium in the host lattice of zinc oxide [24,25]. It should be noted that vanadium has smaller ionic radii than zinc, which can be used through band engineering to utilize nanostructures of vanadium (V)-doped zinc oxide for use in sensing systems. Additionally, their vast application potential in fields like optical devices and biological applications like displays and anticounterfeiting, luminescence-based techniques have recently gained a lot of

---

* Corresponding author.
E-mail address: rahul.k@allduniv.ac.in (R. Kanaoujiya).

https://doi.org/10.1016/j.matpr.2023.08.362
Received 27 May 2023; Received in revised form 27 August 2023; Accepted 30 August 2023

Please cite this article as: Ghulam Mustafa et al., *Materials Today: Proceedings*, https://doi.org/10.1016/j.matpr.2023.08.362

attention [17,26–28].

Many theoretical and experimental studies have been conducted in recent years to actualize the morphology, optical and magnetic potential [1,3,4,6,17,29]. It was found an increase in vanadium doping concentration, detected a blue shift in the band gap of V-doped ZnO [30], the ferroelectric response in two-dimensional V-doped ZnO [31], an increase in doping concentration saw an improvement in the transparency of the ZnO-V-based films in the visible area [32], contradicting findings as a decrease in both the band gap and transparency [33], a red shift in the band gap by increasing the doping concentration [21,24].

In this article, we were synthesized a ZnO NPs and 10 % Vanadium-doped ZnONPs. The sample were prepared via a sol–gel method and post-annealed at different temperatures of 450 °C, 550 °Cand 650 °C under an open atmospheric system. The sample were characterized by XRD, FTIR and SEM. X-ray diffraction was employed to demonstrate the effect of calcination temperature(450 °C, 550 °C and 650 °C) on the structural and crystallite properties of a vanadium doped ZnO NPs and done a photoluminescence of a prepared sample to study the effect of 10 % vanadium doping in a versatile ZnO NPs.

2. Material & method

The bottom-up technique has been used to synthesize the ZnO and Vanadium-doped ZnO NPs via sol–gel method through propylene glycol. In the preparation of ZnO NPs, we used zinc nitrate hexahydrate as a precursor and Vandium-doped ZnO NPs synthesized by using a Zinc nitrate hexahydrate and vanadium acetylacetonate solution precursors were mixed in an appropriate ratios to formation of a resultant solution. Under steady stirring, propylene glycol was added to the aforementioned solution in a 1:1 mol ratio with regard to the metal nitrates. The solution was then heated to 100 °C while being constantly stirred, allowing all of the liquid to evaporate. The resultant sample of powder were then calcined in a different temperatures (450 °C, 550 °C and 660 °C) for 2 h to obtained a well crystalline and pure sample of nanoparticles for further analysis.

A powder X-ray diffraction (PXRD) technique by using a high-resolution PAN analytical X'pert diffractometer with a Xe detector using Cu K radiation (=1.5418), a step size of 0.02° throughout the 2 range of 20-90° at room temperature, and a scan rate of 4.5 s per step. Ascanning electron microscope (SEM) JEOL 6610LV was used to evaluate the morphology of a sample. The Perkin Elmer 2000 Fourier-transform infrared spectrometer was used to record the FT-IR spectra using KBr pellet. All samples photoluminescence (PL) spectra were captured using a PerkinElmer spectrometer at room temperature (Model: LS 45).

3. Results and discussion

Fig. 1A, shows XRD patterns of ZnO NPs in different temperatures i.e. ZnO450, ZnO 550 and ZnO650 NPs samples. The XRD patterns of all samples have hexagonal wurtzite structure confirmed through JCPDS card no: 01–089-1397for ZnO400, ZnO550 with a miller indices of (1 0 0), (0 0 2), (1 0 1), (1 0 2), (1 1 0), (1 0 3), (2 0 0), (1 1 2), (2 0 1), (0 0 4) and (2 0 2). There are not such any additional peaks in a prepared sample, confirming that the final products are pure ZnO NPs. The intensity of XRD peaks gets increased as annealed temperature was raisedas compared to corresponding samples, which may be due to improved crystallinity after annealing wherein elevated temperature of annealing assists movement of atoms to their exact lattice locations [25].

XRD analysis of 10% concentration of vanadium doped ZnO at different calcination temperature (V-ZnO450, V-ZnO550 and V-ZnO650) are shown in Fig. 1B. It shows the presence of additional phase of ZnV_2O_4 (JCPDS No. 01–075-0318) spinal type structure in addition with VO_2 peak in compare to bare ZnO [21].The impact of temperature on the dissolution of vanadium in ZnO matrix have been performed at low temperature lower(450 °C) and another temperature higher(650 °C) for 10% dopedZnV_2O_4 concentration appears to be roughly independent of annealing temperature,irrespective of the sample thermal history, the intensity ratio between the primary zincite peak and the spinel phase remains constant.The average crystallite sizes of each sample are calculated using Debye-Scherer equation[34]:

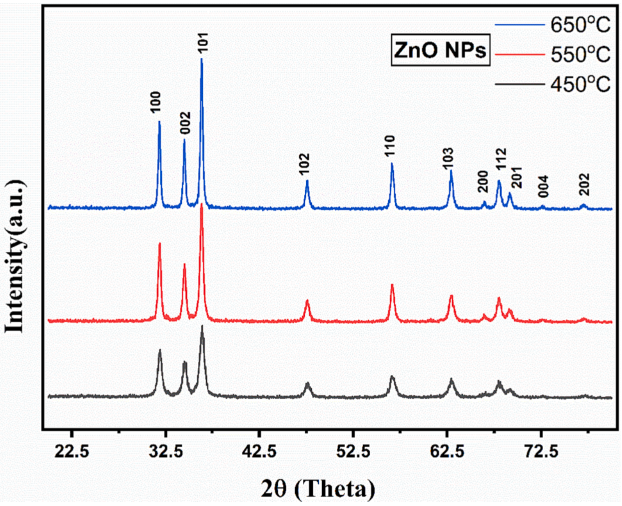

Fig. 1A. XRD graph of ZnO NPs in different temperature (450 °C, 550 °C and 660 °C).

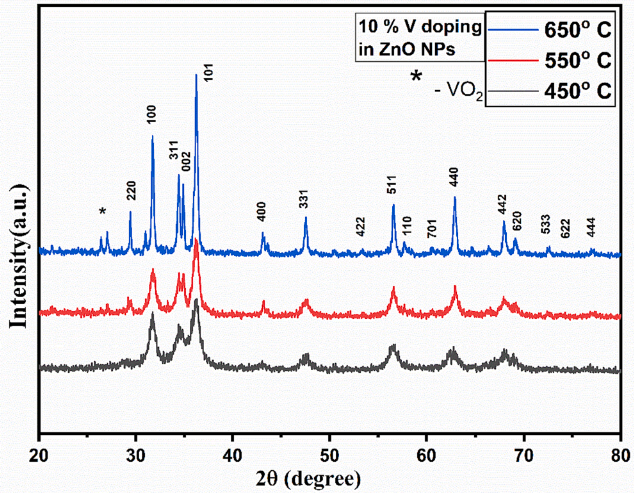

Fig. 1B. XRD graph of vanadium-doped ZnO NPs at different temperatures (450 °C, 550 °C and 650 °C).

$$D = \frac{k\lambda}{\beta cos\theta}$$

where D indicates crystallite size, K indicates Scherer constant (the shape factor of average crystallite, it is assumed here that K = 0.9), λ indicates wavelength of the X-ray using *Cu-Kα*radiation (1.5406 A), θ indicates Braggs diffraction angle in degree and β indicates Full-Width Half-Maximum (FWHM) in radian of the respective peak [34]. The average crystallite size calculated by the above equation are as follows in Table 1.

In Fig. 2, the FTIR spectra of prepared sample of ZnO and 10 % V-ZnO NPs demonstrates the confirmation peak at 730 cm^{-1}, $927^{-1}$and 1158^{-1} of V-O stretching along with the peaksof Zn-O stretching at 650 cm^{-1} and 1052 cm^{-1}. $NO_2$and N–H stretching peaks at 1521 cm^{-1} and 3500 – 3900 cm^{-1} is due to zinc nitrate hexahydrate precursor. C = C

Table 1
The average crystallite size of synthesized ZnO and V-doped ZnO at different calcination temperature.

Samples (At different temperatures)	Average Crystallite Size
Zno (450 °C)	**12 nm**
V-ZnO (450 °C)	**18 nm**
ZnO (550 °C)	**15 nm**
V-ZnO (550 °C)	**28 nm**
ZnO (650 °C)	**19 nm**
V-ZnO (650 °C)	**25 nm**

stretching peak at 1688 cm^{-1}, C–H stretching at 2920 cm^{-1} and its bending at 914 cm^{-1}and 1370 cm^{-1}, O–H stretching peak at 3500—–3900 cm^{-1} and its bending and deformation at 1321 cm^{-1} and 1370 cm^{-1}. CO_2 stretching peak at 2350 cm^{-1} due to external environment and propylene glycol as precursor.

The SEM (Scanning Electron Microscopy) micrograph can reveal the anatomy and size of ZnO NPs along with vanadium doped ZnO NPs in this study. In Fig. 3-A, the SEM images of ZnO NPs shows the spherical like crystal appearance which resembling as a bunch of black balls and an average grain size is 50 nm. In Fig. 3-B, the SEM images of 10% V doped ZnO NPs shows the polyhedral sphere or hexagonal shape which improves the adsorption activity with enhancement in their property and an average grain size of 74 nm.

Fig. 4 shows the photoluminescence spectra of ZnO450, ZnO550, ZnO650, V-ZnO450, V-ZnO550 and V-ZnO650. It shows the emission around 392–394 nm, 418–421 nm, 480–485 nm and 525–527 nm in Fig. 5. The UV emission around 392–394 nm is due to near-band edge

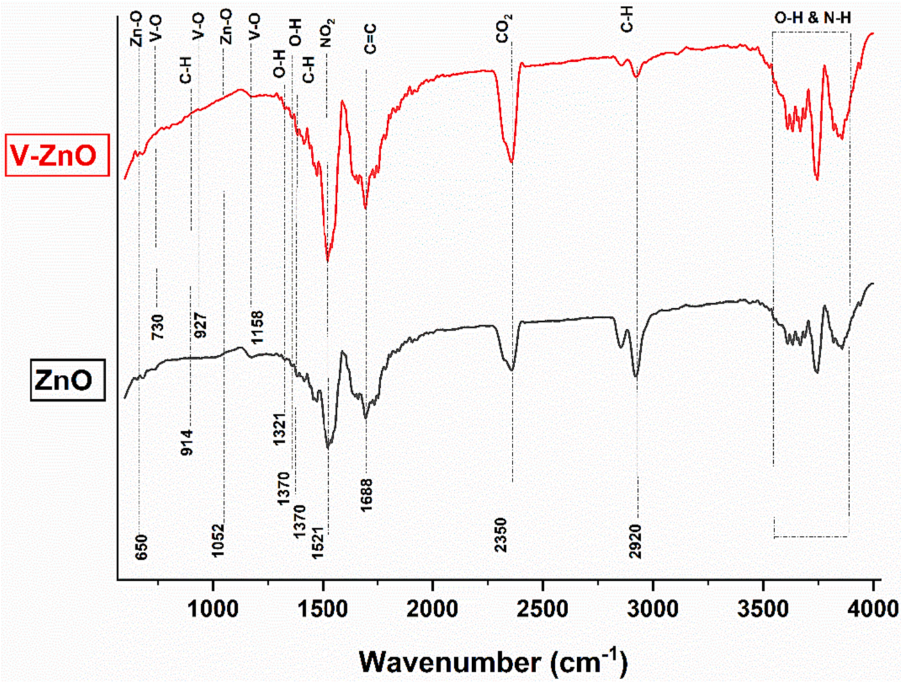

Fig. 2. FTIR spectra of ZnO and Vanadium-doped ZnO NPs.

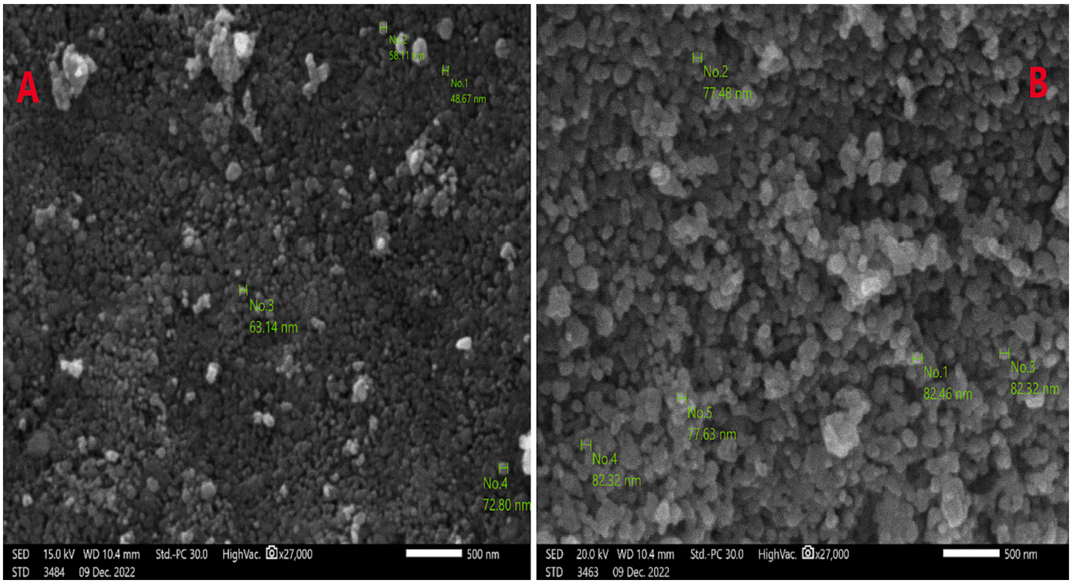

Fig. 3. A: SEM image of ZnO NPs and 3-B SEM image of 10% V-ZnO NPs with particle size.

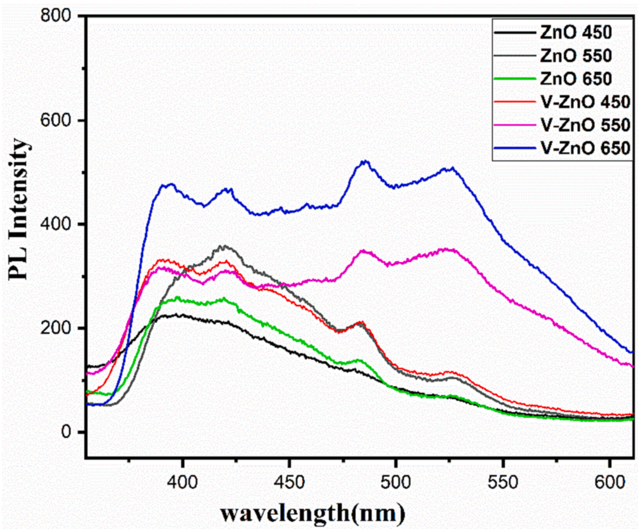

Fig. 4. Photoluminescence spectra of ZnO and V-ZnO NPs at different calcination temperature.

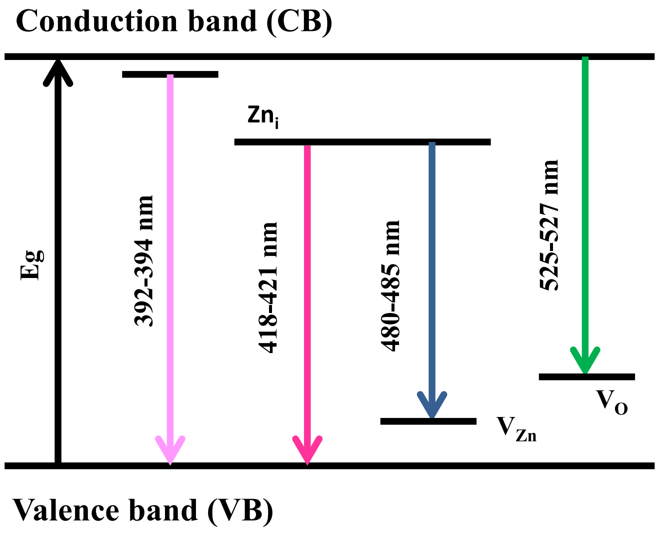

Fig. 5. Representation of Photoluminiscence spectra.

emission which is ascribed to free excitonic emission because of an exciton–exciton collision.The violet emission around 418–421 nm is due to zinc interstitials (Zn_i) defects of ZnO, which corresponds to transition of Zn_i to valence band (VB). The blue emission around 480–485 nm is due to zinc vacancy (V_{Zn}) defects which corresponds to transition of Zn_i to VB. The green emission around 525–527 nm is due to oxygen vacancy defects (V_O) which corresponds to transition of conduction band (CB) to V_o. The emission in vanadium doped ZnO is more as compared to bare ZnO, which may be due to doping of vanadium.The vanadium doped ZnO which is annealed at 650 °C have strong emission due to more defects as compared all other samples due to high temperature of annealing [9,25,35].

4. Conclusion

In this synthesis, we report on the synthesis of ZnO and V-doped ZnO NPs in different calcination temperature (heat treatment) by using sol–gel route. The effect of calcination temperature (450–650 °C) and its effect on the morphology, structural, and optical properties of as-synthesized nanomaterials was evaluated. It was shown that the morphology was greatly affected by the calcination temperature and confirmed through SEM analysis revealed highly porous with a spherical and polyhedral type hexagonal structure. XRD analysis confirmed the formation of pure phase of ZnO and vanadium-doped ZnO NPs at 450 °C, 550 °C and 650 °C with an average crystallite size in Table 1. FTIR analysis showed complete degradation via the calcination step and confirmed its presence via specific peaks. All the sample are photosensitive and results shows that increasing the calcination temperature of ZnO and V-ZnO NPs increseases their photoluminescence property due their increase in Zn_i concentration. The highest temperature of 650 °C exhibit the high level of photosensitivity as compared to other lower calcination temperature. Vanadium-doped ZnO NPs shows the relatively higher photosenstivity than the ZnO NPs. All the results of the prepared sample, we concluded that10% doped Vanadium-ZnO NPs are good for a researcher and the most promising for photo-detection in the scientific field of optoelectronic applications.

CRediT authorship contribution statement

Ghulam Mustafa: Writing – review & editing, Writing – original draft, Supervision, Methodology, Investigation. **Shekhar Srivastava:** Writing – review & editing, Supervision, Methodology, Investigation. **Mohd Kashif Aziz:** Formal analysis, Software. **Rahul Kanaoujiya:** Writing – review & editing, Supervision, Methodology, Investigation. **C. Rajkumar:** Writing – review & editing, Writing – original draft, Resources.

Declaration of Competing Interest

The authors declare that they have no known competing financial interests or personal relationships that could have appeared to influence the work reported in this paper.

Data availability

Data will be made available on request.

Acknowledgements

We gratefully thankful to the Head of the Chemistry Department of University of Allahabad in Prayagraj for providing the essential laboratory equipment. The Indian government provided financial support in the form of CSIR-SRF fellowships, for which the authors are immensely grateful to the University Grant Commission-New Delhi.

References

[1] A.G. Al-Sehemi, A.S. Al-Shihri, A. Kalam, G. Dud, T. Ahmad, M.K. Aziz, S. Chauhan, Z. Azim, G.K. Bharati, S. Srivastava, Microwave synthesis, optical properties and surface area studies of NiO nanoparticles, J. Mater. Sci. Mater. Electron. 6 (2022) 555–597, https://doi.org/10.1007/s10854-018-9411-7.

[2] S. Bayda, M. Adeel, T. Tuccinardi, M. Cordani, F. Rizzolio, The history of nanoscience and nanotechnology: From chemical-physical applications to nanomedicine, Molecules 25 (2020) 1–15, https://doi.org/10.3390/molecules25010112.

[3] A.S.K. Aziz Mohd Kashif, Kalam Abul, Mustafa Ghulam, Srivastava Shekhar, Lead oxide nanodots synthesized by solvothermal and microwave assisted method and its comparative characterization, Asian J. Chem. 34 (2022) 3293–3298. https://doi.org/https://doi.org/10.14233/ajchem.2022.24035.

[4] R. Kanaoujiya, S. K. Saroj, V. D. Rajput, Alimuddin, S. Srivastava, T. Minkina, ... & A. Kumar, Emerging application of nanotechnology for mankind, Emergent Materials. 1-14 (2023). https://doi.org/10.1007/s42247-023-00461-8.

[5] M.A. Ansari, A. Kalam, A.G. Al-Sehemi, M.N. Alomary, S. Alyahya, M.K. Aziz, S. Srivastava, S. Alghamdi, S. Akhtar, H.D. Almalki, S.F. Adil, M. Khan, M. R. Hatshan, Counteraction of biofilm formation and antimicrobial potential of terminalia catappa functionalized silver nanoparticles against candida albicans and multidrug-resistant gram-negative and gram-positive bacteria, Antibiotics 10 (2021), https://doi.org/10.3390/antibiotics10060725.

[6] M.K. Aziz, S. Chauhan, Z. Azim, G.K. Bharati, S. Srivastava, The biosynthesis of nickel oxide nanoparticles using watermelon rind extract and their biophysical effects on the germination of Vigna radiata seeds at various concentrations, (2022).

[7] L. Liu, S. Li, J. Zhuang, L. Wang, J. Zhang, H. Li, Z. Liu, Y. Han, X. Jiang, P. Zhang, Improved selective acetone sensing properties of Co-doped ZnO nanofibers by electrospinning, Sensors Actuators, B Chem. 155 (2011) 782–788, https://doi.org/10.1016/j.snb.2011.01.047.

[8] H. Ji, C. Cai, S. Zhou, W. Liu, C. Liu, F. Yun, Study of microstructural, morphological and optical properties of sprayed vanadium doped ZnO nanoparticles, J. Mater. Sci. Mater. Electron. 45 (2022) 555–597, https://doi.org/10.1016/j.aca.2012.05.048.

[9] R. C, R.K. Srivastava, Time dependent rise and decay of photocurrent in zinc oxide nanoparticles in ambient and vacuum medium, Mater. Res. Express. 5 (2018) 055002. https://doi.org/10.1088/2053-1591/aabeca.

[10] G.C. Kim, J.S.; Park, W.I.; Lee, C.H.; Yi, ZnO nanorod biosensor for highly sensitive detection of specific protein binding, J. Korean Phys. Soc. 49 (2006) 1635.

[11] F. Acosta-Humánez, R. Cogollo Pitalúa, O. Almanza, Electron paramagnetic resonance in Zn1-xCoxO, J. Magn. Magn. Mater. 329 (2013) 39–42, https://doi.org/10.1016/j.jmmm.2012.10.026.

[12] S.K. Arya, S. Saha, J.E. Ramirez-Vick, V. Gupta, S. Bhansali, S.P. Singh, Recent advances in ZnO nanostructures and thin films for biosensor applications: Review, Anal. Chim. Acta. 737 (2012) 1–21, https://doi.org/10.1016/j.aca.2012.05.048.

[13] A. Wei, X.W. Sun, J.X. Wang, Y. Lei, X.P. Cai, C.M. Li, Z.L. Dong, W. Huang, Enzymatic glucose biosensor based on ZnO nanorod array grown by hydrothermal decomposition, Appl. Phys. Lett. 89 (2006) 3–6, https://doi.org/10.1063/1.2356307.

[14] Q. Yuan, S. Hein, R.D.K. Misra, New generation of chitosan-encapsulated ZnO quantum dots loaded with drug: Synthesis, characterization and in vitro drug delivery response, Acta Biomater. 6 (2010) 2732–2739, https://doi.org/10.1016/j.actbio.2010.01.025.

[15] J. Xiao, M. Wu, G. Kai, F. Wang, H. Cao, X. Yu, ZnO-ZnS QDs interfacial heterostructure for drug and food delivery application: Enhancement of the binding affinities of flavonoid aglycones to bovine serum albumin, Nanomedicine Nanotechnology, Biologie et Médecine 7 (2011) 850–858, https://doi.org/10.1016/j.nano.2011.02.003.

[16] X. Chen, Z. Wu, D. Liu, Z. Gao, Preparation of ZnO Photocatalyst for the Efficient and Rapid Photocatalytic Degradation of Azo Dyes, Nanoscale Res. Lett. 12 (2017) 4–13, https://doi.org/10.1186/s11671-017-1904-4.

[17] G. Mustafa, M.K. Aziz, L. Sharma, G.K. Bharati, S. Chauhan, R. Kanaoujiya, S. Srivastava, Synthesis and characterization of biocone-like ZnO nanoparticles as antibacterial agent and as photocatalyst for removal of hazardous methyl orange dye, Journal of PharmaceuticsNegat. Results. 13 (2022) 5480–5490, https://doi.org/10.47750/pnr.2022.13.S07.669.

[18] H.S. Ali, A.S. Alghamdi, G. Murtaza, H.S. Arif, W. Naeem, G. Farid, S. Sharif, M.G. B. Ashiq, S.A. Shabbir, Facile microemulsion synthesis of vanadium-doped ZnO nanoparticles to analyze the compositional, optical, and electronic properties, Materials (Basel). 12 (2019), https://doi.org/10.3390/MA12050821.

[19] A. Dorfman, N. Kumar, J.I. Hahm, Nanoscale ZnO-enhanced fluorescence detection of protein interactions, Adv. Mater. 18 (2006) 2685–2690, https://doi.org/10.1002/adma.200502616.

[20] R. Bhardwaj, J.P. Singh, K.H. Chae, N. Goyal, S. Gautam, Electronic and magnetic structure investigation of vanadium doped ZnO nanostructure, Vacuum 158 (2018) 257–262, https://doi.org/10.1016/j.vacuum.2018.09.053.

[21] J. El Ghoul, Synthesis of vanadium doped ZnO nanoparticles by sol–gel method and its characterization, J. Mater. Sci. Mater. Electron. 27 (2016) 2159–2165. https://doi.org/https://doi.org/10.1007%2Fs10854-015-4006-z.

[22] C. Liu, F. Yun, H. Morko c c, JMatEng_16 Liu FM_ZnO&GaN_review.pdf, J. Mater. Sci. Mater. Electron. B. 6 (2005) 555–597. http://www.google.com/search?client=safari&rls=en&q=ZnO-+and+GaN-Based+Ferromagnetic+Materials:+A+Review&ie=UTF-8&oe=UTF-8%5Cnpapers2://publication/uuid/7C9DAB17-F0E2-472C-A375-56CDF4DAF847.

[23] P. Shukla, J.K. Shukla, Facile sol-gel synthesis and enhanced photocatalytic activity of the V2O5-ZnO nanoflakes, J. Sci.: Adv. Mater. Devices 3 (2018) 452–455, https://doi.org/10.1016/j.jsamd.2018.09.005.

[24] S. Kinra, M.P. Ghosh, S. Mohanty, R.K. Choubey, S. Mukherjee, Correlating the microstructural and optical properties of vanadium ion-doped ZnO nanocrystals, Bull. Mater. Sci. 45 (2022), https://doi.org/10.1007/s12034-021-02650-9.

[25] C. Rajkumar, Effect of annealing temperature on response time of ZnO photoconductor fabricated using thermal evaporation technique, Physica Scripta 97 (2022), https://doi.org/10.1088/1402-4896/ac95db.

[26] G. Lawes, A.S. Risbud, A.P. Ramirez, R. Seshadri, Absence of ferromagnetism in Co and Mn substituted polycrystalline ZnO, Phys. Rev. B - Condens. Matter Mater. Phys. 71 (2005) 1–5, https://doi.org/10.1103/PhysRevB.71.045201.

[27] L. Klein, Sol-gel Technology for Thin Films, Fibres, Performs, Electronics and Special Shapes, part II, New Jersey, II, Park Ridges, New Jersey, 1988.

[28] Y.W. Heo, M.P. Ivill, K. Ip, D.P. Norton, S.J. Pearton, J.G. Kelly, R. Rairigh, A. F. Hebard, T. Steiner, Effects of high-dose Mn implantation into ZnO grown on sapphire, Appl. Phys. Lett. 84 (2004) 2292–2294, https://doi.org/10.1063/1.1690111.

[29] C. Rajkumar, R.K. Srivastava, UV–visible photoresponse properties of self-seeded and polymer mediated ZnO flower-like and biconical nanostructures, Results Phys. 15 (2019) 1–10, https://doi.org/10.1016/j.rinp.2019.102647.

[30] N. Tahir, S.T. Hussain, M. Usman, S.K. Hasanain, A. Mumtaz, Effect of vanadium doping on structural, magnetic and optical properties of ZnO nanoparticles, Appl. Surf. Sci. 255 (2009) 8506–8510, https://doi.org/10.1016/j.apsusc.2009.06.003.

[31] J.H. Lee, K.Y. Lee, M.K. Gupta, T.Y. Kim, D.Y. Lee, J. Oh, C. Ryu, W.J. Yoo, C. Y. Kang, S.J. Yoon, J.B. Yoo, S.W. Kim, Highly stretchable piezoelectric-pyroelectric hybrid nanogenerator, Adv. Mater. 26 (2014) 765–769, https://doi.org/10.1002/adma.201303570.

[32] H. Ftouhi, Z. El Jouad, M. Jbilou, M. Diani, M. Addou, Study of microstructural, morphological and optical properties of sprayed vanadium doped ZnO nanoparticles, EPJ Appl. Phys. 87 (2019), https://doi.org/10.1051/epjap/2019190111.

[33] A. Watanabe, H. Chiba, T. Kawashima, K. Washio, Study on Solid-Phase Crystallization of Amorphized Vanadium-Doped ZnO Thin Films, J. Electron. Mater. 45 (2016) 2008–2012, https://doi.org/10.1007/s11664-016-4338-3.

[34] U. Holzwarth, N. Gibson, The Scherrer equation versus the 'Debye-Scherrer equation’, Nat. Publ. Gr. 6 (2011) 534. http://www.nature.com/doifinder/10.1038/nnano.2011.145%5Cnpapers2://publication/doi/10.1038/nnano.2011.145.

[35] C. Vivek, B. Balraj, S. Thangavel, Structural, optical and electrical behavior of ZnO@Ag core–shell nanocomposite synthesized via novel plasmon-green mediated approach, J. Mater. Sci. Mater. Electron. 30 (2019) 11220–11230, https://doi.org/10.1007/s10854-019-01467-x.